Important Notice

UNIVERSITY OF CALGARY

Linear AVO Inversion of Multi-component Surface Seismic and VSP Data

by

Faranak Mahmoudian

A THESIS

SUBMITTED TO THE FACULTY OF GRADUATE STUDIES

IN PARTIAL FULFILMENT OF THE REQUIREMENTS FOR THE

DEGREE OF MASTER OF SCEINCE

DEPARTMENT OF GEOLOGY AND GEOPHYSICS

CALGARY, ALBERTA

OCTOBER 2006

UNIVERSITY OF CALGARY

FACULTY OF GRADUATE STUDIES

The undersigned certify that they have read, and recommend to the Faculty of Graduate Studies for acceptance, a thesis entitled "The Linear AVO Inversion of Multi-component Surface Seismic and VSP Data" submitted by Faranak Mahmoudian in partial fulfilment of the requirements of the degree of Master of Science .

Supervisor, Dr. Gary F. Margrave,
Dept. of Geology and Geophysics

Dr. Don Lawton,
Dept. of Geology and Geophysics

Dr. Larry Lines
Dept. of Geology and Geophysics

External Examiner Dr. Len Bos
Department of Mathematics and Statistics

October 31 2006

ABSTRACT

In AVO (amplitude variation with offset) inversion the amplitudes of compressional and converted shear surface seismic data are inverted both separately and jointly to provide three parameters — the physical properties of compressional impedance, shear impedance, and density. Physical property information obtained from seismic data can be useful in imaging subsurface structure, either by directly detecting changes in the subsurface, or as an aid in the interpretation of seismic reflection data. The approximated Zoeppritz equation is least-squares fitted to the amplitude of all traces of a common-mid point gather (PP data) and a common-converted point gather (PS data) at each depth sample to obtain the band-limited reflectivity of the three parameter traces. Then, the reflectivity traces are integrated to obtain the three parameter traces with the missing low-frequency components provided from well log information. In addition, the AVO inversion of reflection surface seismic data is modified to work with VSP data as well. In this case, deconvolved upgoing wavefield extracted from VSP data is the input data to the AVO inversion.

The three parameters, especially the density, cannot accurately be resolved from AVO data due to the ill-posed nature of the inverse problem. The damped SVD (singular value decomposition) method has been utilized to stabilize the AVO inversion. The examination of the resolution matrix, after adding a damping factor, demonstrates that the shear velocity contributes more than the compressional velocity to improving the density estimate for the study area data namely, VSP data from a Red Deer coal bed methane site.

In the joint inversion, the converted shear wave data dominates in estimating the

shear impedance and density and appears promising in providing shear impedance and density estimates from the PS inversion alone. In addition, in the joint inversion the compressional data dominates in estimating the compressional impedance and provides a good estimate for the compressional impedance in the PP inversion alone.

ACKNOWLEDGEMENTS

Montana, Louis Chabot, Mary Xiao, Nancy Cao, Roxana Varga, and Catherine Brown for their support and laughter;

DEDICATION

To Vafa, Romina, Ryan, my mother,

and to the memory of my father.

TABLE OF CONTENTS

LIST OF TABLES

LIST OF FIGURES

GLOSSARY

Aki & Richards   A linear approximation to Zoeppritz equations (Sheriff, 1990)
equations

AVO   Amplitude variation versus offset

CCP gather   The set of traces which have a common converted point.

CMP gather   The set of traces which have a common midpoint (Sheriff, 1990)

Condition number   The value given when the largest singular value is divided by the

                     smallest singular value. Too large a condition number means that

                     the matrix is ill-posed, and therefore unstable (Sheriff, 1990)

Converted wave   Seismic energy which has traveled partly as a P-wave and partly as

                     an S-wave, being converted from one to the other upon reflection or

                     reflection at oblique incidence on an interface (Sheriff, 1990)

Correlation   A measure of how much two traces look alike or to extendt to which

                     one can be considered a linear function of the other

Critical angle   Angle of incident for which the reflected ray grazes the surface of

                     contact between two media (Sheriff, 1990)

Eigenvalue   A scalar λ is called an **eigenvalue** of an $n \times n$ matrix A if there is a

                     nontrivial solution **x** of $Ax = \lambda x$ (Lay, 1990)

Eigenvector   An **eigenvector** of an $n \times n$ matrix A is a nonzero vector **x** such that

$Ax = \lambda x$ for some scalar $\boldsymbol{\lambda}$ (Lay, 1990)

First break   The first recorded signal attributable to seismic-wave travel from a

known source (Sheriff, 1990)

Fourier transform   Formulas which convert a time function into its frequency-domain

representation and vice versa (Sheriff, 1990)

Gardner's rule   The empirical relationship that density is proportional to the 1/4

power of P-wave velocity (Sheriff, 1990)

Ill-posed   The situation where a small change in the data result in a large

change in the solution (Sheriff, 1990)

Impedance   Acoustic impedance, the product of density and velocity

Joint inversion   Jointly inverting the reflection PP and PS data for rock properties

K.B.   Kelly bushing. The journal box insert in the rotary table of drilling

rig through which the kelly passes. Its upper surface is commonly

the reference datum for well logs and other measurements in a well

bore (Sheriff, 1990)

Least-squares fit   An analytical function which approximates a set of data such that

the sum of the squares of the "distance" from the observed points to

the curves is a minimum (Sheriff, 1990)

NMO	Normal moveout, the variation of reflection arrival time because of source-point-to-receiver distance (Sheriff, 1990)
Offset	The source-point-to-receiver distance (Sheriff, 1990)
Polarity	The condition of being positive or negative (Sheriff, 1990)
PP data	Compressional wave reflection data
PS data	Converted wave reflection data
P-wave	Compressional wave
RMS	Root-mean-square
Singular Matrix	A matrix that has no inverse transformation (Sheriff, 1990)
SVD	Singular value decomposition is a common and precise way of solving linear least-squares problems (Sheriff, 1990)
S-wave	Shear wave
TD	Total depth, the maximum depth reached by a well (Sheriff, 1990)
VSP	Vertical seismic profile; measurement of the response of a geophone at various depths in a borehole to surface on the surface (Sheriff, 1990)
Zoeppritz equations	Equations which express the partition of energy when a plane wave impinges on an acoustic-impedance contrast (Sheriff, 1990)

LIST OF SYMBOLS

I	P-wave impedance
J	S-wave impedance
ρ	Density
G	Matrix of coefficients resulted from a linear AVO inversion
m	Model parameters (I, J, ρ)
d	Data vector
V_P	P-wave velocity
V_S	S-wave velocity
R_{PP}	PP amplitude at different offsets
R_{PS}	PS amplitude at different offsets
R	Resolution matrix
m^{est}	Estimates model parameters from the inversion

CHAPTER 1: Introduction

1.1 Measurement of Rock Properties Using Reflection Seismology

Seismic methods utilize the propagation of seismic waves through the earth. A seismic wave is an elastic disturbance propagated from point to point through a medium. In a typical seismic experiment, the seismic waves are created with artificial sources; then, by measuring the arrival time of their primary reflections from acoustic impedance contrast, the mapping of impedance contrasts is targeted. In addition to the mapping of impedance contrasts, understanding and extracting the rock properties is a goal of reflection seismology. Rock property information obtained from seismic data can be useful in imaging subsurface structure, either by directly detecting changes in the subsurface, or as an aid in the interpretation of seismic reflection data. An aim of amplitude versus offset (AVO) analysis is to deduce rock properties of the subsurface from prestack seismic data. Information about the rock properties helps in the mapping of the interior of the earth. The mapping of the interior of the earth from observations on the surface of the earth is an inverse problem (Bleistein, 1982).

A combination of three parameters is needed to describe a perfectly elastic,

isotropic earth. For example, density ρ and the Lame parameters λ and μ, or the density ρ and the P-wave and S-wave velocities, V_P and V_S (Tarantola, 1986). For the first combination, several authors have commented that more physical insight is provided by the rigidity modulus μ (Wright, 1984; Thomson, 1990; Castagna et al., 1993). Stewart (1995) discussed the potential usefulness of the Lame parameters λ and μ to better differentiate rock properties. For the second combination, a number of authors have observed a link between V_P, V_S, and pore fluid content. The relationship of V_P and V_S values to various rocks and their saturants can be complex, but can provide useful information about reservoir rock properties when used in conjunction with well-log or other independent measurements (Tatham and McCormick, 1991). There are other parameter choices describing rock properties, such as P-wave impedance, $I = \rho V_P$, S-wave impedance, $J = \rho V_S$, and density, ρ which was the choice advocated in Jonnane et al. (1988) or Tarantola (1986). The choice of parameters is not neutral in the sense that although theoretically equivalent, if they are not adequately chosen, the numerical algorithms in the inversion can be inefficient (Tarantola, 1986). In the long (spatial) wavelengths of the earth model, adequate parameters are the P-wave and S-wave velocities, while in the short (spatial) wave length, P-wave impedance, S-wave impedance, and density are adequate. The problem of inversion of waveforms is highly nonlinear for the long wavelengths of the velocities, while it is reasonably linear for the short wavelengths of the impedances and density (Tarantola, 1986).

1.2 Previous Work

Until recently, seismic exploration has consisted mainly of the interpretation of PP data. Early techniques of lithology estimation were focussed on the zero-offset or post-stack inversion of PP data. An inversion method that uses P-wave AVO variation was developed by Smith and Gidlow (1987) who showed that the P-wave and S-wave zero-offset reflectivity traces can be computed by least-squares fitting of a linear approximation of the Zoeppritz equations[1] to the reflection amplitudes within a common-midpoint or CMP gather. For their method they assumed that the Gardner's rule between density and P-wave velocity holds true ($\rho = kV_P^{1/4}$, where k is a constant) (Gardner et al., 1974). Smith and Gidlow (1987) also showed that a computationally simpler procedure for doing the least-squares fitting can be achieved by a weighted stack of the traces in the CMP gather. They went on to show that the resulting P-wave and S-wave velocity reflectivity traces can be combined to obtain "fluid factor" traces that can indicate the presence of gas. Fatti et al., 1994, modified the Smith-Gidlow method for estimating $\dfrac{\Delta I}{I}$ and $\dfrac{\Delta J}{J}$ instead by $\dfrac{\Delta V_P}{V_P}$ and $\dfrac{\Delta V_S}{V_S}$, using an empirical relationship (as in Gidlow et al., (1992)).

Originally, the majority of the work done in AVO was focused on compressional PP reflection data (Ensley, 1984). Studies have shown converted shear PS data to be preferable to conventional PP data in certain circumstances, such as a small acoustic

---

[1] Equations which express the partition of energy when a plane wave impinges on an acoustic-impedance contrast (Sheriff, 1990)

impedance contrast (Engelmark, 2000). Stewart (1990) proposed a method that incorporated PP and PS CMP gathers in a joint PP and PS inversion. This method used the linear Aki-Richards (1980) approximations with PP and PS seismic gathers to estimate of $\dfrac{\Delta V_P}{V_P}$ and $\dfrac{\Delta V_S}{V_S}$ at a particular common-reflection point. Vestrum and Stewart (1993) used synthetic data to show that the joint PP and PS inversion was effective in predicting the relative P-and S-wave velocities. Larsen and Margrave (1999) modified the joint PP and PS inversion method to invert the real PP and PS data to extract the estimates of impedance reflectivity , $\dfrac{\Delta I}{I}$ and $\dfrac{\Delta J}{J}$. They applied the joint inversion to the Blackfoot field data and showed better estimates compared to inverting the PP data only: events appeared more coherent, and the signal-to-noise ratio appeared to have increased. Zhang and Margrave (2003) applied the joint inversion to 3C-2D seismic data from the Pikes Peak oilfield. They showed the impedance reflectivity sections to be more interpretive than conventional seismic sections.

The targeted three-parameter AVO inversion problem is ill-posed for most common geometries, and noise levels necessitate the use of constraints to help stabilize the problem (Downton, 2005). In an ill-posed problem small changes in the data will lead to large errors in the estimates. Smith and Gidlow (1987) made a constraint on density by using Gardner's rule rather than setting the density term constant. Downton (2005) constrained the non-linear three-parameter AVO inversion, using probabilistic constraints

based on local geologic information. He estimated reliable density reflectivity

incorporating long offsets while taking care of NMO stretch and offset-dependent tuning.

Jin et al., (2002) used singular value decomposition (SVD) to stabilize the linearized PS

system of equations and obtain good results for both synthetics and field data.

1.3 Problem Description

The objective of this thesis is to solve an inverse problem to estimate the physical

properties, I, J and ρ, by inverting the AVO data and given the linear Aki-Richards

approximations (Section 2.2). The linear Aki-Richards approximations of the Zoeppritz

equations are equations describing the physics of the problem. The Zoeppritz equations

express the partition of energy when a plane wave impinges on an acoustic impedance

contrast (Sheriff, 1991), and are obtained by solving boundary condition equations which

express the continuity of displacement and stress at the boundary. The Zoeppritz

equations are non-linear and complex, therefore the first-order approximations (Aki-

Richards) of them is use. In addition Aki-Richards equations were chosen because they

incorporate all possible reflected modes at a given interface. The forward problem is

indicated as follows

$$G : \text{Model space} \xrightarrow[\text{equations}]{\text{Exact Zoeppritz}} \text{Data space} , \qquad (1.1)$$

with the inverse:

$$G^{-1} : \text{Data space} \xrightarrow[\text{approximations}]{\text{Aki and Richards}} \text{Model space.} \qquad (1.2)$$

The "Model space" is a space whose elements consist of all possible vectors $\begin{bmatrix} I & J & \rho \end{bmatrix}^T$

with a meaningful physical magnitude; the data space is a space whose elements consist

of vector of AVO amplitudes $\begin{bmatrix} d_1 & d_2 & \cdots & d_N \end{bmatrix}^T$.

The above three model parameters, especially the density, cannot accurately be resolved from AVO data, due to the ill-posed nature of the inverse problem. The inversion needs to be stabilized to provide good estimates for all three parameters. This complication sets the target problem in this thesis: the estimation of physical properties.

1.4 Methodology

Most of the combined classical AVO work only solves for the two parameters *I* and *J*. This thesis proposes a method that, by combining PP and PS reflection, enables the estimate of three parameters, including density. To incorporate the PP and PS data in the joint inversion, both kinds of data have been converted from time to depth.

At a particular depth over a set of source-receiver's offset, the joint AVO inversion uses the 3-parameter linear approximations of PP and PS reflection coefficients (Aki-Richards approximations). By raytracing a smooth, representative interval velocity (from borehole or velocity analysis) and assuming no dip, the angle of incidence required in reflection coefficients is calculated. The linear approximations of PP and PS reflection coefficients for different offsets result in a linear system of equations with 3 unknowns. Then the system of equations is solved by normal least-squares or the SVD method, to obtain band-limited impedances and density reflectivity. The estimated band-limited reflectivity traces are integrated to *I*, *J* and ρ, with the low frequency components

provided from the velocity-model or well logs, using a MATLAB routine called BLIMP
(Ferguson and Margrave, 1996). A damped SVD method is used to stablize the joint
inversion solutions where needed. Also, with the assumption of Gardner's rule between
P-wave velocity and density, the 2-parameter joint inversion for I and J estimate is
examined.

The AVO inversion method is evaluated using synthetics and real 3-component 2D
field VSP data. High resolution reflection data extracted from the VSP can provide
valuable information for characterizing reservoir lithology, fracture, and fluids. The AVO
inversion for surface seismic data has been modified to work with the reflected upgoing
wavefield of zero-offset and offset VSP data. The successful application of a damped
SVD in the AVO inversion of VSP data for the three parameters of I, J and ρ is
presented.

1.5 Assumptions

Regarding the physics and geometry of the problem, this work assumes that all
models studied are vertically heterogeneous and isotropic with no dipping reflectors.
Only two seismic events are considered: P-wave reflection, PP, and its respective
conversion to an SV-wave, PS. The plane wave assumption is acceptable when the
source-to-receiver distance is much longer than the wavelength of the incident wave and
is generally acceptable for precritical reflection data at exploration depths and
frequencies (Castagna et al., 1993). The plane-wave assumption is one that can cause
inaccurate estimates of near-offset data. One solution to this problem would involve

computing plane wave decompositions of recorded wavefield (Treitel et al., 1982).

The linear Aki-Richards approximations are made under the assumptions that two solid half-spaces are welded at an elastic interface, that there are only small relative changes in elastic parameters, and that the average P- and S-wave angles of incidence and transmission across the interface do not approach a critical angle or 90˚ (Aki and Richards, 1980).

1.6 Original Contributions of This Thesis

A program has been written in MATLAB to apply the joint AVO inversion on reflection surface seismic data. The joint AVO inversion program estimates the three parameters $\Delta I/I$, $\Delta J/J$ and $\Delta \rho/\rho$, using the SVD method rather than the normal least-squares method. Then these three parameter traces are integrated and low frequencies restored, resulting in estimates of I, J and ρ. The application of the SVD method in the AVO inversion rather than normal least-squares method is to provide a precise way of analyzing a matrix[2], and to yield a stable but approximate inverse. The damped SVD method is used for stabilizing the ill-posed cases and providing reasonable estimates for all three parameters I, J and ρ.

The AVO inversion has been applied for pure compressional wave (PP data), as well as converted shear wave (PS data) separately, resulting in the PP inversion and PS inversions. This facilitates the comparison of the joint inversion estimates with the estimates from PP and PS inversion, and demonstrates the advantage of the joint

---

[2] through evaluation of its eigen values and eigen vectors.

inversion. In the presence of random noise in the data, the joint inversion is more accurate for all parameters and can provide good estimates for both I and J and reasonable estimate for the ρ compared to the PP or PS inversions. However, inverting the compressional data provides the I estimate very similar to those of the joint inversion, and inverting the converted shear data provides J and ρ estimates very similar to those of the joint inversion.

1.7 Thesis Organization

Chapter 1 provides some background detail regarding elastic rock properties and why the inversion program has been solved for the rock properties of compressional impedance, shear impedance and density. Further discussion includes the review of P-wave AVO methods and multi-component seismology. Chapter 1 further discusses the thesis problem description and why the work is a worthwhile extension of the review.

Chapter 2 presents the theory of the 3-parameter joint inversion. Next, using Gardner's rule assumption between the density and the P-wave velocity the 2-parameter joint inversion, which is equivalent to the weighted stacking method of Smith and Gidlow for inverting the compressional data using the least-squares method, is discussed. Then the mathematical background of the SVD method and how the SVD method diagnoses the ill-poseness of the inversion problem is presented. The application of damped SVD for ill-posed problem to provide a good density estimate is examined. Chapter 2 also discusses the derivation of the P-impedance, S-impedance, and density from the P-, S-, and density reflectivity traces, with the missing low frequency trend restored.

In detail Chapter 3 presents the implementation of the AVO joint inversion. The 2- and 3-parameter joint inversion is tested and compared with a few synthetic examples; the advantage of the joint inversion compared to the inversion of compressional or shear data separately, is discussed. The theoretical accuracy of the 3-parameter joint inversion is explored.

Chapter 4 presents, the processing flows of VSP data prior to input to the AVO inversion. The Red Deer study area and data is examined.

In Chapter 5, the modification of the 3-parameter joint inversion for surface data to work with the VSP data is presented. The 3-parameter joint inversion has been applied to the real VSP data. The AVO inversion of the Red Deer walkaway VSP data is an ill-posed problem; the detailed application of damping SVD method to stabilize the problem is presented.

1.8 Data Used

The joint AVO inversion procedure was evaluated using the following datasets.

1.8.1 Synthetic Data

The synthetic PP and PS data of chapter 3 were generated using a multi-offset synthetics seismogram (Lawton and Howell, 1992; Margrave and Foltinek, 1995) and blocked models of depth vs. V_P, V_S and ρ. These models were then raytraced for PP and PS incident angles and amplitudes were calculated using the full non-linear Zoeppritz equations. The resulting PP and PS offset gathers were then used to evaluate the

performance of various joint inversion methods under investigation. The synthetic data of chapter 3 and 4 were generated using sonic and density logs from wells 08-08-23-23W4 of the Blackfoot field, and the Cygnet 9-34-38-28W4 lease.

1.8.2 Red Deer VSP Data

Vertical seismic profile data were acquired at the Cygnet 9-34-38-28W4 lease, located northwest of Red Deer, Alberta, as shown in Figure 1.1. At this location, Suncor Energy Inc., industry partners, and the Alberta research Council, are evaluating the upper Cretaceous Ardley coal zone for its coalbed methane (CBM) potential, as well as testing enhanced coalbed methane recovery with carbon dioxide injection (Richardson, 2003). The acquisition parameters for the Red Deer VSP data are summarized in table 1.1.

Table 1.1: Red Deer 3C-2D acquisition parameter

Zero-offset VSP	
Source Parameters	
Source	Compressional
Source Type	SCHLUMBERGER MINI-VIBE
Sweep Parameter	8-250 Hz, Linear, 9 Sec.
Source Offset	20 m
Source Azimuth	87.7 degrees from true north
Source Elevation	943.48 m
Walk-away VSP	
Source Parameters	
Source	Compressional
Source Type	SCHLUMBERGER MINI-VIBE
Sweep Parameter	8-250 Hz, Linear, 9 Sec.
Source Offset	99.89 m, 149.65 m, 190.8 m, 243.28 m
Source Azimuth	~90 degrees from true north
Source Elevation	943.48 m, 942.67 m, 942.85 m, 943.28 m
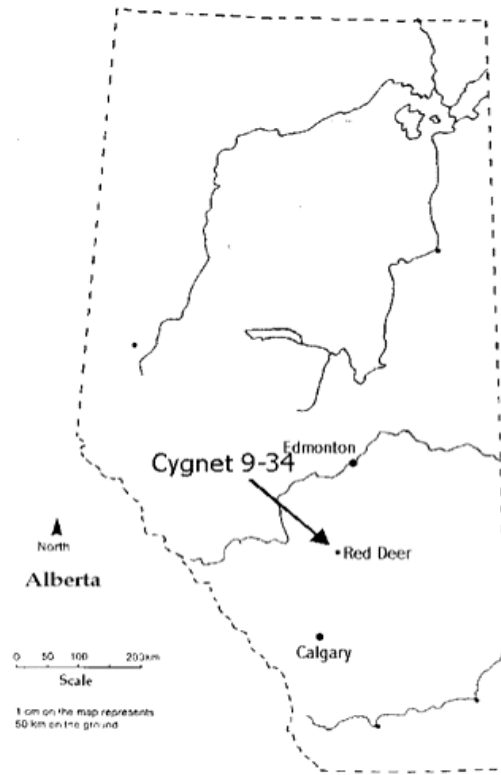
Figure 1.1: A map of Alberta showing the location of Cygnet 9-34-38-28W4 well of Suncor Energy (courtesy of Richardson, 2003).

1.9 Hardware and Software Used

The VSP processing presented in Chapter 5 was done on a SUN MICROSYSTEM network operated by the CREWES Project of the Department of Geology and Geophysics at the University of Calgary. The programming was done in the MATLAB programming language. This includes the PP, PS and joint AVO inversion, well log smoothing, PP and PS conversion to depth, and amplitude scaling of PP and PS data. A number of other MATLAB-based programs coded by Dr. Gary Margrave of the University of Calgary were also utilized in this research. Synthetic data were generated using SYNGRAM, a

seismic modeling package originally developed by Dr. Ed Krebes and Dr. Don Lawton of the University of Calgary, and ported to MATLAB by Dr. Gary Margrave and Mr. Darren Foltinek also of the University of Calgary. The Red Deer 3C-2D VSP data were processed with GEOFRAME software by Larissa Bezouchko of Schlumberger Canada at January 2003. The Red Deer zero-offset Mini-P VSP data were also processed with PROMAX. Processed images (Chapter 4) were screen captured using XV.

CHAPTER 2: Joint AVO Inversion Theory

2.1 Introduction

Smith and Gidlow (1987) showed that the Aki-Richards approximation for the PP reflection coefficient can be used to invert the amplitude of a PP, CMP gather in a weighted stacking scheme for two parameters of P- and S-wave velocity reflectivity ($\Delta\alpha/\alpha$ and $\Delta\beta/\beta$). Also, Stewart (1990) derived the extension of the Smith-Gidlow approach using both PP CMP and PS common-conversion-point (CCP) gathers to estimate $\Delta\alpha/\alpha$ and $\Delta\beta/\beta$. Larsen and Margrave (1999) outlined a least-squares, weighted stacking procedure incorporating both PP and PS gathers to extract P- and S-wave impedance reflectivity, $\Delta I/I$ and $\Delta J/J$. In the weighted stacking method, normal-moveout (NMO) corrected CMP (PP case) and CCP (PS case) gathers are weighted and stacked, and the weights are derived from a smoothed background velocity model. Ferguson and Margrave (1996) presented a method to invert the PS reflectivity to estimate S-wave velocity while restoring the low frequency trend.

I modified the joint inversion to estimate the three parameters $\Delta I/I$, $\Delta J/J$ and $\Delta\rho/\rho$, using the SVD method rather than the normal least-squares method. Then using the

Ferguson and Margrave (1996) method, these three parameter traces are integrated and low frequencies restored, resulting in estimates of *I, J* and ρ.

This chapter presents the theory of the Larsen and Margrave (1999) least-squares method, the Ferguson and Margrave (1996) low frequency restoration method, and the mathematical background of the SVD method is reviewed. SVD is widely used in geophysical inversions and provides a precise way of analyzing a matrix and to yield a stable but approximate inverse. The present joint AVO inversion is based on the Larsen and Margrave (1999) least-squares method.

2.2 The Least-Squares Method

The variation of reflection and transmission coefficients with incidence angle, and thus offset, is commonly known as amplitude versus offset (AVO). The Zoeppritz equations describe the elastic, plane-wave reflection and transmission coefficients as a function of incidence angle and elastic properties of the media (Aki and Richards, 1980). When the changes in elastic properties at the boundary of two layers are small, the relationship between model parameters, impedances and density, and reflection data, is strongly linear. The Aki-Richards (1980) linear approximations for PP and PS reflection coefficients, R_{PP} and R_{PS}, can be formulated as a function of density and P-wave impedance, $I = \rho V_P$ (therefore the P-wave impedance reflectivity will be, $\Delta I / I \approx \Delta V_P / V_P + \Delta \rho / \rho$) and S-wave impedance, $J = \rho V_S$ (therefore, the S-wave impedance reflectivity will be $\Delta J / J \approx \Delta V_S / V_S + \Delta \rho / \rho$) (Larsen and Margrave, 1999),

the resulting expressions are

$$R_{PP} = A(\theta)\frac{\Delta I}{I} + B(\theta)\frac{\Delta J}{J} + C(\theta)\frac{\Delta\rho}{\rho}, \tag{2.1}$$

$$R_{PS} = E(\theta,\varphi)\frac{\Delta J}{J} + D(\theta,\varphi)\frac{\Delta\rho}{\rho}, \tag{2.2}$$

where R_{PP} and R_{PS} are the angle dependent PP and PS reflection coefficients, and ρ is density. The coefficients A, B, C, D and E are functions of the average P-wave incident angle, θ, the average S-wave reflected angle, φ, and the ratio of S-velocity to P-velocity, V_S/V_P, across the interface (Larsen and Margrave 1999) given by

$$A(\theta) = \frac{(1+\tan^2\theta)}{2}, \tag{2.3}$$

$$B(\theta) = -4\frac{V_S^2}{V_P^2}\sin^2\theta, \tag{2.4}$$

$$C(\theta) = -\left(\frac{\tan^2\theta}{2} - 2\frac{V_S^2}{V_P^2}\sin^2\theta\right), \tag{2.5}$$

$$D(\theta,\varphi) = -\frac{V_P\tan\varphi}{2V_S}\left(1+2\sin^2\varphi - 2\frac{V_S}{V_P}\cos\theta\cos\varphi\right), \tag{2.6}$$

and

$$E(\theta,\varphi) = \frac{V_P\tan\varphi}{2V_S}\left(2\sin^2\varphi - 2\frac{V_S}{V_P}\cos\theta\cos\varphi\right). \tag{2.7}$$

Equations (2.1) and (2.2) are reasonable approximations assuming small relative changes in elastic parameters and the angles θ and φ do not approach a critical angle or 90 degrees (Aki and Richards, 1980).

Assuming that the PP and PS reflection data provide estimates of R_{PP} and R_{PS} for a range of source-receiver offsets, the Aki-Richards (1980) approximations for different offsets, at a particular depth under consideration, can be used to express a linear system of $2n$ linear equations[3] (n being the number of source-receiver offsets[4]) with three unknowns as

$$
\begin{bmatrix}
A_1 & B_1 & C_1 \\
& \vdots & \\
A_n & B_n & C_n \\
0 & E_1 & D_1 \\
& \vdots & \\
0 & E_n & D_n
\end{bmatrix}_{2n \times 3}
\begin{bmatrix}
\dfrac{\Delta I}{I} \\
\dfrac{\Delta J}{J} \\
\dfrac{\Delta \rho}{\rho}
\end{bmatrix}
=
\begin{bmatrix}
R_{PP1} \\
\vdots \\
R_{PPn} \\
R_{PS1} \\
\vdots \\
R_{PSn}
\end{bmatrix}_{2n \times 1}
, \tag{2.8}
$$

the above is also a matrix equation which can be written symbolically

$$ G\,m = d, \tag{2.9} $$

where G is the matrix of known coefficients, m, the unknown parameter vector containing $[\Delta I / I \quad \Delta J / J \quad \Delta \rho / \rho]$, and d the input data vector (reflection data from each source-receiver pair at that particular depth). The matrix G is related to the geometry of the problem and not the data itself. Having more data than unknowns when $n > 3$, the system of equations (2.9) has no exact solution. A solution that minimizes the sum squared error, the least-squares solution, is given by:

$$ m = (G^T G)^{-1} G^T d. \tag{2.10} $$

---

[3] There is no need for PP and PS datasets to have the same number of source-receiver offsets. Generally PP and PS can have different offset ranges. Equality was assumed for simplicity in coding the problem.

[4] Avoiding the under-determined system, at least three offsets are needed to have more equations than unknowns.

The general least-squares solution, Equation (2.10), is obtained by minimizing the total squared errors between reflection amplitude data and the model, See Appendix A about the philosophy of least-squares. There is only one such "best" solution and the least-squares method fails if the number of solutions that give the same minimum prediction error is greater than one (uninvertable matrices) (Menke, 1989). The least-squares solution of Equation (2.9) is coded in MATLAB to obtain the estimate of $\Delta I / I$ and $\Delta J / J$.

2.2.1 Two-Parameter Joint Inversion

If Gardner's rule between density and P-wave velocity holds true ($\rho = kV_P^{1/4}$, where k is a constant; Gardner at al., 1974) the density contrast term can be rewritten as a function of P-wave impedance,

$$\frac{\Delta \rho}{\rho} = \frac{1}{5}\frac{\Delta I}{I}. \tag{2.11}$$

Applying this assumption, the Aki-Richards (1980) approximations (Equations (2.1) and (2.2)) are simplified to

$$R_{PP} = A'(\theta)\frac{\Delta I}{I} + B'(\theta)\frac{\Delta J}{J}, \tag{2.12}$$

$$R_{PS} = C'(\theta,\varphi)\frac{\Delta I}{I} + D'(\theta,\varphi)\frac{\Delta J}{J}, \tag{2.13}$$

where the coefficients A, B, C and D are given as follows:

$$A^{'}(\theta) = \frac{1}{2} + \frac{2}{5}(\tan^2\theta + \frac{V_S^2}{V_P^2}\sin^2\theta) \tag{2.14}$$

$$B'(\theta) = -4\frac{V_S^2}{V_P^2}\sin^2\theta, \tag{2.15}$$

$$C'(\theta,\varphi) = \frac{-V_P\tan\varphi}{10V_S}\left(1 + 2\sin^2\varphi - 2\frac{V_S}{V_P}\cos\theta\cos\varphi\right), \tag{2.16}$$

$$D'(\theta,\varphi) = \frac{V_P\tan\varphi}{2V_S}\left(2\sin^2\varphi - 2\frac{V_S}{V_P}\cos\theta\cos\varphi\right). \tag{2.17}$$

Using this constraint for density, the system of equations (2.8) becomes

$$\begin{bmatrix} A_1' & B_1' \\ \vdots & \vdots \\ A_n' & B_n' \\ C_1' & D_1' \\ \vdots & \vdots \\ C_1' & D_1' \end{bmatrix}_{2n\times2} \begin{bmatrix} \dfrac{\Delta I}{I} \\ \dfrac{\Delta J}{J} \end{bmatrix} = \begin{bmatrix} R_{PP1} \\ \vdots \\ R_{PPn} \\ R_{PS1} \\ \vdots \\ R_{PSn} \end{bmatrix}_{2n\times1}. \tag{2.18}$$

The equivalent the matrix equation is

$$G\,m = d, \tag{2.19}$$

where m is the unknown parameter vector containing the impedance reflectivities $[\Delta I/I \quad \Delta J/J]^{\mathrm{T}}$.

Smith and Gidlow's (1987) weighted stacking method is a computationally simpler procedure for performing the least-squares curve fitting of Equation (2.12) to the PP reflection amplitudes, as in the extension by Stewart (1990) and Larsen and Margrave (1999).

2.2.2 Weighted Stacking Method

Larsen and Margrave (1999) expanded the least-squares solution of the system of

equations (2.19) and calculated the estimates of ΔI and ΔJ as:

$$\frac{\Delta I}{I} = \sum_{i=1}^{n} W_{IPP} \ R_{PPi} + \sum_{i=1}^{n} W_{IPS} \ R_{PSi}, \qquad (2.20)$$

$$\frac{\Delta J}{J} = \sum_{i=1}^{n} W_{JPP} \ R_{PPi} + \sum_{i=1}^{n} W_{JPS} \ R_{PSi}. \qquad (2.21)$$

The weights W_{IPP}, W_{IPS}, W_{JPP} and W_{JPS} are given in Appendix B. Equations (2.20) and (2.21) are used to estimate $\Delta I / I$ and $\Delta J / J$ with the weighted stacking scheme in this thesis. Although the least-squares and weighted stacking methods are basically the same, the weighted stacking is examined due to the fact that it gives information about the contribution of PP and PS datasets in I and J estimates.

2.3 Three-Parameter Joint Inversion

3-parameter inversion seeks the three unknown model parameters I, J and ρ. However, many theoretical and numerical studies have demonstrated that by using offset limited data, the two impedances and density can not unambiguously resolved (Tarantola, 1986; Debski and Tarantola, 1995, Jin, et al. 2002). To overcome this problem the stability of the system of equations (2.9) must be known. In fact, the result of AVO inversion is first affected by the processing steps which transform the recorded seismic data into reflection coefficients, however the other important factor is the inherent instability of the linear system (2.9). This instability persists even when the processing related errors are removed (Jin, et al., 2002). This problem becomes worse as the range of angles used in the inversion becomes smaller. Various authors (Shuey (1985), Smith and

Gidlow (1987), and Fatti at al. (1994), among others) rearranged the Equations (2.1) and (2.2) to solve for better parameterizations. In implementing these schemes, hard constraints are usually implemented either explicitly or implicitly to improve the stability of the problem. As discussed in Section 2.2.1, Smith and Gidlow (1987) use Gardner's rule (Gardner et al., 1974) to remove the density term, thus improving the stability of the problem. Shuey (1985) and Fatti et al. (1994) both solved the Equations (2.1) and (2.2) using only the impedance terms, implicitly constraining the density reflectivity term to zero (Downton and Lines, 2001). Jin et al., (1993) showed that singular value decomposition (SVD) can be effectively used for AVO stabilization. The main benefit of SVD is to provide a precise way of analyzing a matrix, and to yield a stable but approximate inverse. SVD is widely used in geophysical inversions and in this thesis the SVD technique has been used in a 3-parameter AVO inversion.

2.4 SVD Analysis

Singular value decomposition, SVD is a common and precise way of solving linear least-squares problems (Sheriff, 1991). For a general matrix G of order $n \times m$ [5] which is a map from the model space $S(m)$, to the data space $S(d)$, there is always a matrix decomposition called the singular value decomposition (SVD) of matrix G. Singular value decomposition allows the matrix G to be expressed as the product of three matrices (Lay, 1996),

$$G = U \Lambda V^T ,\qquad\qquad (2.22)$$

where $U_{m \times m}$ is the matrix of eigenvectors[6] of GG^T that span the data space, and $V_{n \times n}$ is

the matrix of eigenvectors of the $G^T G$ that span the model space. The *singular values* of

the matrix G are the positive square roots of the eigenvalues[7] of the matrix $G^T G$. $\Lambda_{m \times n}$ is

a matrix with the singular values of the matrix G in its main diagonal elements in a

decreasing order, as

$$\Lambda = \begin{bmatrix} \sigma_1 & 0 & \cdots & 0 \\ 0 & \sigma_2 & 0 & \cdots \\ \vdots & 0 & \ddots & 0 \\ 0 & \cdots & 0 & \sigma_m \end{bmatrix}_{n \times m} \tag{2.23}$$

$$\sigma_1 \geq \sigma_2 \geq \cdots \geq \sigma_m \geq 0.$$

Menke (1989) showed that the SVD of matrix G becomes

$$G = U \Lambda V^T = U_p \Lambda_p V_p^T, \tag{2.24}$$

where the matrices $U_P = [u_1 \ldots u_p] \in \mathbb{R}^{p \times p}$ and $V_P = [v_1 \ldots v_p] \in \mathbb{R}^{n \times p}$ consist of the first p

columns of U and V, related to non-zero singular values. $\Lambda_{p \times p}$ is a diagonal matrix

with the non-zero singular values of the matrix G in diagonal elements. In the inversion

calculations Equation (2.24) is used, which is a reduced SVD. The vectors of matrices

U_p and V_p are orthogonal,

$$V_p^T V_p = U_p^T U_p = I_{p \times p}. \tag{2.25}$$

---

[5] The matrix G in the 3-parameter joint inversion is of order $2n \times 3$.
[6] An eigenvector of an $n \times n$ matrix A is a nonzero vector x such that $Ax = \lambda x$.
[7] An **eigenvector** of an $n \times n$ matrix A is a nonzero vector **x** such that $Ax = \lambda x$ for some scalar λ.

The SVD of matrix G always exists due to the existence of matrices U, V and Λ (Lay, 1996). Since the diagonal entries in matrix Λ_p are nonzero, the generalized inverse, also called the Lanczos inverse, of matrix G is defined as (Lay, 1996)

$$G_g^{-1} = V_p \Lambda_p^{-1} U_p^T = V_p \left[diag \left(\frac{1}{\sigma_p} \right) \right] U_p^T. \tag{2.26}$$

For the generalized inverse matrix in Equation (2.26), the following equations hold

$$G_g^{-1} G G_g^{-1} = G_g^{-1}, \tag{2.27}$$

$$G G_g^{-1} G = G. \tag{2.28}$$

In the 3-parameter AVO inversion, the generalized inverse of matrix G with the order of $2n \times 3$ has been sought. Applying the generalized matrix G_g^{-1} to both sides of Equation (2.9), we will have

$$G_g^{-1} G m = G_g^{-1} d. \tag{2.29}$$

Equivalently from Equation (2.27), Equation (2.29) becomes

$$G_g^{-1} G m = G_g^{-1} G G_g^{-1} d. \tag{2.30}$$

Then the estimated solution vector m^{est} will be obtained as

$$m^{est} = G_g^{-1} d. \tag{2.31}$$

By the definition of the generalized inverse of a matrix, Equation (2.26), Equation (2.31) becomes

$$m^{est} = V_p \Lambda_p^{-1} U_p^T d. \tag{2.32}$$

Knowing the matrices U_p, V_p and Λ_p from the SVD of matrix G, the generalized inverse matrix, G_g^{-1}, can be constructed. Consequently, the solution parameter vector m^{est} is obtained from Equation (2.32).

From Equations (2.31) and (2.9), the estimated solution becomes:

$$m^{est} = G_g^{-1}d \cong (G_g^{-1}G)m = (V_p V_p^T)m, \tag{2.33}$$

with the 3×3 matrix $G_g^{-1}G$ being called the *model resolution* matrix,

$$R = G_g^{-1}G = V_P V_p^T, \tag{2.34}$$

for the generalized inverse operator (Krebes, 2004, Jackson, 1972, Menke, 1989, among others). The model resolution matrix defines how well the estimated solution, m^{est} resolves the true solution m. For perfect resolution, the resolution matrix would be the identity matrix. The diagonal elements of a resolution matrix are good measures of the model resolution. The non-unit diagonal elements imply that the estimates are linear combinations of the true values.

The variance of the kth estimated solution is calculated as (Jackson, 1972):

$$\text{var}(m_k^{est}) = \sum_{i=1}^{2n} G_{gki}^{-2} \, \text{var}(d_i). \tag{2.35}$$

For statistically independent data with unit variance, using Equations (2.26) and (2.25), the variance becomes (Jackson, 1972):

$$\text{var}(m_k^{est}) = \sum_{j=1}^{p} \left(\frac{V_{pkj}}{\sigma_j} \right)^2. \tag{2.36}$$

The Equation (2.36) allows us to examine the error of each model parameter m_k^{est} individually.

Any possible instability in the numerical calculation of m^{est}, is identified in matrix Λ. The only potential difficulty in using SVD is when inverting a matrix that possesses some very small singular values. If a singular value σ_j is small, the inverse of it becomes large and is dominated by numerical round off error, which is undesirable. As Menke (1989) states "*One solution to this problem is to pick some cutoff size for singular values and then consider any values smaller than this value as equal to zero. When small singular values are excluded, the solution is generally close to the natural solution and possesses better variance. Or instead of choosing a sharp cutoff for the singular values, it is possible to include all the singular values while damping the smaller ones. This change has little effect on the larger eigenvalues but prevents the smaller ones from leading to large variances*". These approaches for avoiding instabilities have the analogs in digital filtering of band-pass filtering and prewhitening; it is not clear which one is better. Both approaches had been tested in this thesis; however choosing a cutoff size for singular values failed for the Red Deer case study.

Therefore, if some of the singular values of matrix G are extremely small, numerical round off errors are almost inevitable. The damped generalized inverse is defined as (Krebes, 2004):

$$G_g^{-1} = V_p \Lambda_p (\Lambda_p^{\ 2} + \varepsilon^2 I \,)^{-1} U_p^{\ T}. \qquad (2.37)$$

and the model resolution matrix become

$$R = V_p \Lambda_p^2 (\Lambda_p^2 + \varepsilon^2 I)^{-1} V_p^T, \tag{2.38}$$

which reduces to the usual model resolution matrix when $\varepsilon = 0$. Also, the variance of the kth estimated solution for damped SVD becomes

$$\mathrm{var}(m_k^{est}) = \sum_{j=1}^{p} \left(V_{pkj} \frac{\sigma_j}{\sigma_j^2 + \varepsilon^2} \right)^2. \tag{2.39}$$

Non-zero ε implies less resolution (Equation (2.38)), but a more stable solution is obtained due to the lower variance of the estimated solutions (Equation (2.39)) and a better inverse, as is achieved in Equation (2.37).

The precise value of damping factor must be chosen by a trial-and error process which weighs the relative merits of having a solution with small variance against one that is well resolved (Menke, 1989). There is always a trade-off between resolution and variance in the estimation of the unknown parameter. For the price of less variance, less resolution of model parameters is achieved. A great deal of care should be exercised in choosing the appropriate value of the damping factor. The ability to make any reliable interpretation from unknown parameters m^{est} may be limited either by lack of resolution, or by large variance (Jackson, 1972).

The ratio of the largest to the smallest singular values is the condition number of a matrix, which is a measure of the singularity of the matrix. A matrix is well-posed when its condition number is not far from 1 (Jin at al., 2002), and an ill-posed matrix is a matrix with very large condition number. In SVD analysis of the AVO inversion the condition number has been examined as an indicator of the singularity of the matrix. A

singular matrix is a square matrix which is invertible, by its mathematical definition. A non-square invertible matrix is called rank-deficient matrix. However, in this thesis the singular term is used for all invertible matrixes either square or non-square.

The SVD solution of Equation (2.9) is also a least-squares solution (Jackson, 1972 and Lay 1996). In general, SVD finds the least-squares best compromise solution (Press et al., 1992). The advantage of using SVD over a normal least-squares method is in dealing with matrices that are either singular or else numerically very close to singular. SVD will diagnose when a matrix is singular or near singular, and a damped SVD gives a stable numerical answer.

In amplitude versus offset or AVO analysis using offset limited data, two impedances and density can not be unambiguously resolved (Tarantola, 1986; Dębski and Tarantola, 1995, Jin, et al. 2002). Avoiding this ambiguous, in this thesis the damped SVD has been used to invert a near singular matrix for $\Delta I/I$, $\Delta J/J$ and $\Delta\rho/\rho$ while avoiding numerical round off errors. At the next step the band-limited $\Delta I/I$, $\Delta J/J$ and $\Delta\rho/\rho$ traces are integrated using the BLIMP routine to obtain the broad-band I, J and ρ estimates.

2.5 BLIMP, Band Limited IMPedance Inversion

Missing low-frequency components are a common occurrence in seismic data. The main reasons include: band-limited seismic sources and using band-pass filters in data recording and processing. Band-pass filters are usually applied to data to eliminate the low-frequency ground-roll or coherent high frequency noise. In this process some desired low-frequency data is lost. Inversion of such band-limited data results in band-limited

impedance. Lindseth (1979) stated that the inversion of the reflection coefficient leads to band-limited velocity estimation (here impedance). The moderately high-frequency reflection components are recoverable by proper acquisition and data processing; the very low frequencies, representing the gross velocity information, must be obtained elsewhere. Lindseth (1979) used the interval velocity analyses or sonic log data to recover the missing low-frequency components. Waters (1987) described an inversion scheme to estimate impedance values from PP seismic data, while preserving the low-frequency content. Ferguson and Margrave (1996) extended Water's (1978) method to a band-limited impedance inversion which has been implemented as a MATLAB algorithm, called BLIMP (Band-Limited IMPedance inversion).

The solution of Equation (2.9) or equivalently the solutions of equations (2.20) and (2.21), the estimated reflectivity traces, *ΔI/I(z)*, *ΔJ/J(z)* and *Δρ/ρ(z)* are integrated in depth to estimate the *I*, *J* and *ρ*, while including the missing low-frequency components using the BLIMP routine.

The BLIMP routine uses a reference impedance log from a velocity-model (or interval velocity) to provide the missing low-frequency components of the input reflectivity trace. The reflectivity trace is integrated and exponentiated, resulting in a band-limited impedance estimate; the method is explained in Appendix C. A brief review of how to compensate for the low frequency components as stated by Ferguson and Margrave (1996) is

      1. Compute the linear trend of the impedance log calculated from sonic logs.

2. Subtract the linear trend from the impedance log.

3. Compute the Fourier spectrum of step (2).

4. Apply a band-limited integration filter to the reflectivity trace and exponentiate the result. The result is a band-limited impedance estimate.

5. Compute the Fourier spectrum of step (4).

6. Determine a scalar to match the mean magnitude of (5) and (3) over the seismic signal band.

7. Multiply the spectrum of (5) by the scalar from (6).

8. Low-pass filter (3) and add the result to (7).

9. Inverse Fourier transform (8).

10. Add the linear trend from (1) to (9).

The joint inversion program uses the input PP and PS data in depth, as will be discussed in section 3.1.3. Thus the frequency content of these data are described by k_z, the spatial frequency. The minimum and maximum of k_z required for restoring the low frequency components is input by the user.

2.6 PP and PS Inversion

To examine the PP or PS data contribution in each I, J and ρ estimates in the joint inversion, each dataset alone is used as input to the inversion, resulting in the PP inversion or PS inversion methods. Also, to investigate the advantages of combining PP and PS data in the joint inversion, the inversion only of each datasets alone is considered.

2.7 Chapter Summary

The theory of 2- and 3-parameter least-squares joint inversion and the mathematical background of the SVD method are reviewed. The SVD method is used in the joint inversion of PP and PS gathers to estimate $\Delta I/I$, $\Delta J/J$ and $\Delta\rho/\rho$. These three reflectivity traces are inverted to obtain I, J and ρ estimates, restoring low frequency components obtained by using BLIMP routine. The SVD method gives the best least-squares solution and is the same as the least-squares method for well-posed matrices. The damped SVD method can be used to stablize the inversion results for the ill-posed problems.

CHAPTER 3: AVO Inversion Implementation and Testing on Synthetic Data

3.1 Introduction

Smith and Gidlow (1987) gave a detailed explanation of their weighted stacking method of inverting the compressional data. The joint inversion testing of some synthetic and real examples were presented by Larsen and Margrave (1999) and Margrave et al., 2001, for Blackfoot field, and Zhang and Margrave 2003 for Pikes Peak oilfield.

The implementation and testing of the linear 2- and 3-parameter AVO inversion on a few synthetic data are presented in this chapter.

The implementation includes the smoothing of the background velocity, raytracing, conversion of data from time to depth, and scaling of the data amplitude. The performances of the 2- and 3-parameter PP, PS and the joint inversion, have been compared; the condition number plots from SVD analysis of AVO inversions, as a measure of the singularity of a matrix, is examined.

3.2 Practical Implementation Steps

The joint inversion program requires five sources of data and five processing steps

(Figure 3.1). The required data are: background P- and S-wave velocity-depth models,

a density-depth model and a PP and a PS reflection data set (in two way time). The

background P and S-wave velocity-depth models are smoothed and ray-traced to provide

the angles needed for the Aki-Richards coefficients to construct the matrix G, as in

Equation (2.8). The PP and PS datasets are converted from time to depth in order to be

correlated (Section 3.2.4), and scaled to represent the reflectivity (Section 3.2.5). Then,

by using the normal least-squares or SVD method, the PP and PS data are jointly inverted

to obtain the compressional, converted wave impedance and density reflectivity; then the

reflectivity traces are integrated to estimate the P- and S-impedance and density using the

BLIMP routine. Additionally, PP data or PS data alone can be used as an input, resulting

in a PP or PS inversion.
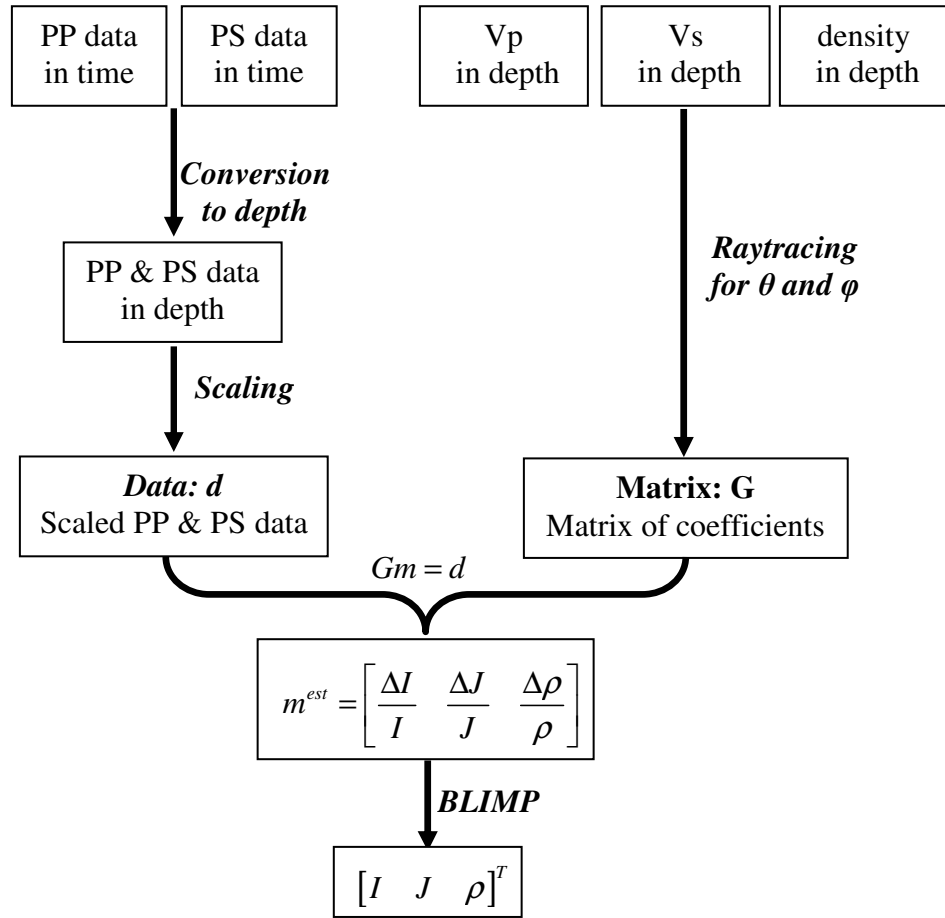
Figure 3.1: Workflow for the joint AVO inversion

The joint inversion solves Equation (2.9) to estimate the reflectivities. In this regard, the matrix G (Equation (2.8)), needs to be determined. At each sample depth under consideration, the coefficients A, B, C, D and E of Equations (2.3)–(2.7), are functions of the P-incident and PS-reflection angles, and also the V_S / V_P ratio. Raytracing is performed on a smooth background velocity model to obtain the necessary angles. The following sections detail the steps necessary for the joint inversion.

3.2.1 Smoothing background velocity

Raytracing to provide the angles of incidence and reflection should be done using a

smooth background interval velocity (provided from well logs or velocity analysis). The interval velocity function is generally not available in detail, and therefore a smooth interval velocity is used to simulate the real conditions. For the case of using well log for the interval velocity, the smoothed velocity should be geologically representative and over smoothing is not desired either; also generally interval velocity derived from a velocity analysis doesn't need to be smoothed. Appendix E gives a simple algorithm of smoothing the background velocity in the MATLAB program.

3.2.2 Raytracing

Assuming there is horizontal layering with no lateral velocity variation, raytracing provides the required angles of incidence and reflection at each sample depth for each receiver location. PP and PS raytracing is undertaken on a smooth interval velocity by the MATLAB routines TRACERAY-PP and TRACERAY-PS (from CREWES MATLAB library). In raytracing, the velocity model needs to be extended to ground level. The interval velocity is generally not available in detail, and therefore a smoothed velocity model is used to simulate the real conditions. The P incident angles are different for the PP and PS reflections, given the same set of source-receiver pairs.

3.2.3 Treatment of the V_S / V_P Factor

V_S / V_P, ratio of the S-wave to P-wave velocity, is needed to determine the Aki-Richards coefficients (Equations (2.3)–(2.7)). In joint inversion, if the S-wave velocity

model is not provided the "mudrock line" relation is used. The Mudrock line is a relation for water-saturated clastic silicate rocks provided in Castagna et al. (1985) as

$$V_P = 1360 + 1.16V_S \text{ (velocities in m/s)}. \tag{3.1}$$

This, with the smooth P-wave velocity model, will provide a value of V_S / V_P for each sample depth of the CMP gather. Equation (3.1) is not a 'universal' equation, and a different relation may be appropriate for a specific area.

3.2.4 Time-to-Depth Conversion of PP and PS Data

In the joint inversion, PP and PS data must be aligned unambiguously in time or depth. The improper correlation of the PP and PS data is one of the most severe error sources in the joint inversion. Zhang and Margrave (2003) carried out the event correlation in time in such a way that the same reflections occur at the same PP travel time in both data sets. For the first step, post-stack time migration of the limited-offset-stacks of the PP and PS data (the limited-offset-stacks are explained later) was done. Secondly, correlation of the PP and PS limited offset stacks in PP time is performed, and the data are flattened to a certain event. After the matching, they carried out the depth conversion. An event correlation may be accomplished by tying the PP and PS data (in depth) to PP and PS synthetic seismograms from well logs (Zhang and Margrave, 2003), or, as stated by Larsen and Margrave (1999), given a sufficiently detailed velocity-depth model, the time-migrated PP and PS data can then be converted to depth and directly correlated relative to a common datum or horizon. Two possible methods of PP and PS

data correlation are:

1: Post-stack or pre-stack time migration and subsequently depth conversion.

2: Direct pre-stack depth migration.

However, for complex real data, it is possible that the PP and PS data still do not correlate in depth, and some other event correlation technique might be needed. However, for a simple horizontally layered geology, the PP and PS data in depth should correlate.

In this thesis, to focus on event correlation, a procedure to convert both datasets from time to depth has been followed; since only synthetic data and a horizontally layered real data were tested, time-migration was not needed. The process of converting the PP and PS datasets from time to depth follows a relatively simple procedure. A program was written in MATLAB to perform the time-to-depth conversion for the synthetic surface seismic datasets[8]. With the velocity-depth model, the time-depth curve can be constructed; the time-depth curve is then used to manipulate the time-depth conversion of the PP and PS datasets. The PP and PS events have been linearly interpolated using the previously obtained time-depth curve. Appendix D gives a simple algorithm of the time-to-depth conversion in the MATLAB program. In time-to-depth conversion of VSP data (Chapter 4 and 5) the first break times are used as the time-depth curve.

Generally, for a large volume of real datasets, converting the PP and PS data from time to depth requires a pre-stack depth migration or a pre-stack time migration followed

---

[8] The time-to-depth conversion of real VSP data is presented in Chapter 4.

by a depth conversion. Pre-stack migration is computationally intensive and can be time-consuming. In order to decrease the amount of data in pre-stack migration, a more practical approach has been developed. Larsen and Margrave (1999) and Zhang and Margrave (2003) rearranged the CMP and CCP gathers into limited-offset-stacks. They used different overlapping bins in rearranging the data into limited-offset-stacks. A limited-offset stack trace is the result of stacking NMO-corrected PP or PS traces from a limited range of offsets (a bin), and represents the mean offset for traces which were stacked. The stacks are migrated first and then input to the inversion program, rather than performing a full pre-stack migration, allow limited-offset stack traces to be post-stack migrated. This reduces the expense of the inversion, but it might decrease the accuracy of the result.

3.2.5 Scaling the PP and PS Amplitude to Represent the Reflectivity

In an AVO inversion, using the amplitudes of the PP and PS reflection data as estimates of R_{PP} and R_{PS}, it must be required that the amplitudes represent a good approximation to the reflectivity. To obtain the true reflectivity amplitudes even on data which have a true-amplitude recovery in regular processing prior to the inversion, amplitude scaling is still needed. To correct the amplitude prior to the joint inversion, Larsen and Margrave (1999) and Zhang and Margrave (2003) created synthetic seismograms for the PP and PS data from the well logs to compute the average expected amplitude. The processed PP and PS data were then adjusted to have the same RMS amplitude as the synthetic data; the amplitude scalars are functions of offset but

independent of time (Zhang and Margrave 2003).

In this thesis, the root mean square (RMS) amplitude of the PP data is matched by the RMS amplitude of the trace ($\Delta I / 2I$) calculated from the well logs over the seismic band. Similarly, the RMS amplitude of the PS data is matched by the RMS amplitude of the trace ($\Delta J / 2J - \Delta I / 2I$) calculated from well logs. The following explains why these traces have been chosen to scale the PP and PS amplitudes.

The PP reflection coefficient for a normal incidence reflection across an interface is

$$R_{PP}(\theta = 0) = \frac{I_2 - I_1}{I_2 + I_1} = \frac{1}{2}\frac{\Delta I}{I}, \tag{3.2}$$

where I_1 and I_2 are the P- wave impedances in the first and second layer, ΔI is the impedance difference across the interface, and I is the averaged impedance across the interface. The RMS magnitude of the normal incidence R_{PP}, or ($\Delta I / 2I$) is the average expected amplitude of the PP data for the small-incidence angle reflections. The RMS spectrum of $\Delta I / 2I$ (calculated from well logs) over the seismic frequency band width is used as the reference to scale the PP data.

By an empirical relationship, an approximation suitable for R_{PS} for pre-critical incident angles is

$$R_{PS} \cong -R_{PP} - R_{SS}. \tag{3.3}$$

This relation is reasonable assuming the Aki-Richards approximations and the ratio of V_P / V_S is constant. Appendix F gives a numerical derivation for the Equation (3.3). From the Zoeppritz equations, the SS reflection coefficient for the normal incident reflection

across an interface is

$$R_{SS}(\theta = 0) = -\frac{J_2 - J_1}{J_2 + J_1} = -\frac{1}{2}\frac{\Delta J}{J}.$$ (3.4)

Consequently, from Equation (3.3) a suitable approximation for R_{PS} would be

$$R_{PS} = \frac{1}{2}(\frac{\Delta J}{J} - \frac{\Delta I}{I}).$$ (3.5)

The RMS spectrum of ($\Delta J / 2J - \Delta I / 2I$), calculated from well logs over the seismic frequency band width is used as the reference to scale the PS data. The following formulas have been applied to calculate the scalar for each dataset

$$PP\ scalar = \frac{RMS\ of\ (\Delta I / 2I)\ spectrum}{RMS\ of\ the\ first\ PP\ trace\ spectrum},$$ (3.6)

$$PS\ scalar = \frac{RMS\ of\ (\Delta J / 2J - \Delta I / 2I)\ spectrum}{RMS\ of\ the\ second\ PS\ trace\ spectrum}.$$ (3.7)

Then, the scaled PP and PS data is the inverse Fourier transform of the spectrum below

$$spectrum\ of\ scaled\ PP\ data\ =\ spectrum\ of\ data\ \times\ PP\ scalar,$$ (3.8)

$$spectrum\ of\ scaled\ PS\ data\ =\ spectrum\ of\ data\ \times\ PS\ scalar.$$ (3.9)

In the testing of the joint inversion method on synthetic data, the PP and PS amplitude corrections are not applied, and only the real VSP data in Chapter 5 was amplitude corrected.

The testing of the 2-parameter joint inversion for I and J estimates for a few synthetic examples are presented in the next section. The rest of the chapter will examine the testing of the 3-parameter joint inversion for I, J and ρ estimates.

3.3 Two-Parameter Inversion Testing

Several synthetic models have been used to test the joint inversion algorithm. The PP and PS synthetics, created by using SYNGRAM, have reflection amplitudes computed with the exact Zoeppritz equations and primaries only (no multiples), and do not include transmission losses or spherical spreading. As well, NMO is removed; but moveout stretch effects are present. The problem of NMO stretch can be obviated using the inversion approach advocated by Downton and Lines (2001). The synthetic PP and PS sections are in time. Both seismograms were created initially as broad-band responses and then convolved with the appropriate wavelet. The 2-parameter joint inversion results for the three synthetic data examples are presented. The first example is an ideal and well-posed inversion example with a typical blocky velocity model. The second example, also well posed, uses real well logs (as the velocity model) obtained from the Blackfoot field. The third example, ill-posed at the interested zone, has a blocky velocity model from the Red Deer coal bed methane site; the AVO inversion of the real VSP data of third example is presented in Chapter 5.
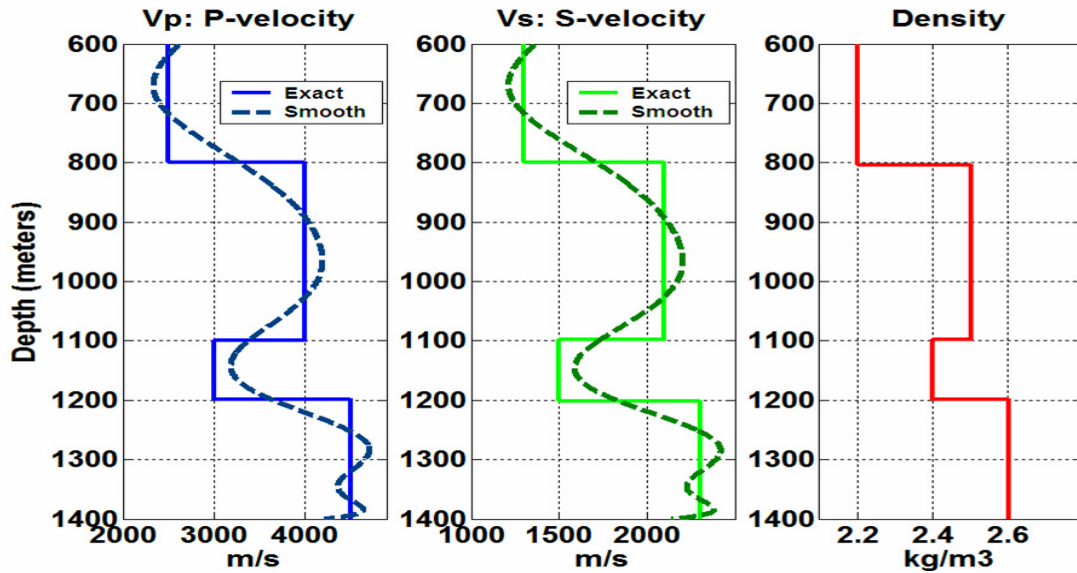
Figure 3.2: Synthetic 1, velocity-depth model.

3.3.1 Synthetic 1; Well-Posed Example

Figure 3.2 shows the first velocity-depth model, in which the density model obeys Gardner's rule and the S-wave velocity obeys Mudrock line relation (the V_P/V_S ratio is not constant). This figure also illustrates the smoothed P- and S-velocities given in the raytracing. The PP and PS synthetic for this velocity model are displayed in Figures 3.3 and 3.4. Both the PP and PS synthetic have an initial 5-10-80-100 Hz zero-phase wavelet, and the same offset range from 0 to 500 m. In real seismic sections, the PP and PS data have different frequency content; typically PS data have less frequency content compared to PP data. Although, taking an initial 5-10-80-100 Hz zero-phase wavelet for both PP and PS synthetics is not realistic, but this initial wavelet has only been used for simplicity. Three reflection events based on the velocity model (Figure 3.2) can easily be recognized in both the PP and PS synthetic datasets.
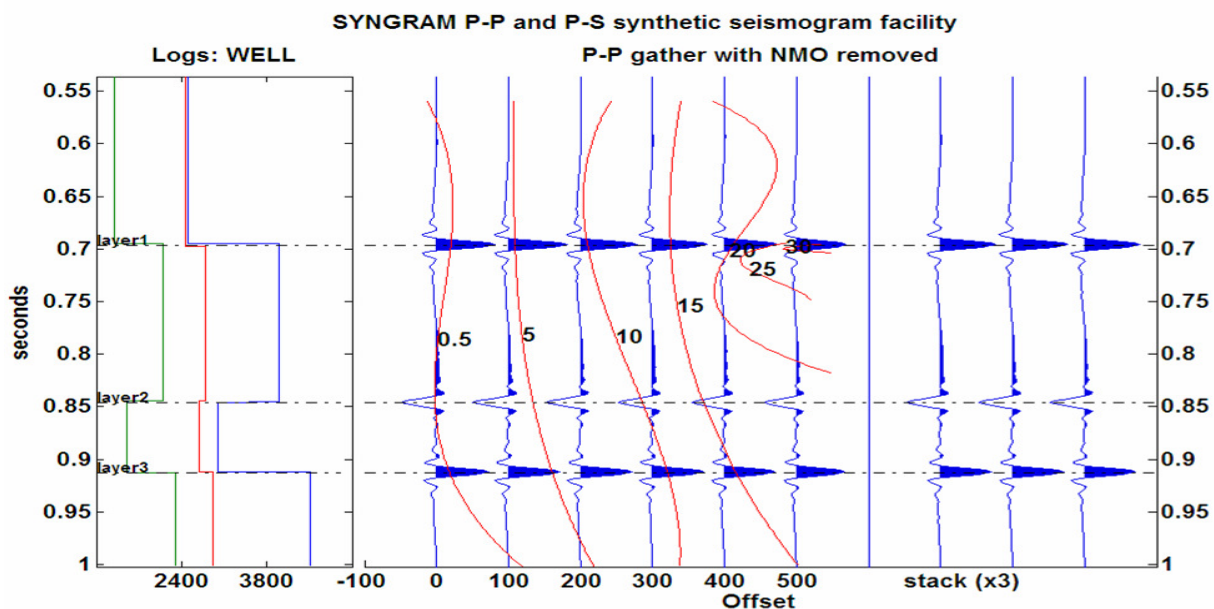
Figure 3.3: Synthetic PP gather from the velocity model in Figure 3.2 in PP time. The three traces on the right are three repetitions of the stacked trace. The contours of incident angles (degrees) of PP rays are displayed.
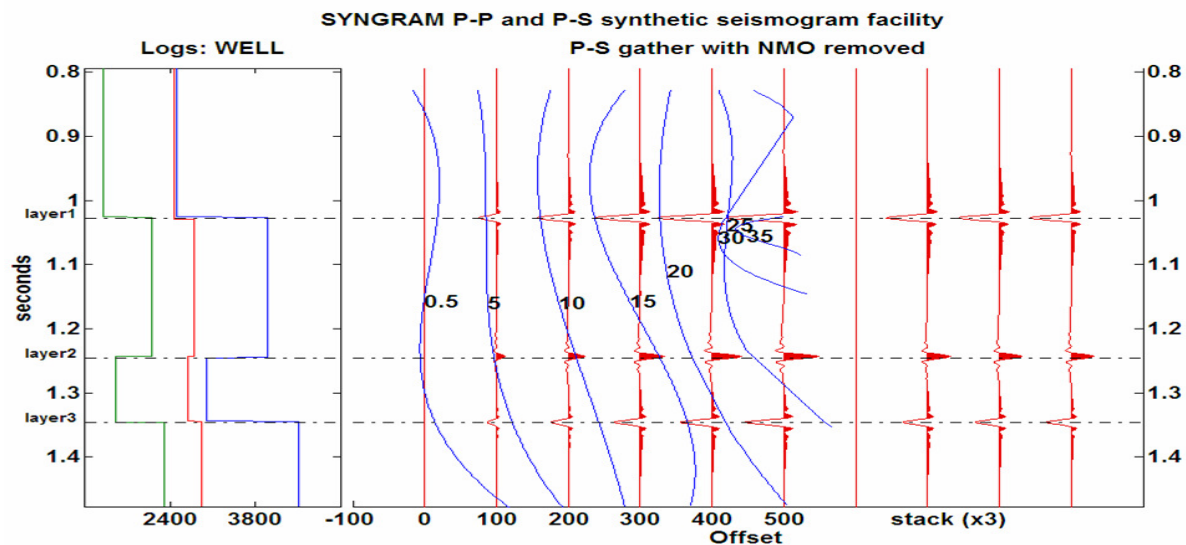
Figure 3.4: Synthetic PS gather from the velocity model in Figure 3.2, in PS time. The three traces on the right are three repetitions of the stacked trace. The contours of incident angles (degrees) of PS rays are displayed.

As an indicator to the singularity of the inversion problem the condition number (Section 2.4) is examined. A high condition number indicates the ill-posdness of the inversion. Figure 3.5 -Figure 3.6 show the two singular values versus the depth from the 2-parameter joint, PP and PS inversions of the synthetic 1, for the *I* and *J*. In singular value plots, below, the condition number of the matrix is shown in red and the righthand vertical axis shows its value, while the singular value plots are shown in red the lefthand vertical axis shows the magnitude of the singular values.
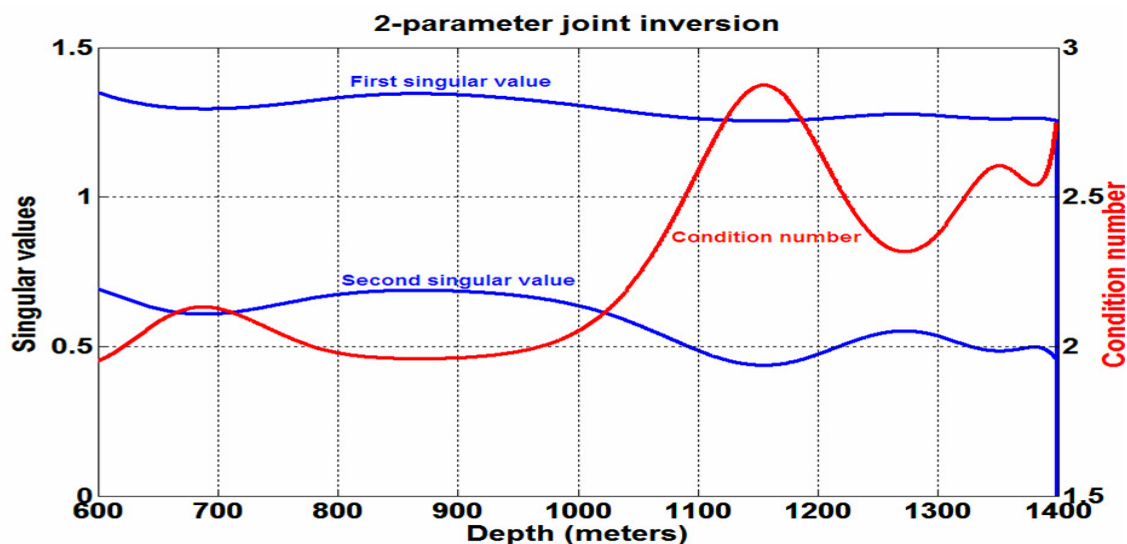
Figure 3.5: Singular values (in blue) and the condition number (red curve) versus depth, of the 2-parameter joint inversion only of synthetic 1, for *I* and *J*.

Inverting the PP data alone shows a reasonable inversion process with the condition number from 10-25 over the depth range; while, in the PS inversion, the condition number varies from 100-300 (Figure 3.6). The high condition number indicates that the

PS inversion is not well-posed for all depths. This example demonstrates the relative inadequacy of the PS inversion which would show instability and unrealistic *I* and *J* estimates.
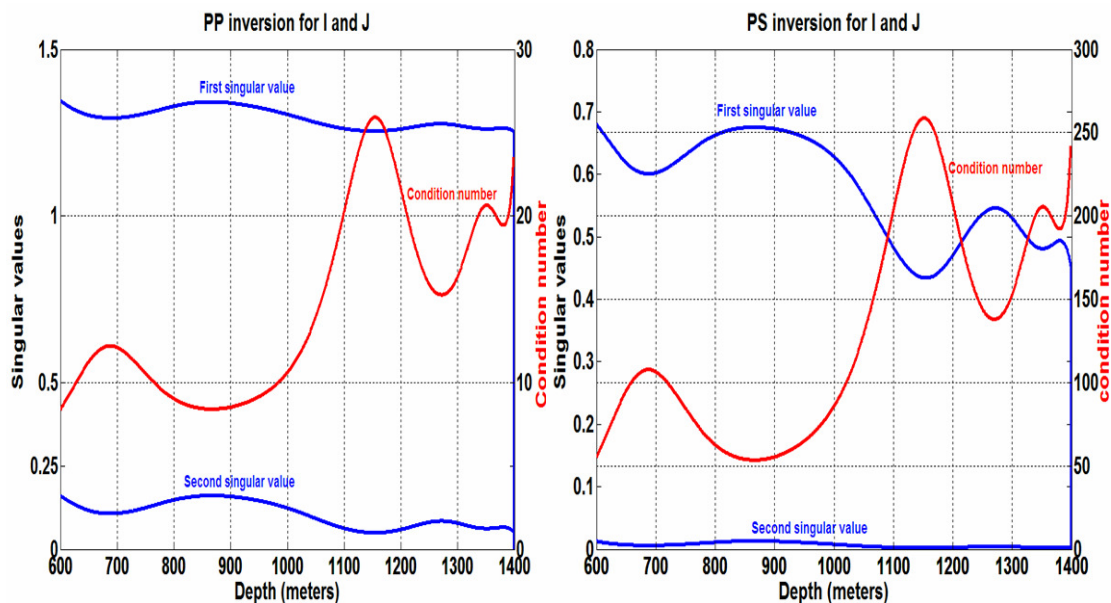
Figure 3.6: Singular values (in blue) and the condition number (red curve) versus depth, of the 2-parameter PP inversion of synthetic 1, for *I* and *J*.

The 2-parameter joint inversion has a small condition number between 2-3 versus depth (Figure 3.5), indicating that joint inversion produces more accurate and stable results compared to the PP and PS inversion. Figure 3.7 shows the estimate of impedances from the 2-parameter PP, PS and the joint inversion; the advantages of using the joint inversion is hard to be judged by the results due to the simplicity of the synthetics 1 model, it has results similar to the PP inversion. However, the condition number analysis has shown the advantage of the application of the joint inversion. As we expected from the condition number plots, the PP and the joint inversion provide better,

more stable results for both the *I* and the *J* estimate (Figure 3.8), than the PS inversion

does. However, the PS inversion produces a good estimate for *J* which is very similar to

the joint inversion, which means that PS inversion estimates *J* better than *I.*
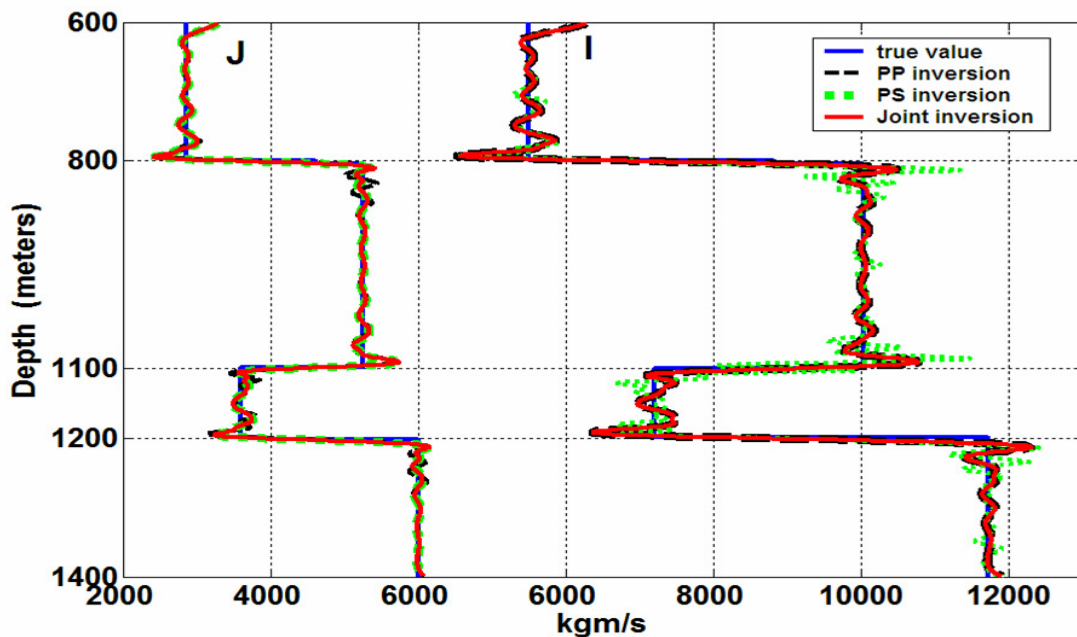
Figure 3.7: P-impedance, *I* and S-impedance: *J,* estimate from PP, PS and joint inversion by the SVD method.

To examine the effect of larger angle coverage in the inversion results, the joint

inversion of the synthetic 1 example, with an offset range between 0-1000 m, is

presented. The PP and PS synthetic are shown in Figure 3.8. Figure 3.9 shows the

condition number plot from the 2-parameter joint inversion of 0-1000 m offset data sets.

The righthand of Figure 3.9 shows the condition number plots from the 2-parameter joint

inversion of 0-500 and 0-1000 m offset data. Figure 3.9 demonstrates that the inversion is

less stable at a depth of 700-1000 m, which is due to the fact that the incident angle

exceeds the critical angle at this depth range. For example at the depth of 800 m, the critical angle is 35 degrees. Angle contours in Figure 3.8 indicate the inversion of a few data beyond the critical angle at this depth range; near critical angle, the linear Aki-Richards equations does not hold and will lead to an incorrect inversion.
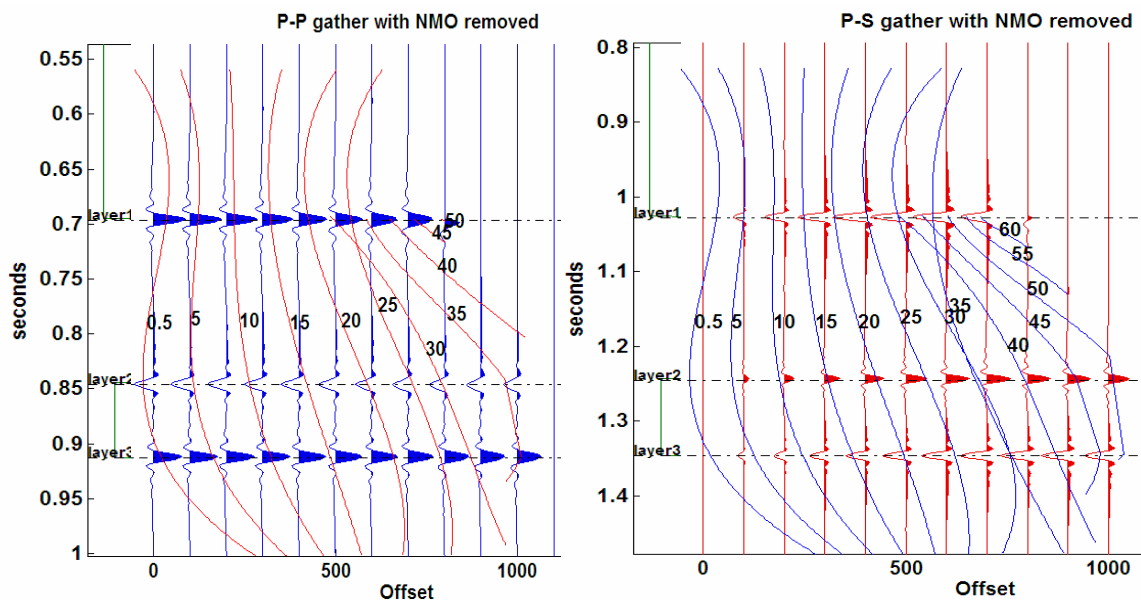
Figure 3.8: The synthetic PP (left) and PS (right) gather from the velocity model in Figure 3.2. Both synthetics have an offset range of 0-1000. The contours of incident angles (degrees) of PP and PS rays are displayed.

The right side of Figure 3.9 shows that for the depth of 1100-1400 m, the joint inversion is more stable (with less condition number) with the inclusion of a longer offset, and the incident angles for these reflectors are less than the critical angle; for example, the critical angle is 45 degrees for the depth of 1200 m. Although including larger angle coverage will lead to a good inversion in the sense of increasing the fold of data, even a smaller offset range gave good results (Figure 3.7). Figure 3.10 shows the *I* and *J* estimate from the joint inversion using the SVD method for synthetic 1, with 0-500

m offset datasets as well as 0-1000 offset datasets, with very similar results for the two

offset data.
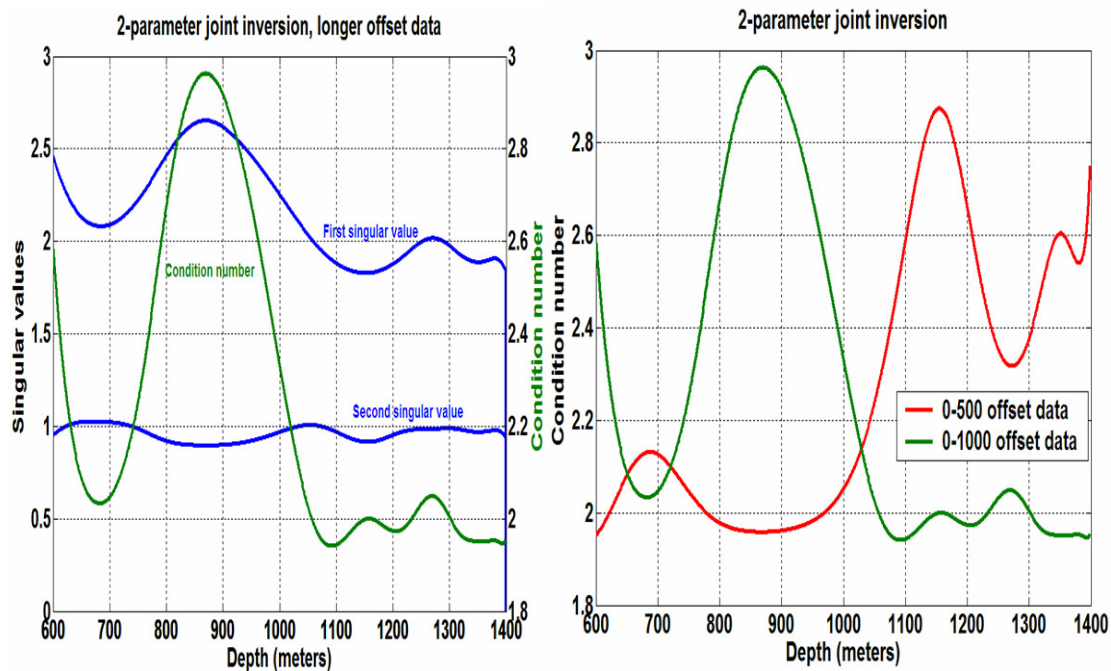
Figure 3.9: Singular values (in blue) and the condition number (red curve) versus depth, from 2-parameter joint inversion of synthetic 1 data with longer offset range. The right figure compares the condition number plots from the 2-parameter joint inversions of the 0-500 offset data and the 0-1000 offset data.
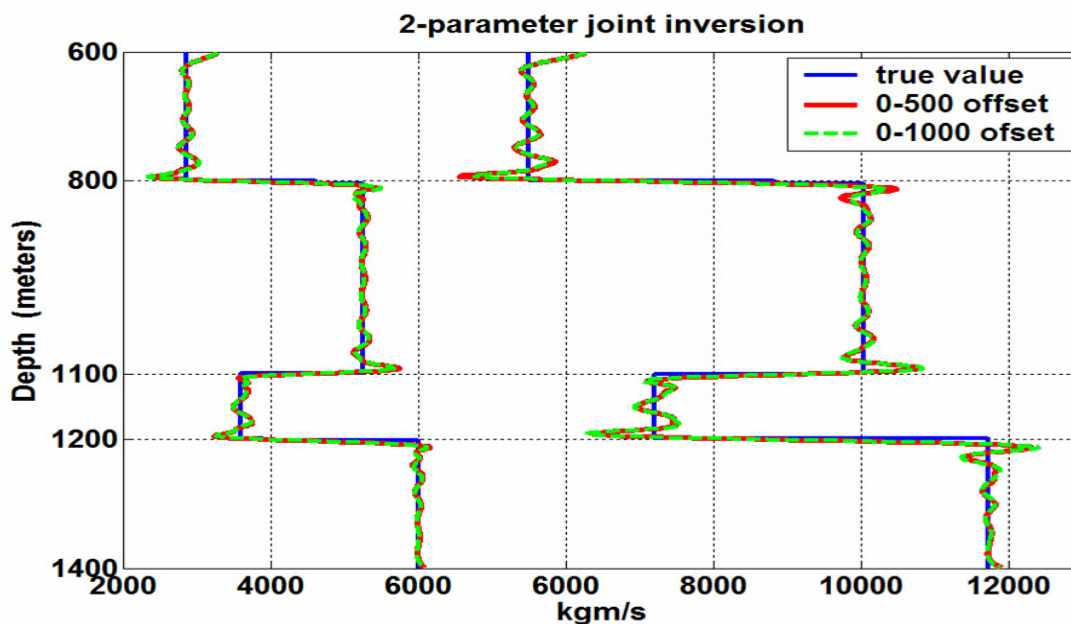
Figure 3.10: P-impedance, I and S-impedance, J estimate from the joint inversion by the SVD method, for synthetic 1 with 0-500 and 0-1000 offset datasets.

3.3.2 Synthetic 2; Blackfoot Field

The inversion results for the real velocity model, Figure 3.11, are examined. The example comes from the Blackfoot 08-08-23-23W4 well, owned and operated by EnCana, in south eastern Alberta, Canada. The PP and PS synthetic were generated with different initial input wavelets. A zero-phase wavelet 5-10-80-100 is used for the PP synthetic, and a zero-phase wavelet 3-7-57-70 is used for the PS synthetic. Both the PP and PS synthetics have the same offset range of 0 to 1000 m. The PP and PS synthetic are shown in Figure 3.12. Figure 3.13 and Figure 3.14 show the singular value and condition number plots for the 2-parameter joint inversion, and the PP-PS inversion of the synthetic datasets. As in the case of the synthetic 1, the PP inversion gives more stable results, with smaller condition numbers than the PS inversion, Figure 3.14, and the

joint inversion has the best stable results with condition numbers around 2, Figure

3.13. The 2-parameter PP and PS inversion and the joint inversion results are presented in

the following sections.
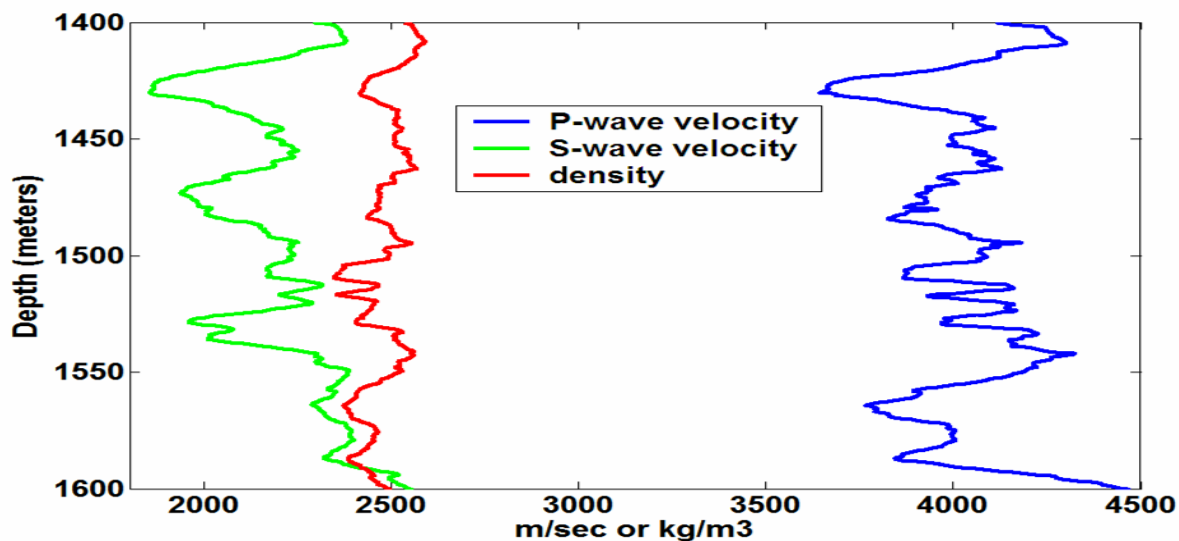
Figure 3.11: Synthetic 2, real velocity model in depth, Blackfoot field.
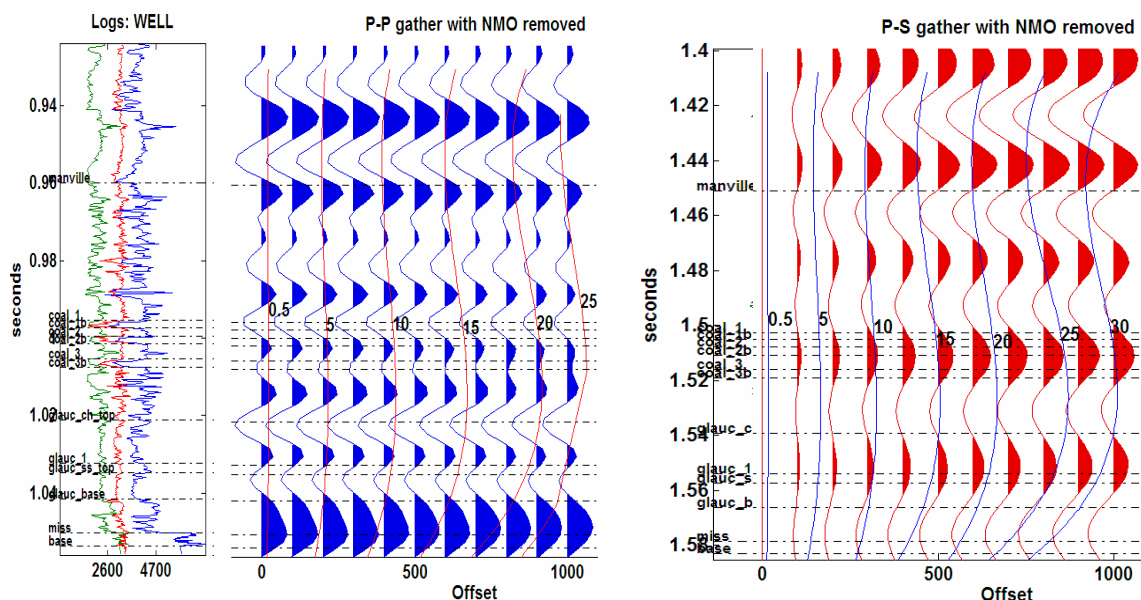
Figure 3.12: Synthetic PP (left) and PS (right) gather from the velocity model in Figure 3.12. Both synthetics have an offset of range 0-1000. The contours of incident angles (degrees) of PP and PS rays are displayed.
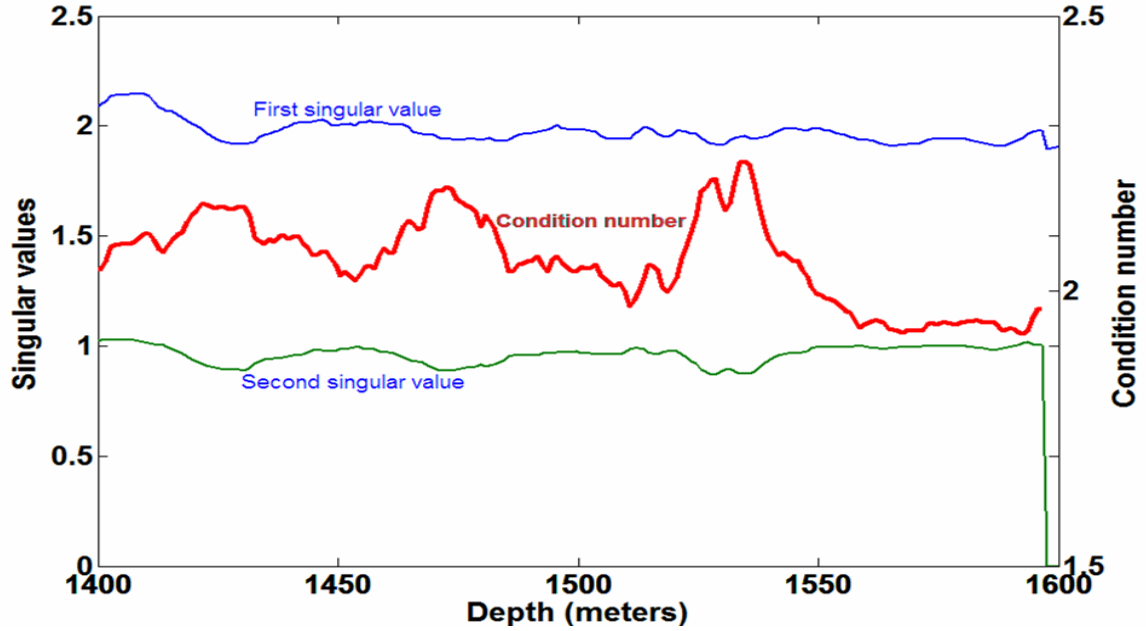
Figure 3.13: Singular values (in blue) and the condition number (red curve) versus depth from the 2-parameter joint inversion of synthetic 2 data.
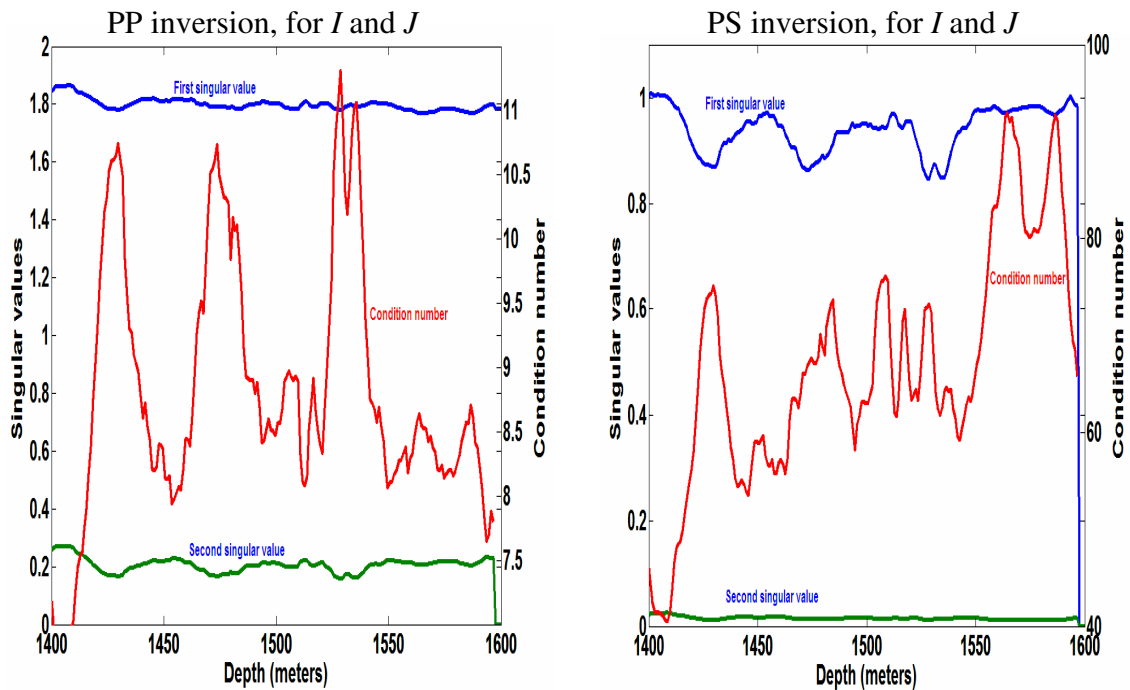
Figure 3.14: Singular values (in blue) and the condition number (red curve) versus depth from the PP (left plot) and PS inversion (right plot) of synthetic 2, for *I* and *J*.

3.3.3 Synthetic 3; Red-Deer Field

Figure 3.15 shows the third studied velocity-depth model, a blocky well log from Red Deer, Alberta, Canada. The AVO inversion of the real Red Deer VSP data is presented in Chapter 5. Both the PP and PS gathers were generated with equal frequency content, the zero-phase wavelet 8-10-120-150 (similar to the real VSP data of Chapter 5), and the offset range from 0 to 250 m (Figure 3.16). The critical angles of the depth of 200 and 300 m are 58 and 50 degrees, respectively and the low velocity layer between 280–299 m has no critical angle (Figure 3.16).
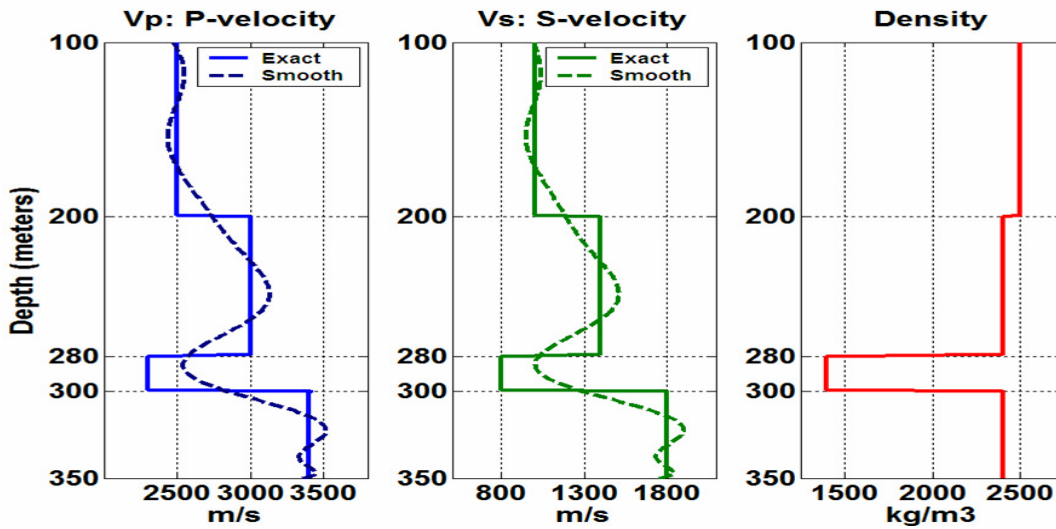
Figure 3.15: Synthetic 3, blocked well logs from Red Deer in depth.
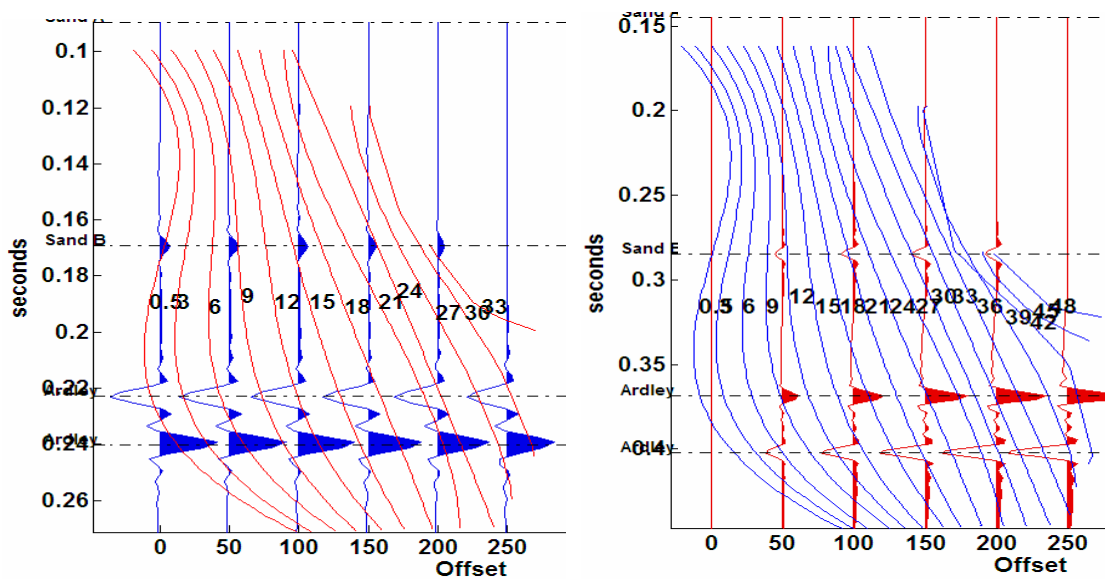
Figure 3.16: The synthetic PP (left) and PS (right) gather from the velocity model in Figure 3.16.

For a depth of 280-300 m (a low velocity layer), all three inversions have a higher condition number (Figure 3.17 and Figure 3.18) expressing the uniqueness of the AVO inversion at the low velocity layer. Figure 3.19 shows the good I and J estimates from the 2-parameter AVO inversion of the synthetic 3 case.
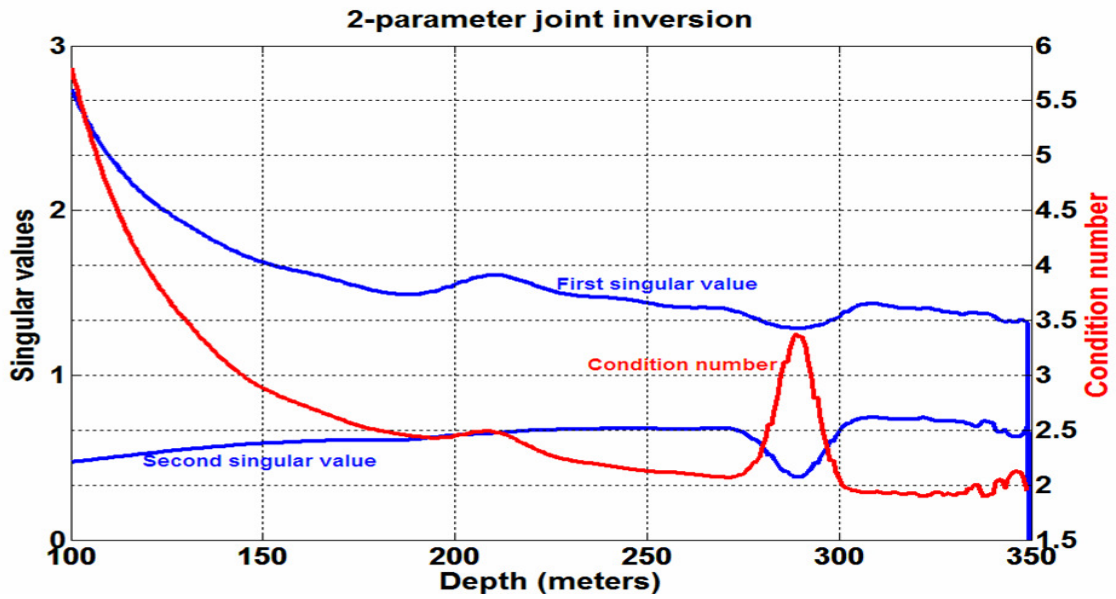
Figure 3.17: Singular values (in blue) and the condition number (red curve) versus depth from the 2-parameter joint inversion of synthetic 3, for *I* and *J*.
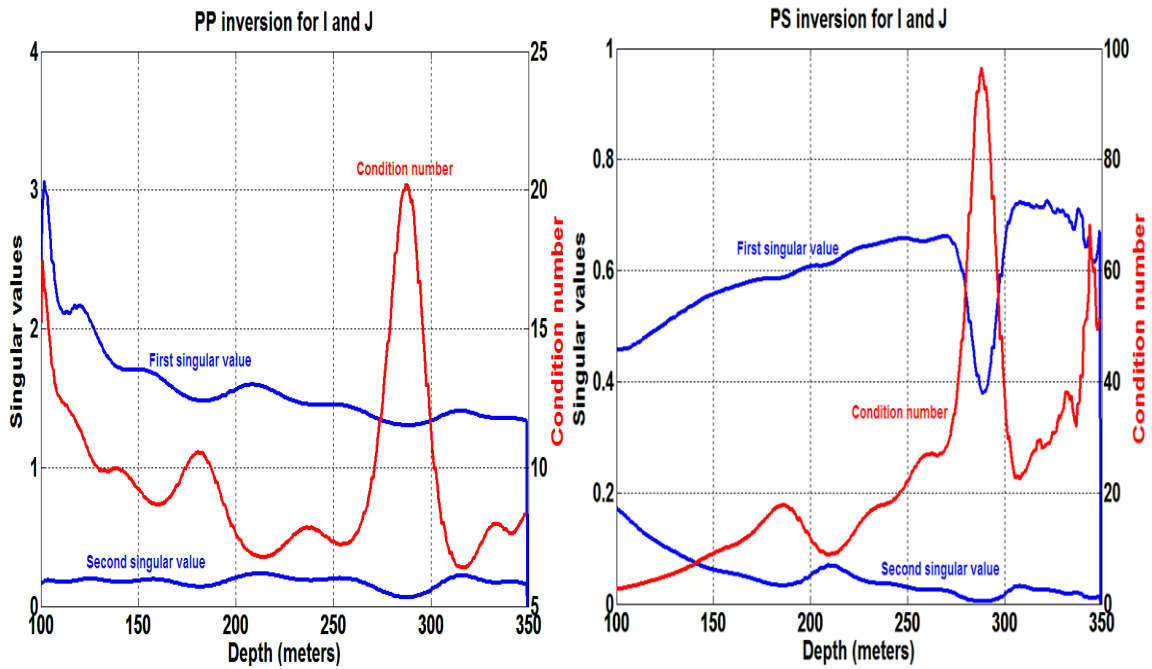
Figure 3.18: Singular values (in blue) and the condition number (red curve) versus depth, from the 2-parameter PP inversion (left plot); and PS inversion, (right plot) of synthetic 3, for *I* and *J*.
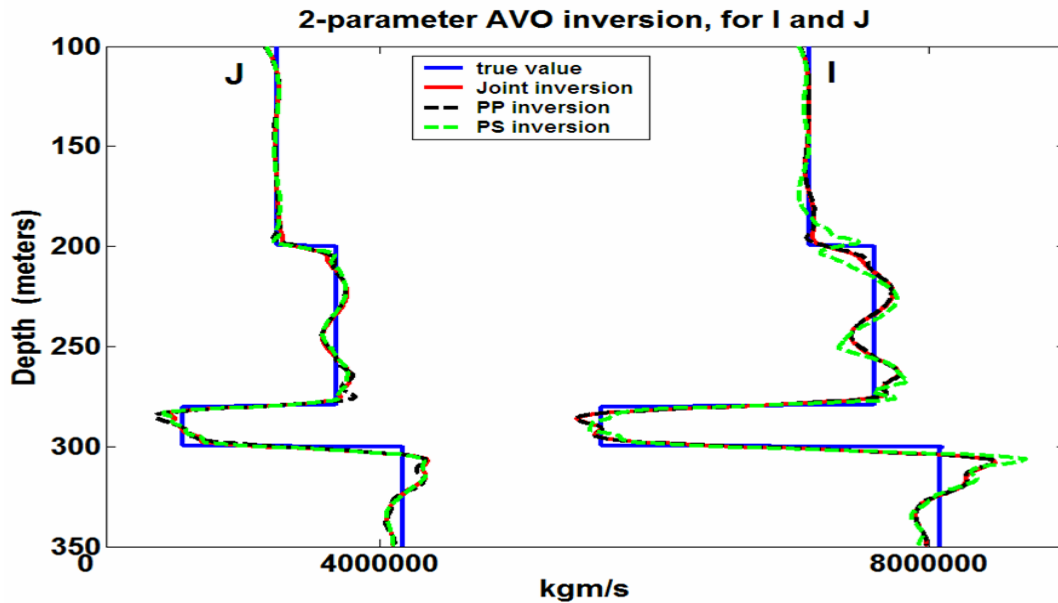
Figure 3.19: P-impedance, *I* and S-impedance, and *J* estimate from the 2-parameter PP, PS and the joint inversion, for synthetic 3.

3.3.4 SVD: The Best Least-Squares Solution

As discussed in section 2.4, for non-singular matrices the SVD solution is identical to the least-squares solution. To demonstrate this for the well-posed synthetic 1, the estimates of *I* and *J* are shown from the SVD and the least-squares methods in Figure 3.20 and Figure 3.21. The *I* estimate is exactly the same for the PP inversion with the least-squares and SVD methods, and similar for the joint inversion, while there is a little difference for the PS inversion (Figure 3.20). The *J* estimate seems to have the same value using the least-squares or SVD method in the PP and PS inversion and the joint inversion (Figure 3.21). An ill-posed PS inversion, Figure 3.6, affects the *I* estimate, while PS inversion still provides a good estimate for *J*.
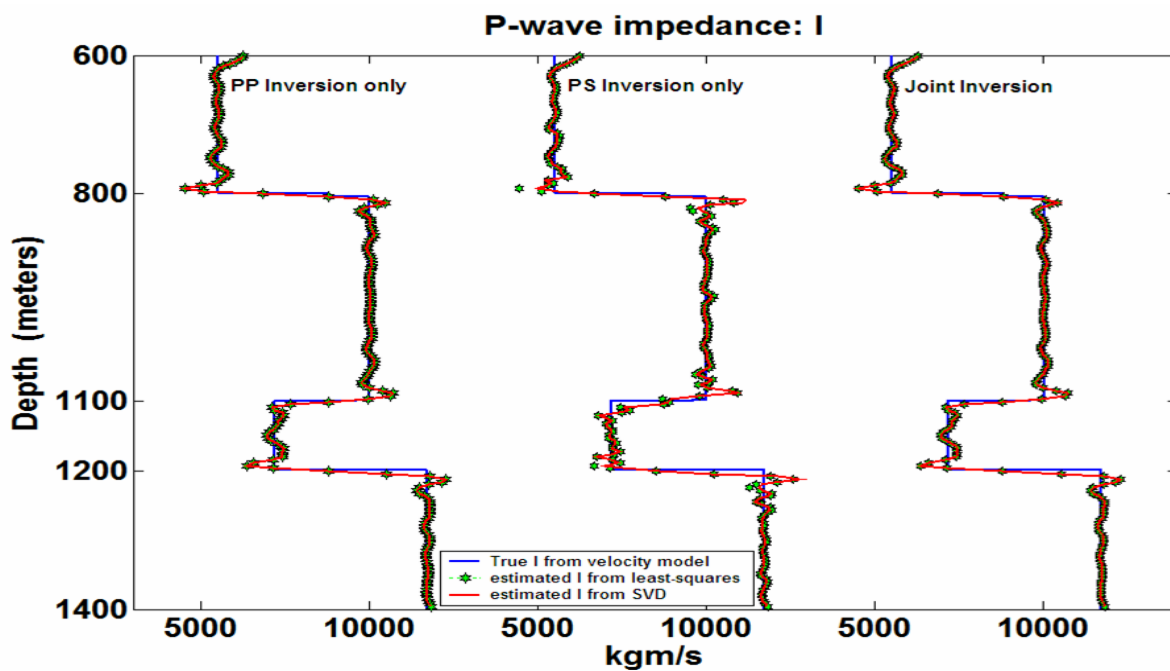
Figure 3.20: P-impedance: *I* estimate by the PP, PS and joint inversion by least-squares and SVD methods for synthetic 1.
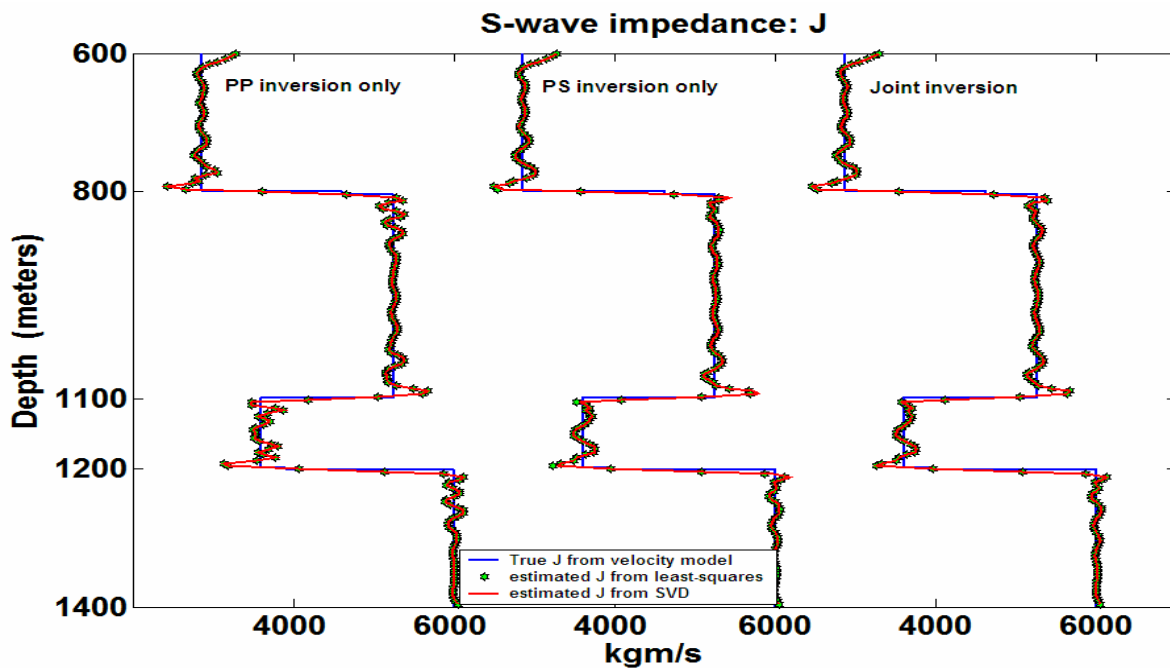
Figure 3.21: S-impedance: *J* estimate by the PP and PS inversion and joint inversion by least-squares and SVD methods for synthetic 1.

3.3.5 Contribution of the PP and PS Data in the Joint Inversion

The stacking weights required in $\Delta I/I$ and $\Delta J/J$ estimates, from the PP, PS and the joint inversion, of the synthetic 1 datasets are shown in Figure 3.22 and Figure 3.23, respectively. Also, the weights for the $\Delta I/I$ and $\Delta J/J$ estimates of the synthetic 2 datasets are shown in Figure 3.24 - Figure 3.25.

The PP data weights from the PP, PS and the joint inversion are very different to the weights of PS data. The PP weights have the maximum magnitude for the zero and near offset traces (Figure 3.22 -Figure 3.25), showing that the zero and near offset traces with highest amplitude have the highest contribution to the estimates. While, the PS weights have zero or minimum magnitude for the zero and near offset traces (Figure 3.22 -Figure 3.25) indicating that the zero or small amplitude of zero and near offset traces have the lowest contributions to the estimates.
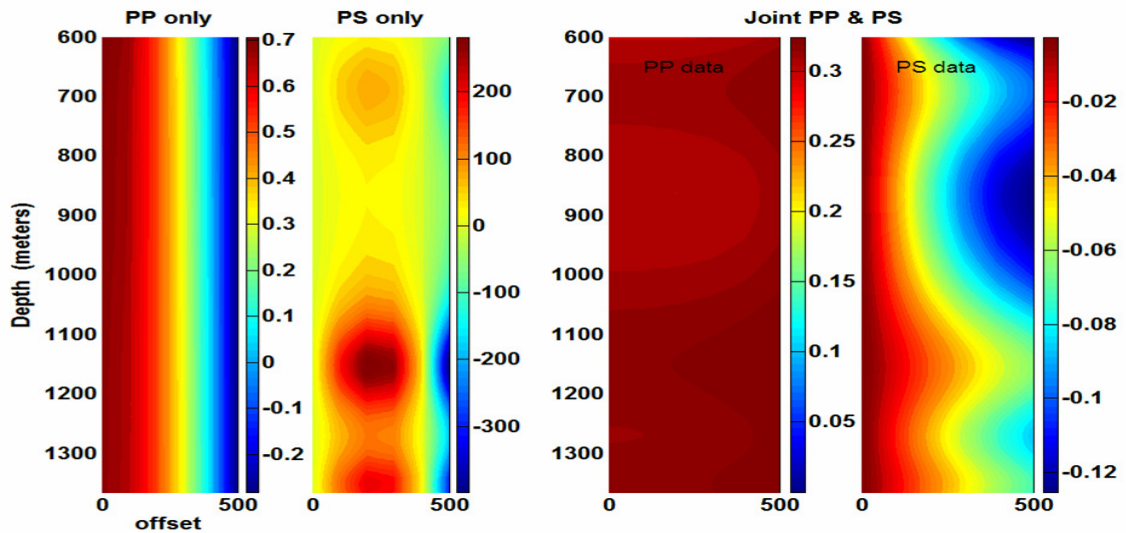
Figure 3.22: The stacking weights in estimating $\Delta I/I$ by PP inversion (left), PS inversion (middle) and joint inversion (right), for synthetic 1. The joint method needs two sets of weights, for PP and PS data respectively. Note the colour bars on the right of each plot.
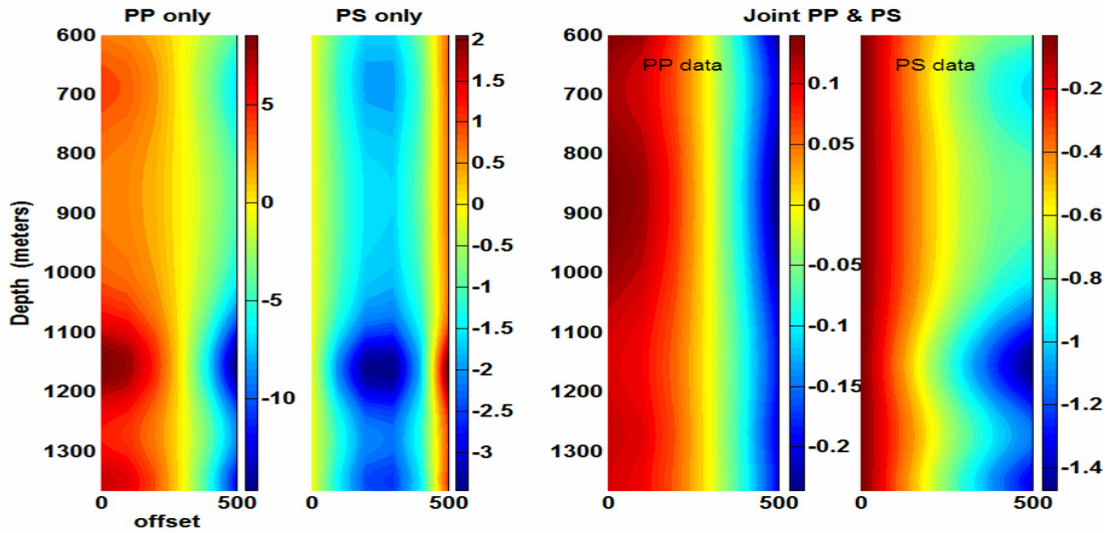
Figure 3.23: The stacking weights in estimating $\Delta J/J$ by PP inversion (left), PS inversion (middle) and joint inversion (right), for synthetic 1. The joint method needs two sets of weights, for PP and PS data respectively. Note the colour bars on the right of each plot.

Examining the weights for the joint inversion in the estimation of $\Delta I/I$, the PP weights are larger than to the weights applied to the PS data, is shown in Figure 3.24 for synthetics 2 and Figure 3.22 and for synthetics 1 (look at reflector depths at 1100 and 1200 m). Thus, in joint inversion, PP data contribute more to the I estimate than do PS data. For the $\Delta J/J$ estimate in joint inversion, the PS weights are larger than the PP weights, Figure 3.23 and Figure 3.25, thus PS data contribute more to the J estimates in the joint inversion.
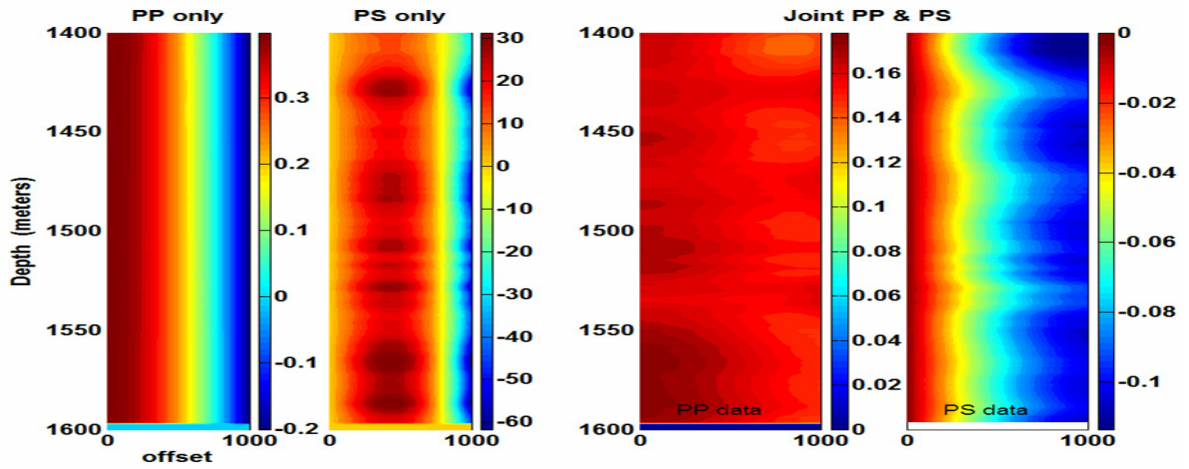
Figure 3.24: The stacking weights in estimating *ΔI/I* by PP inversion (left), PS inversion (middle) and joint the inversion (right), for synthetic 2. The joint method needs two sets of weights, for PP and PS data. Note the colour bars on the right of each plot.
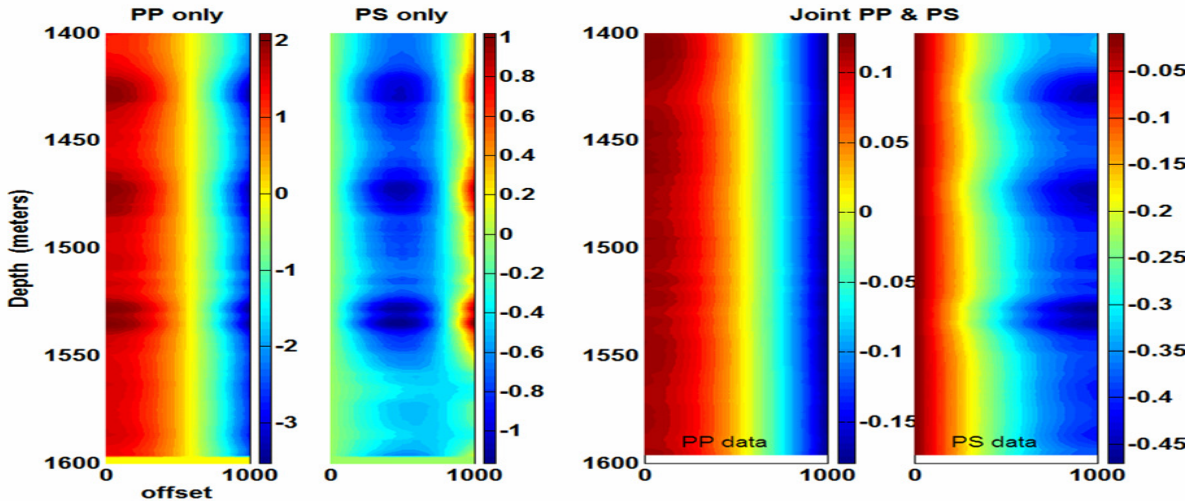
Figure 3.25: The stacking weights in estimating *ΔJ/J* by PP inversion (left), PS inversion (middle) and the joint inversion (right), for synthetic 2. The joint method needs two sets of weights, for PP and PS data. Note the colour bars on the right of each plot.

Figure 3.26 shows the *I* and *J* estimates from the PP inversion and the joint inversion, and Figure 3.27 shows the *I* and *J* estimates from the PS inversion and the joint

inversion of synthetic 2. The *I* estimate is very similar to the PP inversion and joint inversion (Figure 3.26), confirming the higher contribution of the PP data in the joint inversion. The *J* estimate from the joint inversion is very similar to the PS inversion result (Figure 3.27), confirming the higher contribution of the PS data in the joint inversion. Additionally, the *J* estimate from the joint inversion shows less frequency content compared to the result of the PP inversion (Figure 3.26), because the PS data, with its reduced frequency content, has more influence on the *J* estimate. This observation could help in deciding the correct polarity of the PP and PS data used in a joint AVO inversion.
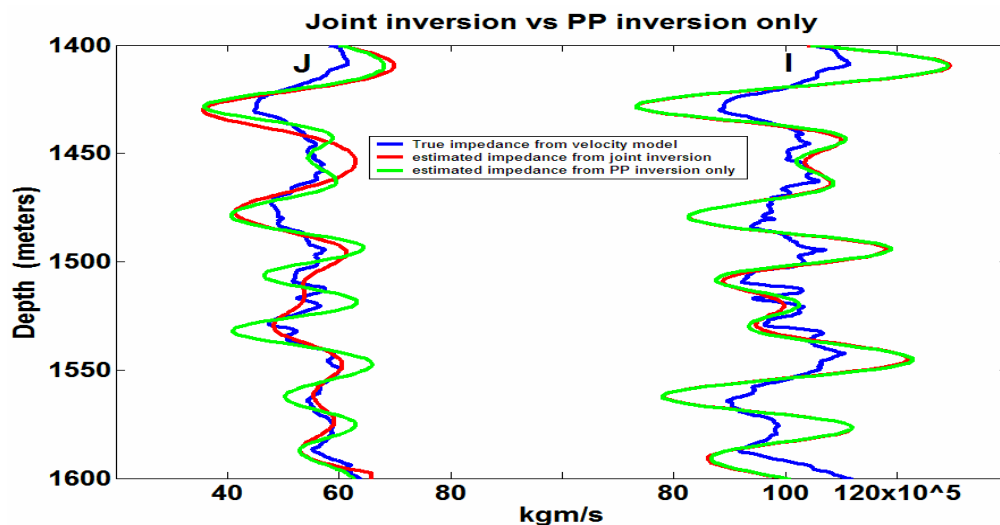
Figure 3.26: P-impedance, *I*, and S-impedance, *J*, from the joint and PP inversion of synthetic 2.
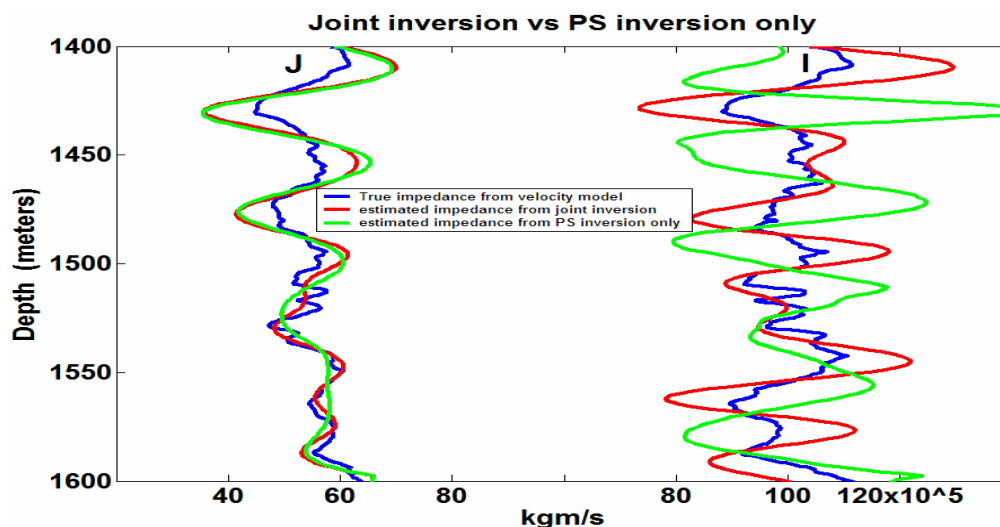
Figure 3.27: P-impedance, *I* and S-impedance, *J* from the joint and PS inversion of synthetic 2.

3.3.6 PP and PS Polarity Check

The SEG polarity standard is a positive amplitude (peak) on a PP section indicating a P-impedance increase, whereas a positive amplitude on a PS section indicates an increase in the S-impedance (Thigpen et al. 1975). Since the SEG acquisition polarity standard was elaborated in terms of single-component surface seismic conventions, it did not explicitly make provision for the horizontal-component geophones (Brown et al., 2002). Also, the polarity of the input data to an AVO inversion needs to follow Zoeppritz equations and not the SEG standard. Therefore, the issue of polarity is deceivingly simple, and prior to the joint AVO inversion we need to make sure that the correct polarity of the PP and PS data is considered.

The previous discussion, using the results of the PP and PS inversion, has shown that a good *I* estimate is expected from the PP inversion, and a good *J* estimate is

expected from the PS inversion, which can lead to a decision regarding the correct polarity of the PP and PS data. A simple rule for checking the correct PP and PS polarity is as follows:

1: Prepare the PP inversion and look for the *I* estimate.

2: Compare the *I* estimate to the estimate from the well control. Change the PP polarity if it looks flipped.

3: Prepare the PS inversion and look for the *J* estimate.

4: Compare the *J* estimate to the estimate from the well control. Change the PS polarity if it looks flipped.

This polarity check is recommended in the joint inversion, due to the fact that with a flipped polarity for one of the datasets, the joint inversion still shows a good result for the estimate that the correct polarity data is dominant for.

3.3.7 Low Frequency Inclusion Improvement

Figure 3.28 and Figure 3.29 show the joint inversion results with the SVD method of synthetic 1 and 2. The impedances are displayed before and after including the low-frequency components; the impedance estimates have significantly improved after including the low-frequency.
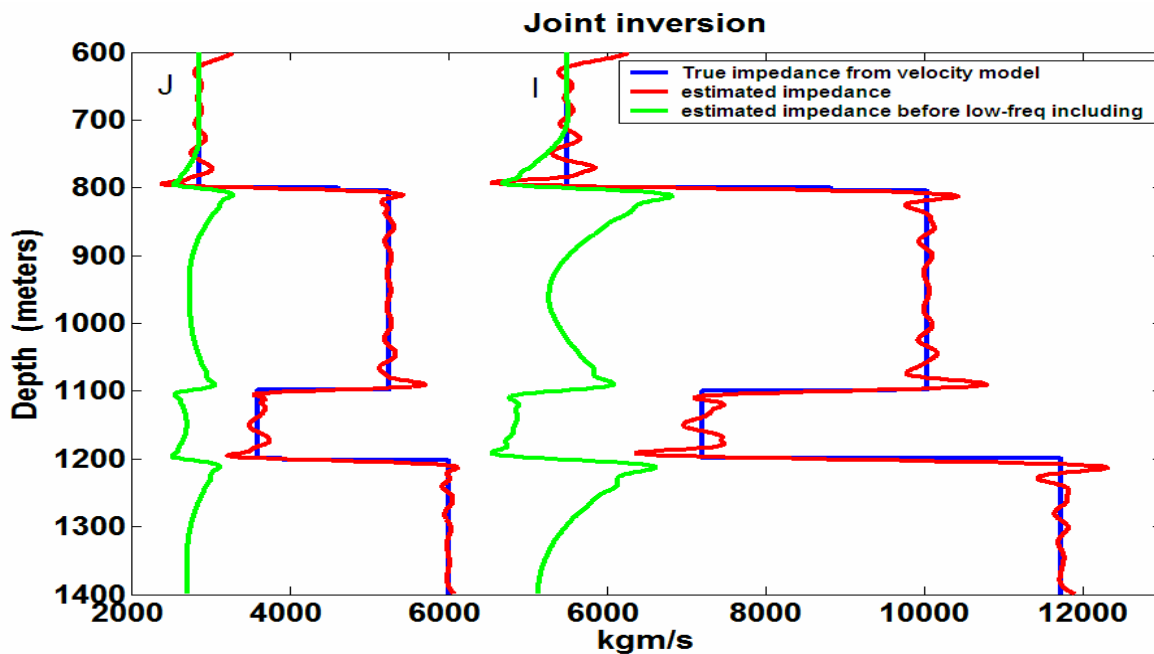
Figure 3.28: P-impedance, *I*, and S-impedance, *J*, from joint inversion of synthetic 1.
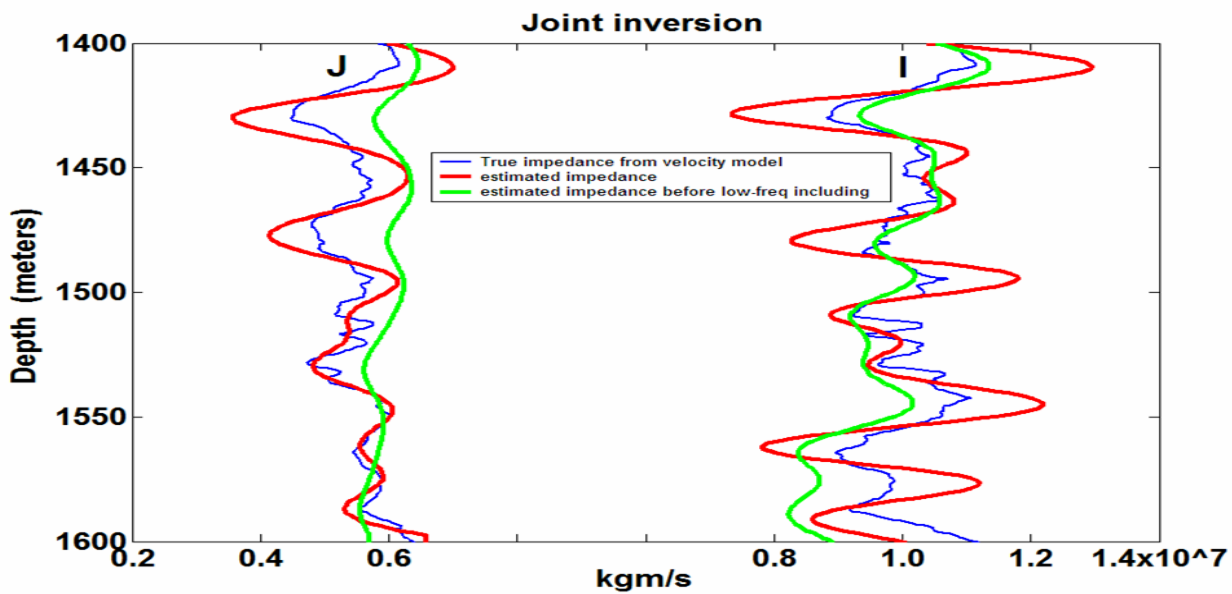
Figure 3.29: P-impedance, *I*, and S-impedance, *J*, from joint inversion of synthetic 2.

3.3.8 Noise Effect on 2-Parameter Inversion

Any given seismic recording will contain some amount of noise in relation to the desired signal. Since the joint inversion method includes twice as many reflectivity observations as the others, it is reasonable to assume that a corresponding improvement in signal-to-noise ratio is possible (Larsen and Margrave, 1999). To examine the effect of noise upon the inversion accuracy, a random noise is added to the synthetic data. The MATLAB routine called RNOISE (CREWES MATLAB library) is used to generate the random noise. RNOISE adds the random noise to a seismic trace in the time domain with the desired signal-to-noise ratio. RNOISE measures the root-mean-squares of power of a seismic trace and sets the standard deviation of the noise as

$$\sqrt{\sum_t (\text{noise(t)})^2} = \frac{\sqrt{\sum_t (\text{Seismic trace(t)})^2}}{\text{S/N}}. \tag{3.10}$$
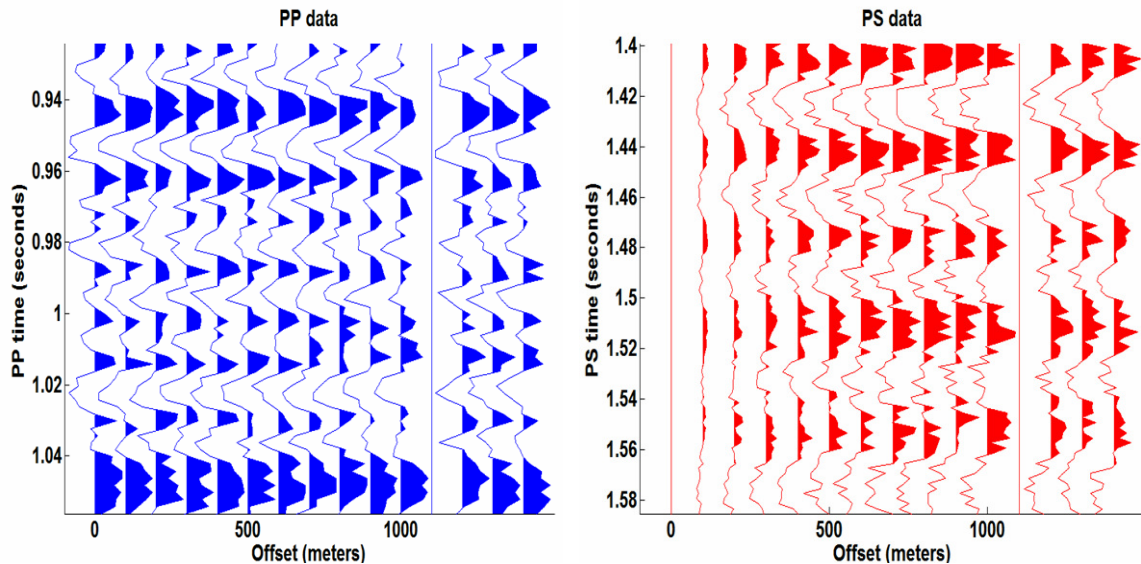
Figure 3.30: PP and PS data of synthetic 2, with a signal-to-noise ratio of 2. In each seismogram, the three traces on the right are three repetitions of the stacked trace.

Figure 3.30 shows the PP and PS data of the synthetic 2 with a signal-to-noise ratio of 2. In this example, the noise is larger than is typically encountered in real surface seismic data. The *I* and *J* estimate from the 2-parameter PP, PS and the joint inversion of the noisy data is shown in Figure 3.31-Figure 3.33. In the presence of noise, the PP inversion is poor for the *J* estimate (Figure 3.31), the PS inversion is poor for the *I* estimate (Figure 3.32), and the joint inversion is significantly more stable for both estimates for the noisy datasets (Figure 3.33). In fact, the joint inversion is unaffected in this case.
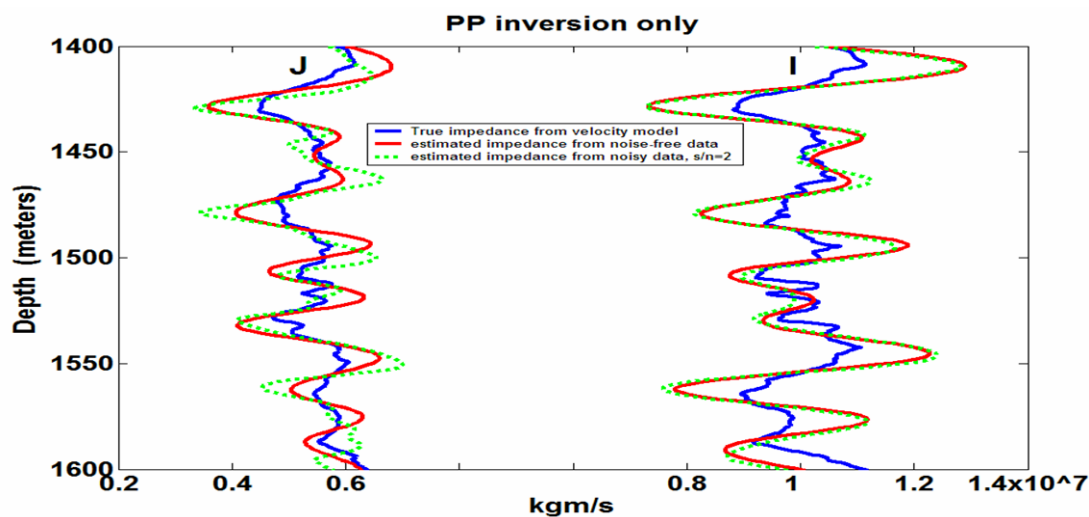
Figure 3.31: P-impedance, *I*, and S-impedance, *J*, from the PP inversion of the noisy data of synthetic 2 with a signal-to-noise ratio of 2.
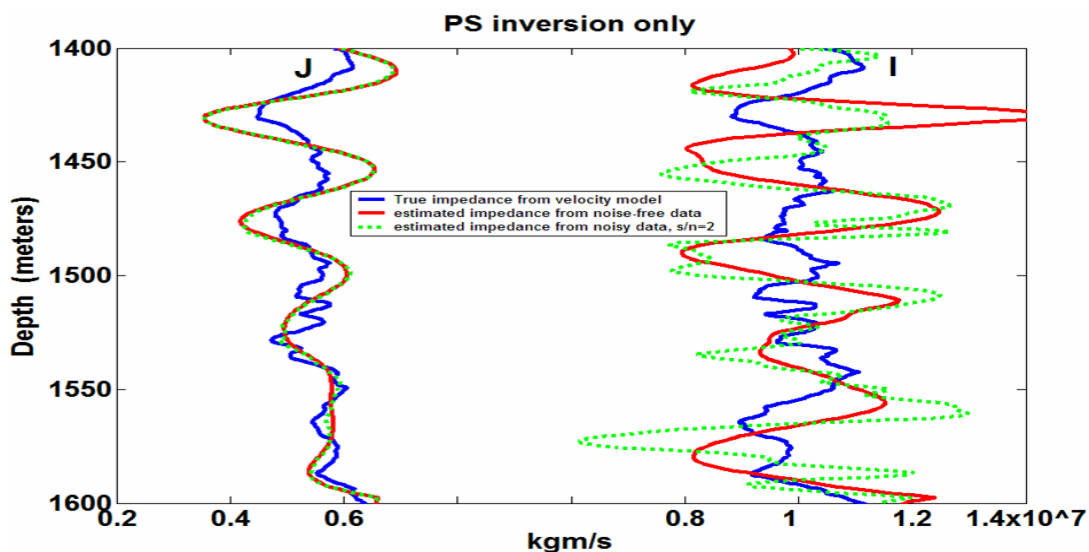
Figure 3.32: P-impedance, *I*, and S-impedance, *J*, from the PS inversion of the noisy data of synthetic 2 with a signal-to-noise ratio of 2.
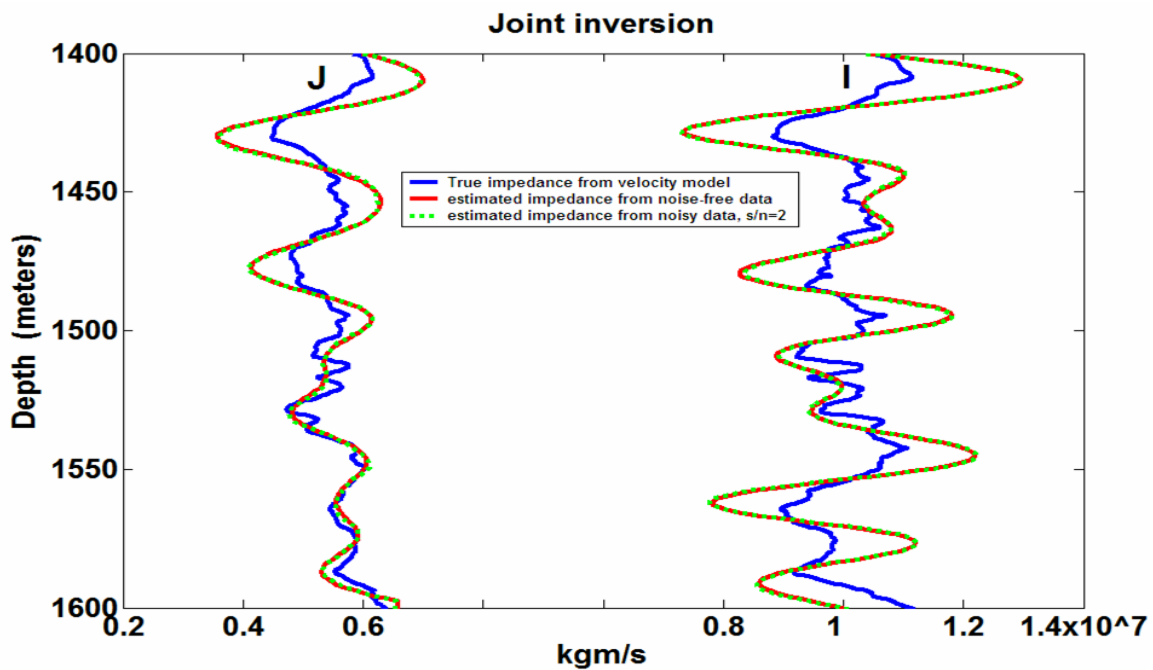
Figure 3.33: P-impedance, *I*, and S-impedance, *J*, from the joint inversion of the noisy data of synthetic 2 with a signal-to-noise ratio of 2.

3.4 Three-Parameter Joint Inversion Testing

The solution vector calculated by the 2-parameter joint inversion consisted of the I and J estimate, while the density term is calculated by using Gardner's rule. Theoretically it seems that the extending of the 2-parameter joint inversion to a 3-parameter joint inversion, for modeling the same PP and PS data, have a more stable and accurate inversion by avoiding another approximation for the density term. The 3-parameter joint inversion results are also presented for the synthetic examples of Section 3.3.

3.4.1 Synthetic 1

The 2-parameter AVO inversion was successfully applied to the synthetic 1 example. The assumption of Gardner's rule for the density term resulted in a well-posed 2-parameter joint inversion with good estimates for the two parameters I and J. The 3-parameter AVO inversion for synthetic 1 example is presented.

Figure 3.34 shows the three singular values of the 3-parameter PP inversion of synthetic 1 versus depth. The higher condition number, condition-number≥ 1000, indicates an instability of the 3-parameter PP inversion in estimating the three parameters, however, with good results for the two parameters I and J. Figure 3.35 shows the I, J and ρ estimates from 2- and 3-parameter PP inversions of synthetic 1, indicating that the density estimate is not as good as the I and J estimates, noting that both the 2- and 3-parameter PP inversion have identical favourable estimates for I and J.
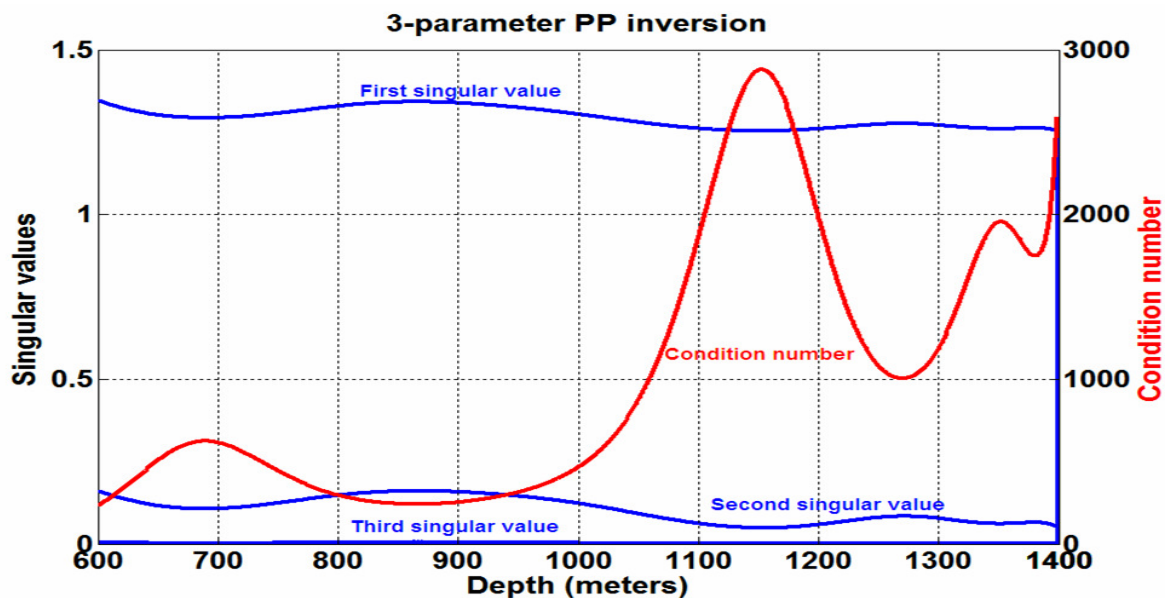
Figure 3.34: Singular values (in blue) and the condition number (red curve) versus depth from the 3-parameter PP inversion of synthetic 1.
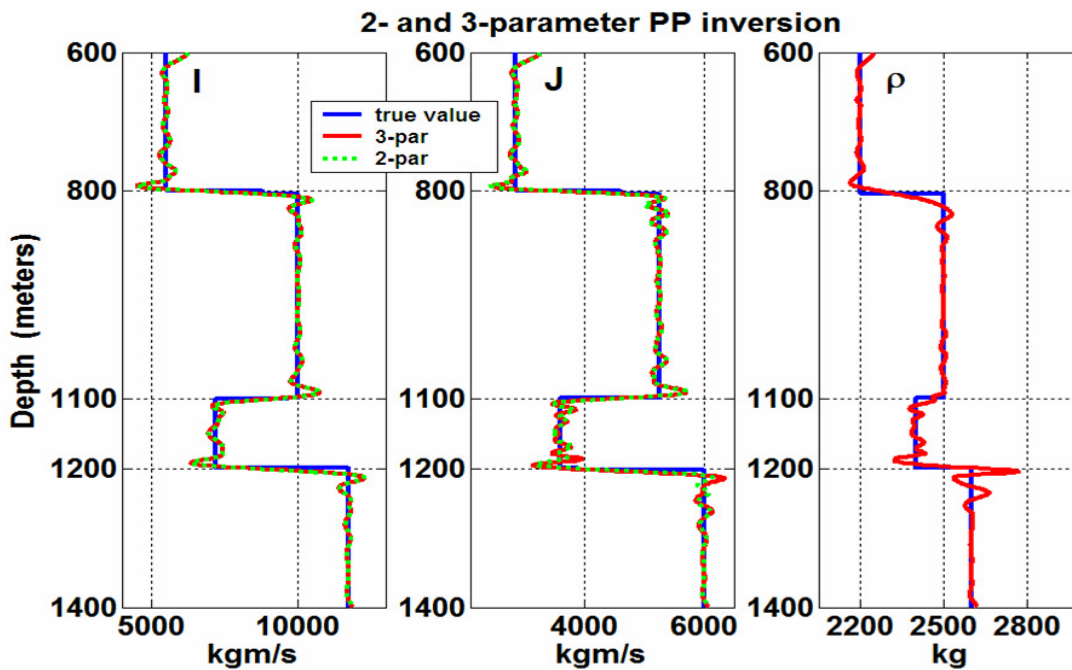
Figure 3.35: P-impedance: I, S-impedance and density estimates from 2- and 3-parameter PP inversions of synthetic 1.

Figure 3.36 shows the two singular values of the PS inversion, for the *J* and *ρ* estimates versus the depth of synthetic 1. The condition number is decreased compared to Figure 3.6, and the PS inversion for *I* and *J* estimates indicates that the converted shear PS data is capable of being inverted with favourable estimates of *J* and *ρ*. Therefore, even for synthetic 1 which obeys Gardner's rule, the choice of parameters is not neutral; the PS inversion has more stable results for the choice of *J* and *ρ* parameters, rather than *J* and *I*. Figure 3.37 shows the *I*, *J* and *ρ* estimates from the PS only inversion of synthetics 1; the red plots are the results of the PS inversion for *J* and *ρ*, and the green plots are the results of the PS inversion for *J* and *I*. Comparing the estimate from Figure 3.7 Figure 3.37, also comparing Figures 3.36 and 3.6 shows better PS inversion results for the choice of *J* and *ρ* parameters.
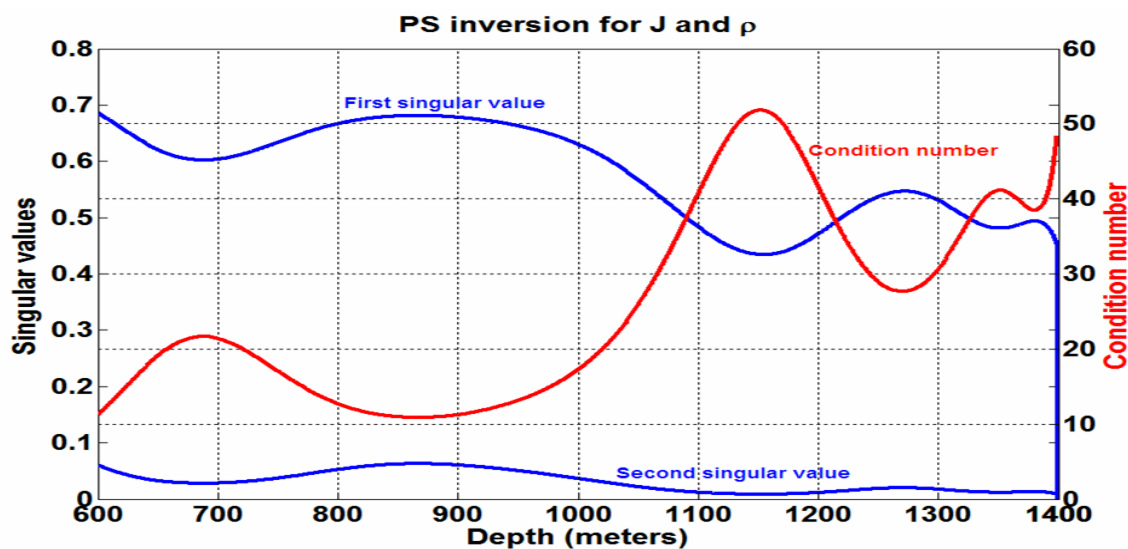
Figure 3.36: Singular values (in blue) and the condition number (red curve) versus depth, from the PS inversion of synthetic 1, for *J* and *ρ* estimates.
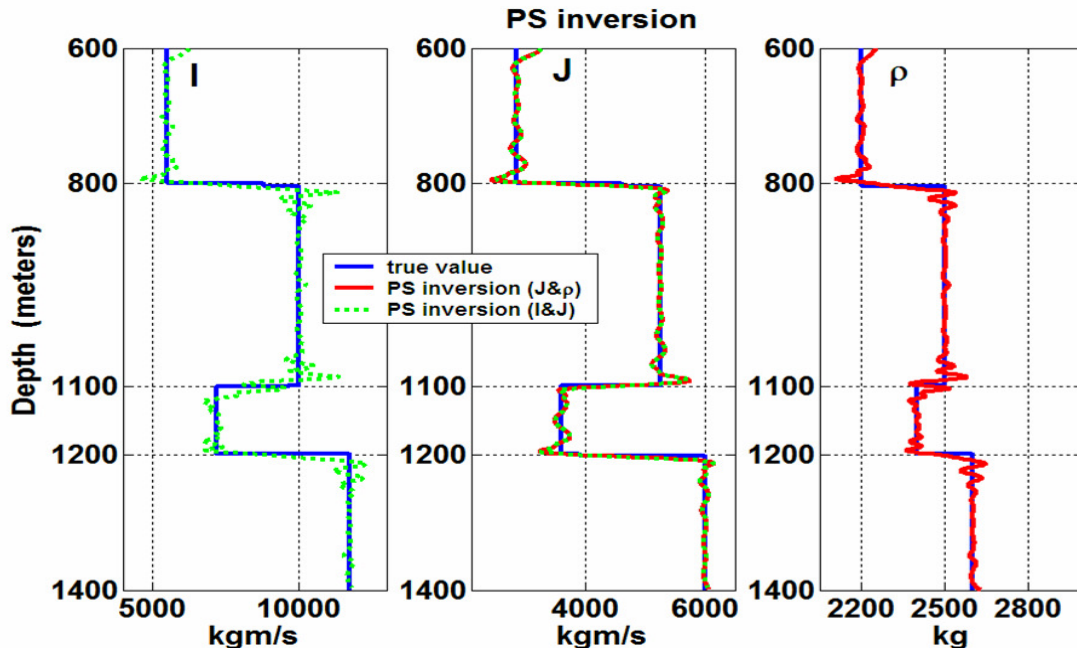
Figure 3.37: P-impedance: I, S-impedance and density estimates from the PS inversion of synthetic 1.

Figure 3.38 shows the three singular values of the 3-parameter joint inversion of synthetic 1 versus depth, the 3-parameter joint inversion has a smaller condition number than the PP inversion show in Figure 3.34; however, it is not as well-posed as the 2-parameter joint inversion (Figure 3.5). Figure 3.39 shows the I, J and ρ estimates from the 2- and 3-parameter joint inversion of the synthetics 1, indicating that both 2- and 3-parameter joint inversion provide good estimates for I and J.
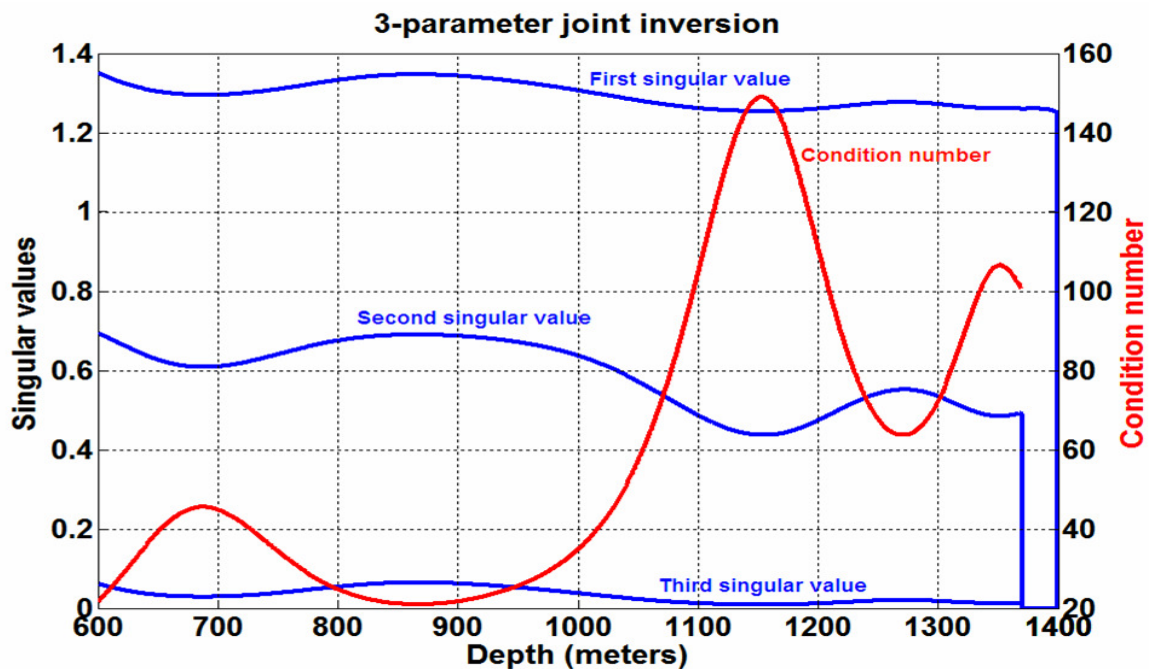
Figure 3.38: Singular values (in blue) and the condition number (red curve) versus depth from the 3-parameter joint inversion of synthetic 1.
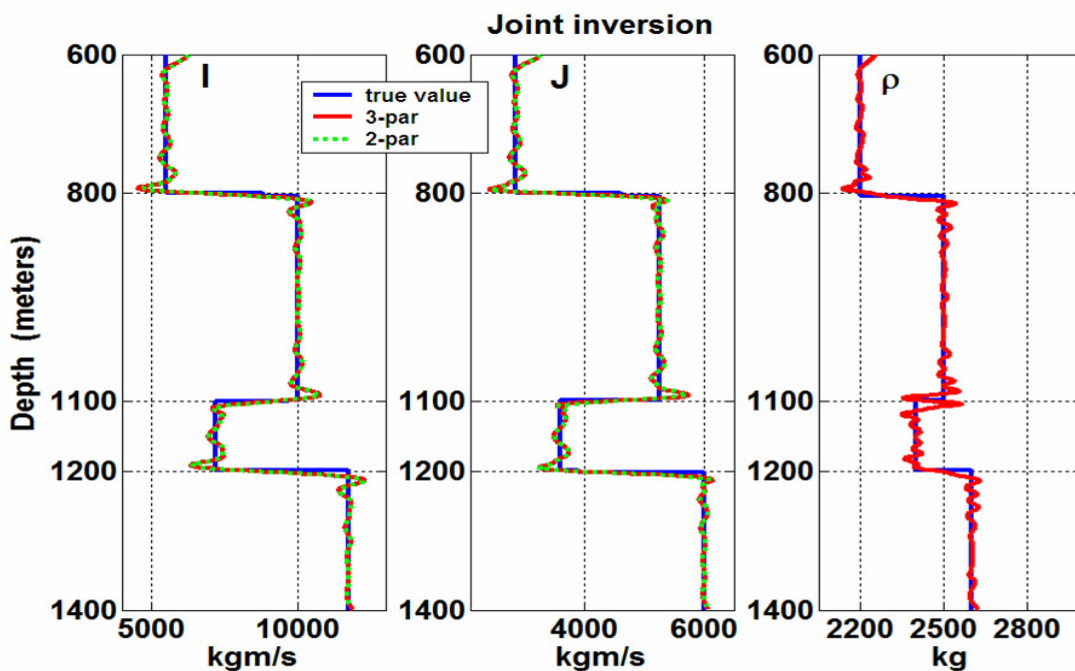
Figure 3.39: P-impedance: *I*, S-impedance *J*, and density estimates from 2- and 3-parameter joint inversions of synthetic 1.

The condition number plots for the 3-parameter PP and joint inversions, Figure 3.34 and Figure 3.38, indicate a smaller condition number for the joint inversion compared to the PP inversion. Therefore, a better J and density estimate is expected from the joint inversion than from the PP inversion. Figure 3.40 shows this, while having an identical estimate for I. The advantage of the joint inversion over the PP inversion is noticeable even for the ideal non-singular synthetic 1 example (Figure 3.40).
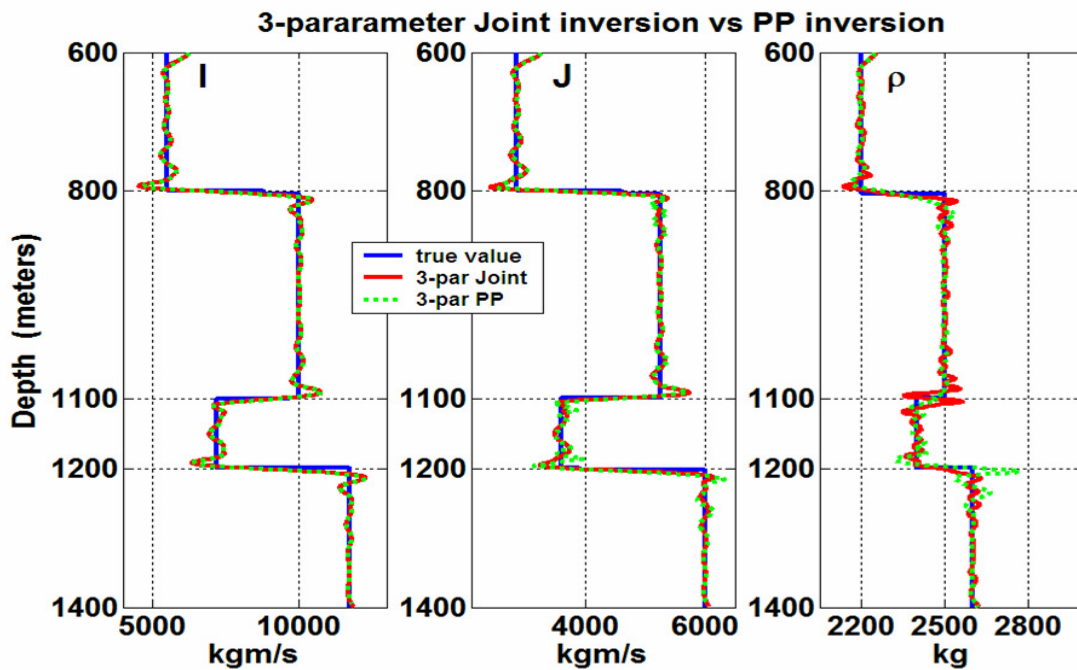
Figure 3.40: P-impedance: I, S-impedance: J, and density: ρ, estimates from the 3-parameter joint and PP inversion of synthetic l.

The J and ρ estimates from the 3-parameter joint inversion, and the PS inversion, are compared in Figure 3.41. Surprisingly, the PS inversion provides a better estimate for density while it is identical for the J estimate. Besides, the lower condition number from

PS inversion (Figure 3.36), compared to the one from the joint inversion (Figure 3.38), further validates the statement. Therefore, the PS inversion results in a good *J* and *ρ* estimate, and confirms the case study by Jin et al. 2002: "*since the amplitude of PS reflection depends on only two parameters for an isotropic elastic medium, the numerical singularity associated with parameter estimation may be less severe than for the P-wave three parameter case*".
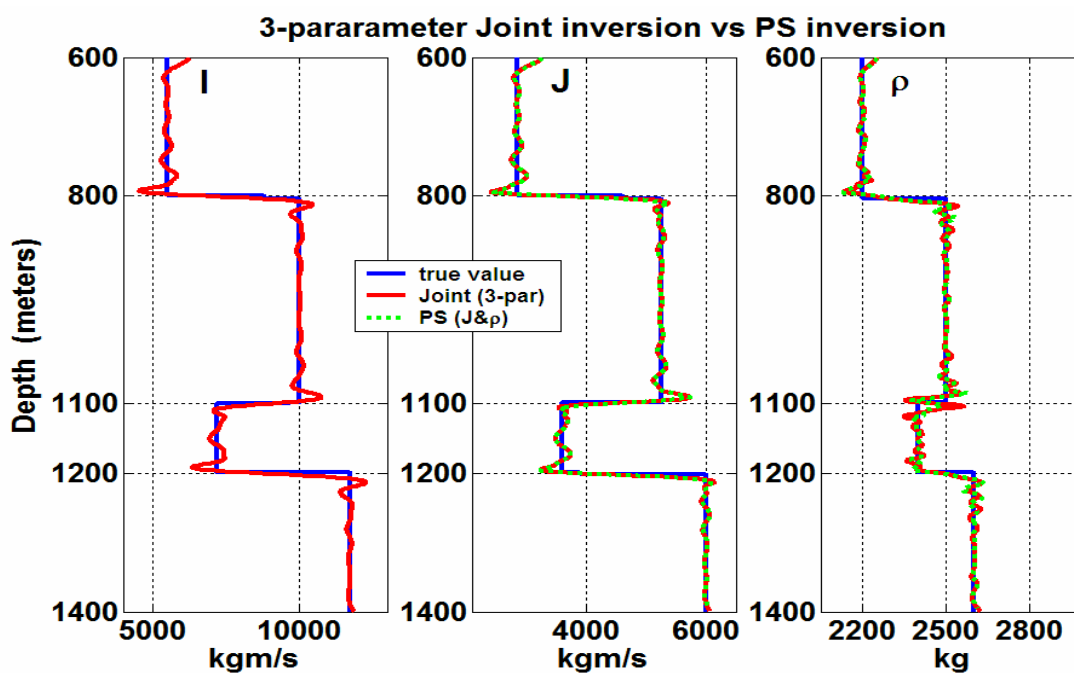
Figure 3.41: P-impedance: *I*, S-impedance: *J*, and density: *ρ*, estimates from the 3-parameter joint and the PS inversion, for *J* and *ρ*, of synthetic 1.

3.4.2 Synthetic 4; Non Gardner's Rule Example

When information about the density is unavailable, density is often estimated from P-wave velocity using an empirical relationship such as Gardner's rule. Gardner's rule is essentially an average of fits for clastics (including sandstone and shale) and carbonates

(Gardner, et al., 1974) rocks. Miller and Stewart (1991) showed that Gardner's rule fits for sandstone quite well except at low densities. Generally Gardner's rule does not hold for all rock types, especially evaporates such as salt. Therefore rather than the direct application of Gardner's rule, the generation of the density from another methods is desired. The 3-parameter inversion claims to estimate the density. The application of 3-parameter AVO inversion on a velocity model which does not obey Gardner's rule is presented.

Figure 3.42 shows the velocity and density model of synthetic 4. The synthetic 4 velocity model is identical to that of synthetic 1, only the density model does not obey Gardner's rule for the depth between 1100-1200 m. The PP and PS data for synthetic 4 both have an initial 5-10-80-100 Hz zero-phase wavelet, and the same offset range from 0 to 500 m.
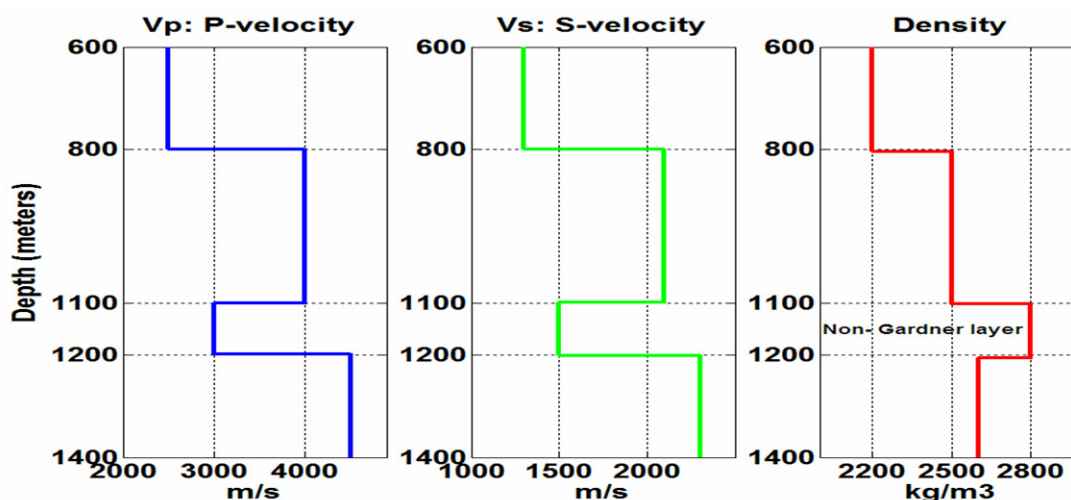
Figure 3.42: Synthetic 4, velocity-depth model with a density model which does not obey the Gardner's rule.

Figure 3.43 shows the condition number plot from the 3-parameter joint inversion for synthetic 4, which has a identical magnitude compared to the 3-parameter joint inversion of synthetics 1 (Figure 3.38); synthetic 1 and 4 have identical velocity model and different density model. Also, there are good estimates for all three parameters from the 3-parameter joint inversion (Figure 3.44). This example confirms that the application of the 3-parameter inversion rather than the 2-parameter inversion for just I and J, for which the density term could not be estimated from the relation between the P-impedance and density (Figure 3.45). In Figure 3.45, the density estimate from the 2-parameter joint inversion is calculated directly from Gardner's rule.
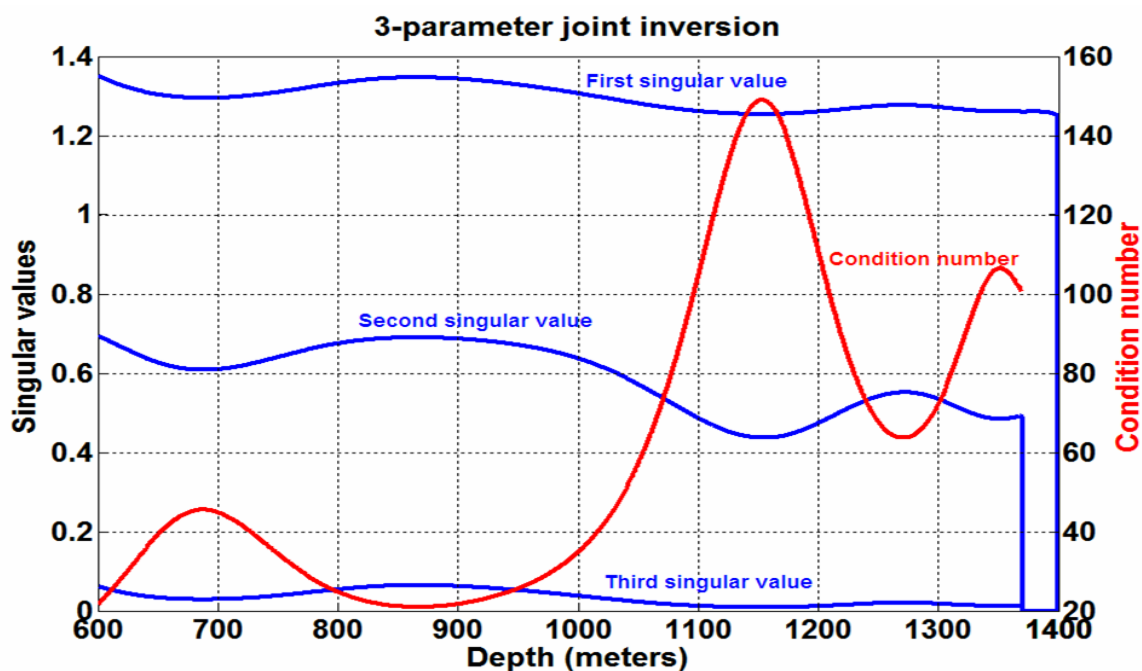
Figure 3.43: Singular values (in blue) and the condition number (red curve) versus depth, from the 3-parameter joint inversion of synthetic 1, with a non-Gardner's rule density-velocity.
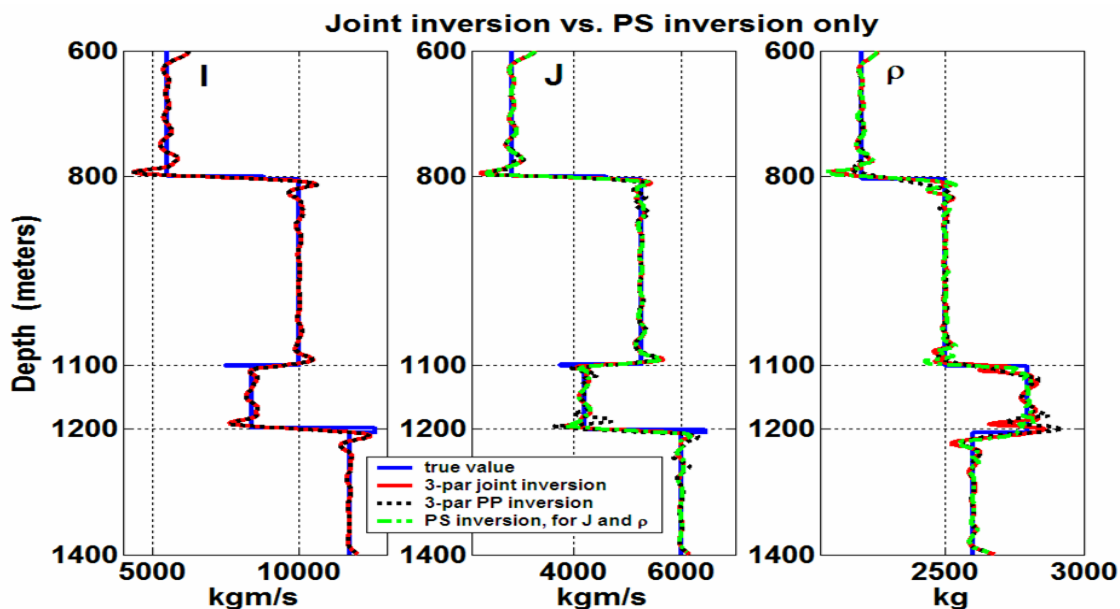
Figure 3.44: P-impedance: *I*, S-impedance: *J*, and density: ρ, estimates from the 3-parameter PP and joint inversions and the PS inversion, for *J* and ρ, of synthetic 4 with a non-Gardner's rule density-velocity.
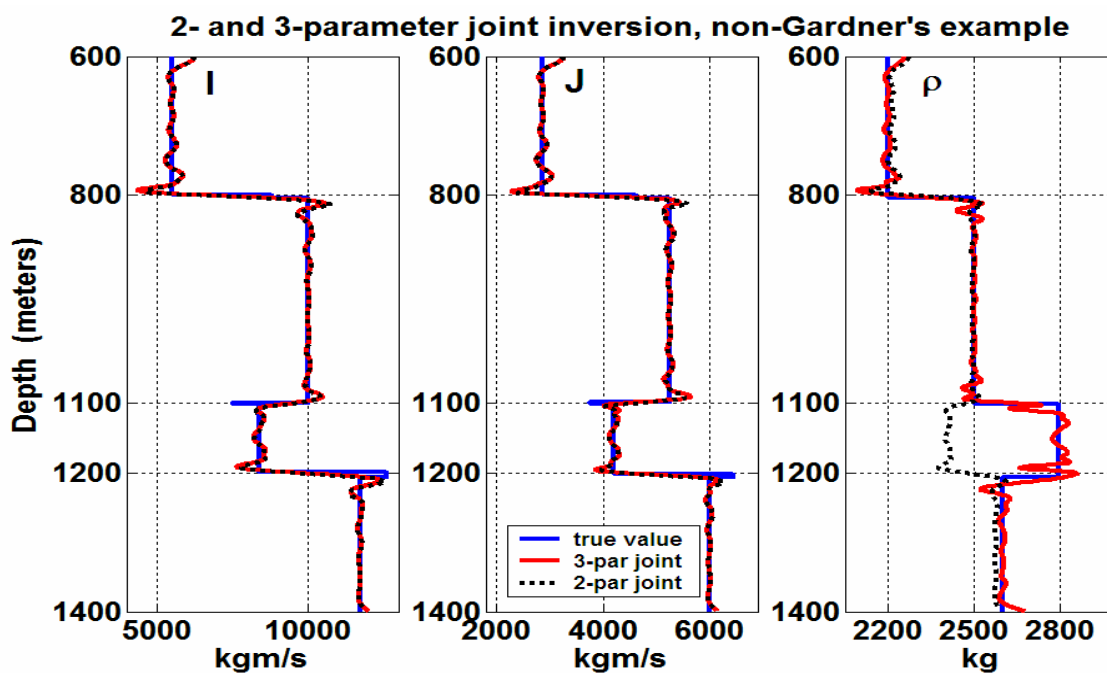
Figure 3.45: P-impedance: *I*, S-impedance: *J*, and density: ρ, estimates from the 2- and 3-parameter joint inversions of synthetic 4 with a non-Gardner's rule density-velocity.

Most of the industry packages for AVO inversion, only estimate the two parameters, *I* and *J*, while the third parameter ρ is calculated by using Gardner's rule. As it is shown in Figure 3.45, the application of the 3-parameter inversion is very beneficial for the lithology examples that Gardner's rule fails.

3.4.3 Synthetic 2; Blackfoot Field

The 3-parameter joint inversion has been tested on synthetic 2. Comparing the condition number plot from the 3-parameter (Figure 3.46), with a small third singular value, with the plot from the 2-parameter joint inversion (Figure 3.13), shows that the 3-parameter joint inversion is less accurate and less stable than the 2-parameter joint inversion. The *I*, *J* and ρ estimates from the 2- and 3-parameter joint inversion of synthetic 2 are shown in Figure 3.47, displaying similar estimates for *I* and *J*.
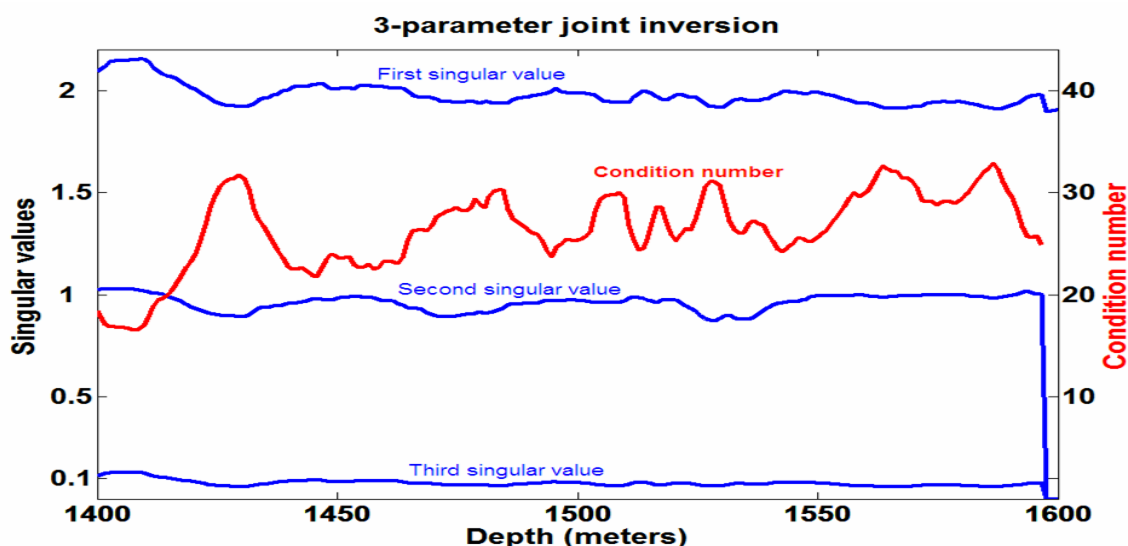
Figure 3.46: Singular values (in blue) and the condition number (red curve) versus depth of the 3-parameter joint inversion of synthetic 2.
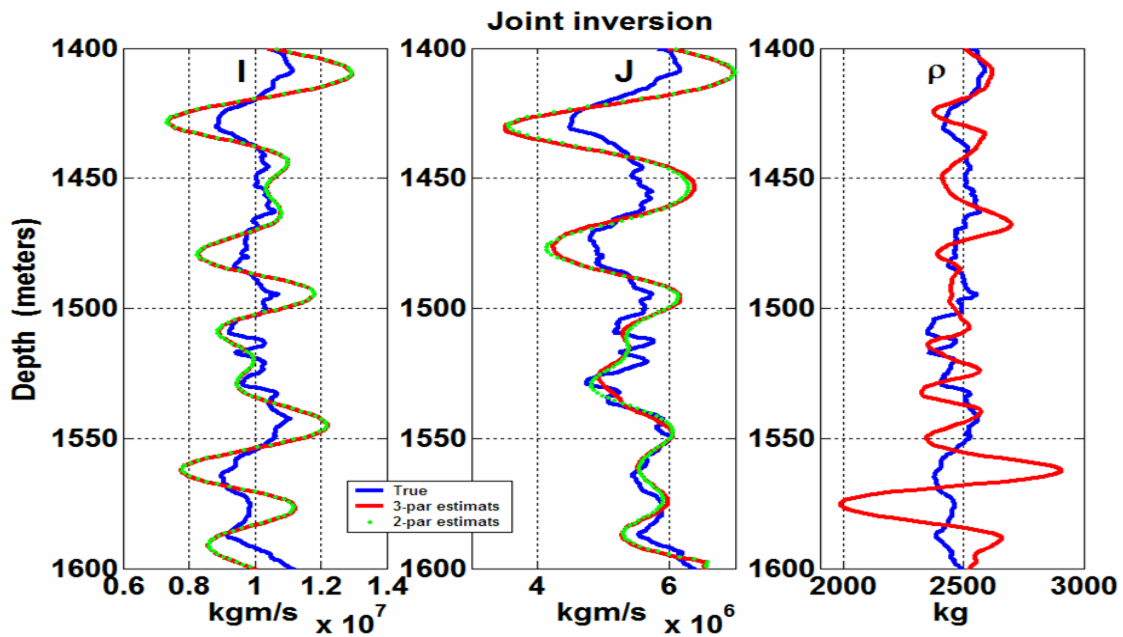
Figure 3.47: P-impedance: *I*, S-impedance: *J*, and density: ρ ,estimates from the 2- and 3-parameter joint inversions of synthetic 2.

As in the case of synthetic 1, for synthetic 2 the 3-parameter PP inversion has very high condition numbers (Figure 3.48), while PS inversion, for *J* and ρ, is a more stable inversion with smaller condition numbers. The 3-parameter PP inversion results are shown in Figure 3.49; the 3-parameter joint inversion has identical results for the *I* estimate and better results for *J* estimate than the PP inversion, but neither of them have good results for the ρ estimate. The PS inversion results, for *J* and ρ, are shown in Figure 3.50; the 3-parameter joint inversion has slightly better results for the *J* estimates than the PS inversion. It seems none of the inversions provide a good estimate of density (Figure 3.49 and Figure 3.50).
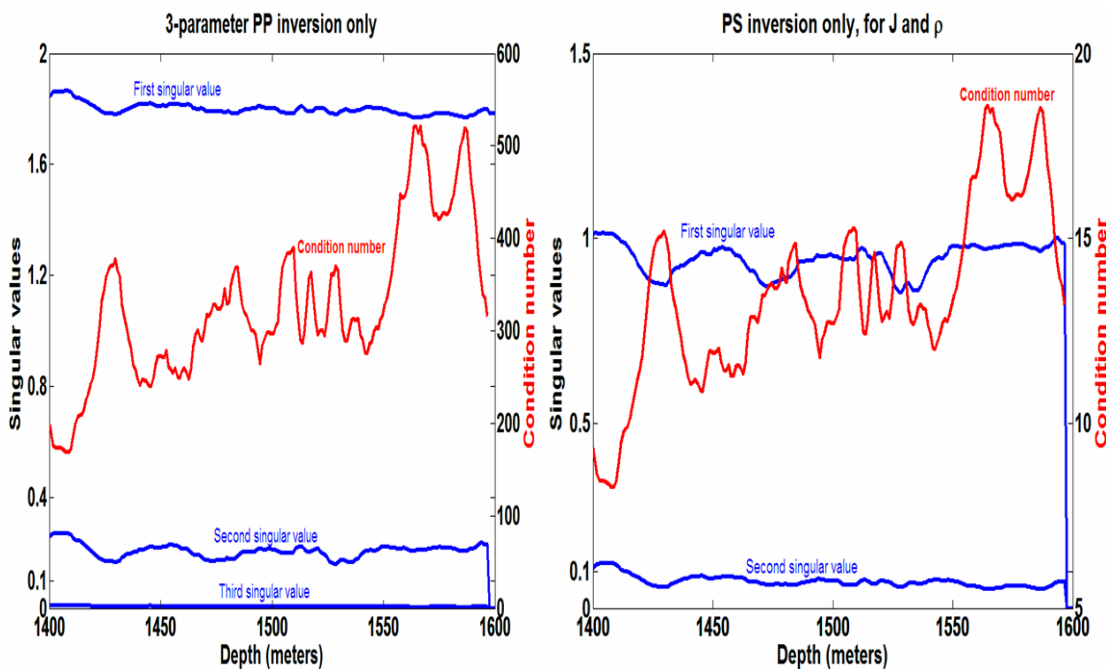
Figure 3.48: Singular values (in blue) and the condition number (red curve) versus depth, from the 3-parameter PP inversion (left plot); and PS inversion, for J and ρ, (right plot), of synthetic 2.
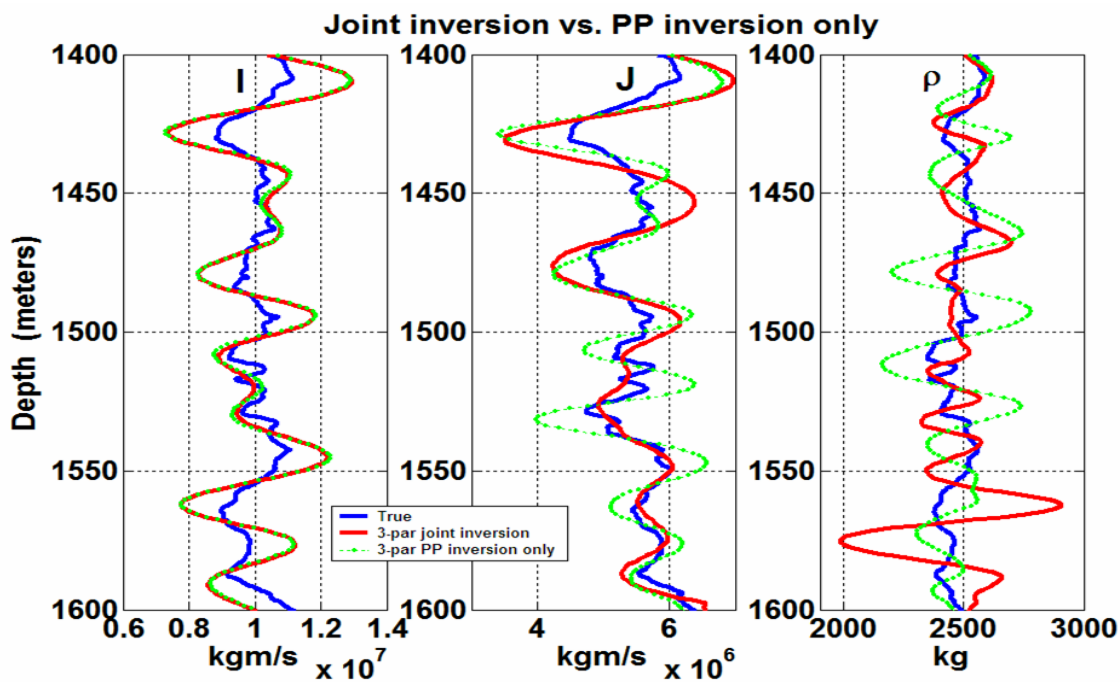
Figure 3.49: P-impedance: I, S-impedance: J, and density: ρ, estimates from the 3-parameter joint and PP inversions of synthetic 2.
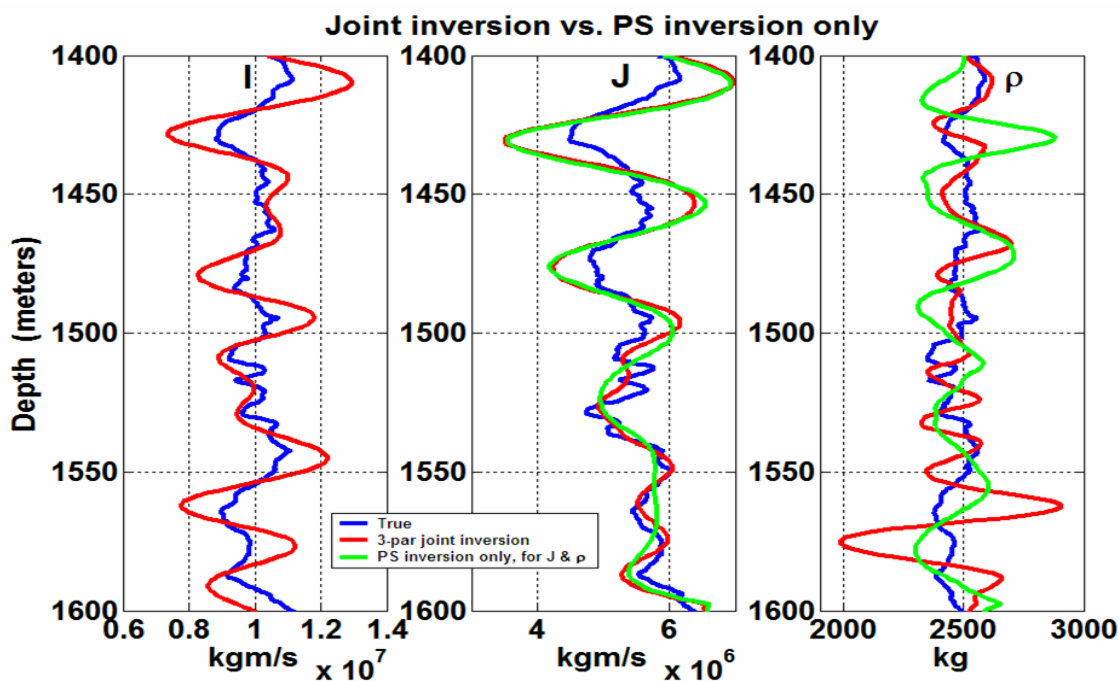
Figure 3.50: P-impedance: *I*, S-impedance: *J*, and density: ρ ,estimates from the 3-parameter joint and PS inversions, for *J* and ρ, of synthetic 2.

As seen from the inversion results of synthetic 1 and 2, overall, the joint inversion is better than inverting the PP or PS datasets separately. Still, joint inversion does not provide a good estimate for the density; as a remedy, the damped SVD method is applied to synthetic 2.

3.4.4 Damped SVD Method; Synthetic 2 Example

Jin et al., (1993) showed that the SVD can be effectively used for AVO stabilization. The SVD stabilization method consists of adding a small positive value to the smaller singular values (Section 2.4). Figure 3.51 shows the joint inversion results for synthetic 2, with 10% of the first singular value added to the singular values; the density

estimate is considerably improved, though the damped SVD only yields an approximate solution for density. In other words, the damping compromises the accuracy for AVO inversion, which is the price to pay for a reduced noise level; it reduces the model parameter resolution matrix. A detailed explanation of this statement is presented later for the Red Deer VSP data shown in Chapter 4.
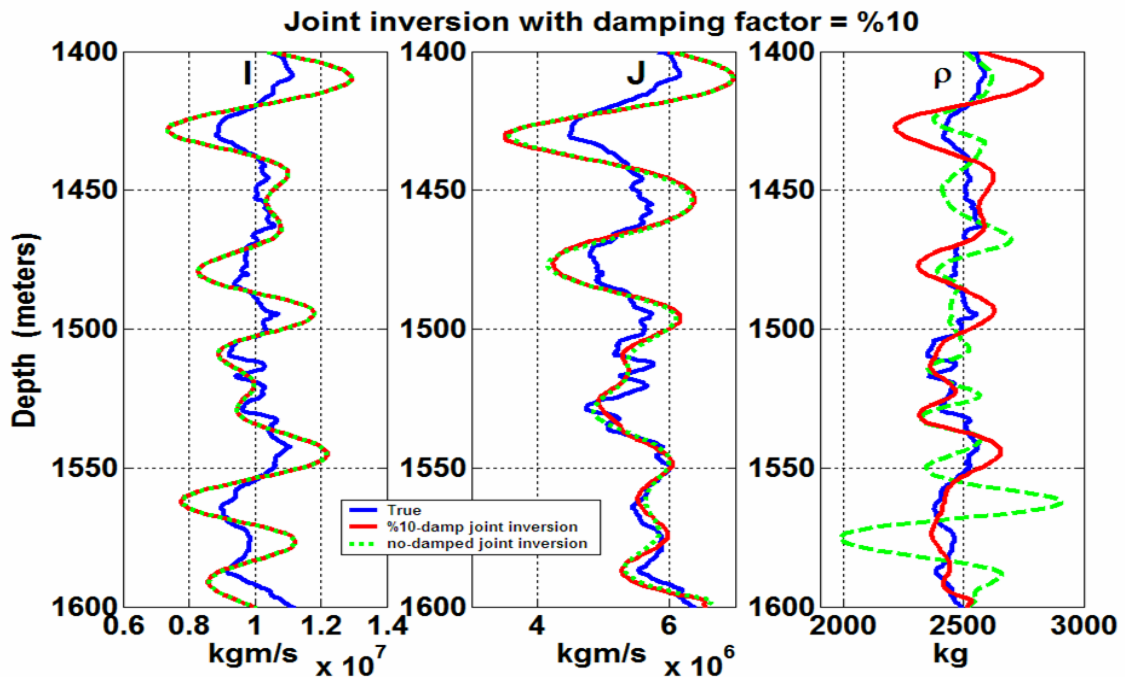
Figure 3.51: P-impedance: I, S-impedance and density estimates from 3-parameter joint inversion, with no damped SVD and %10 damped SVD, on synthetic 2 model.

3.4.5 Noise Effect on the 3-Paramater Joint Inversion

For the noisy synthetic 2 datasets, with a signal-to-noise ratio of 2, the 3-parameter joint inversion performs very stably for all three parameters (Figure 3.52), compared to either the 3-parameter PP inversion (Figure 3.53), or to the PS inversion for J and ρ

(Figure 3.54). The 3-parameter joint inversion performs very well in the presence of noise, confirming the strong advantage of the joint inversion.
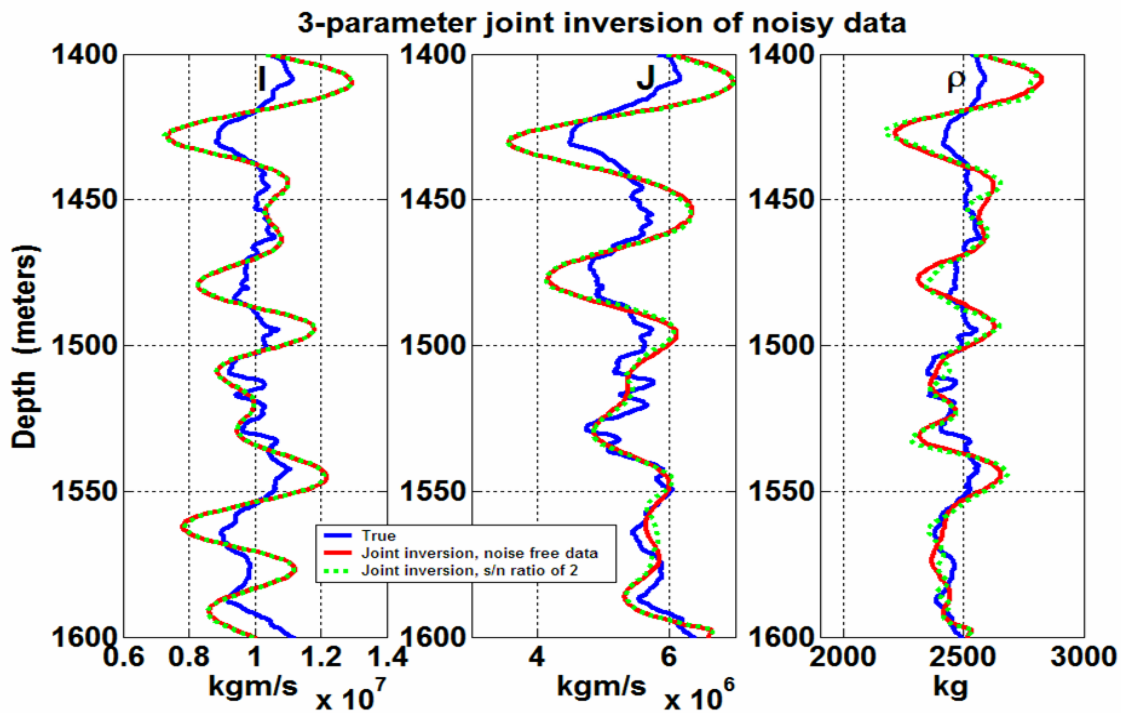
Figure 3.52: P-impedance: *I*, S-impedance: *J*, and density: ρ, from the 3-parameter joint inversion of the noisy synthetic 2, with a signal-to-noise ratio of 2.
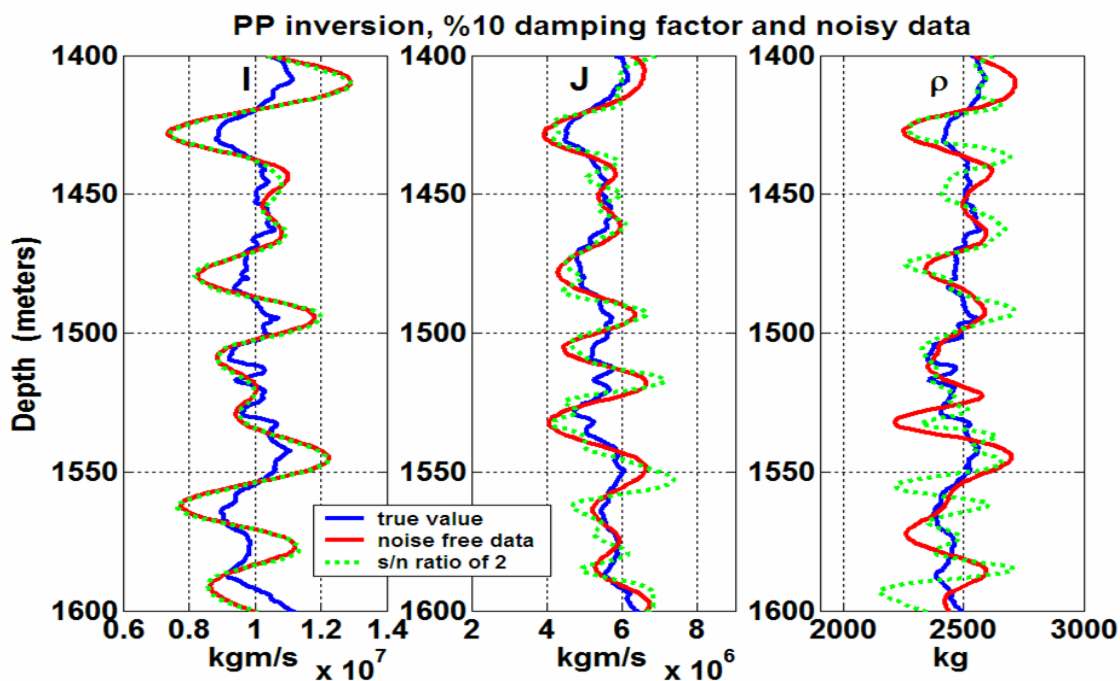
Figure 3.53: P-impedance: *I*, S-impedance: *J*, and density: ρ, from the 3-parameter PP inversion of the noisy synthetic 2, with a signal-to-noise ratio of 2.
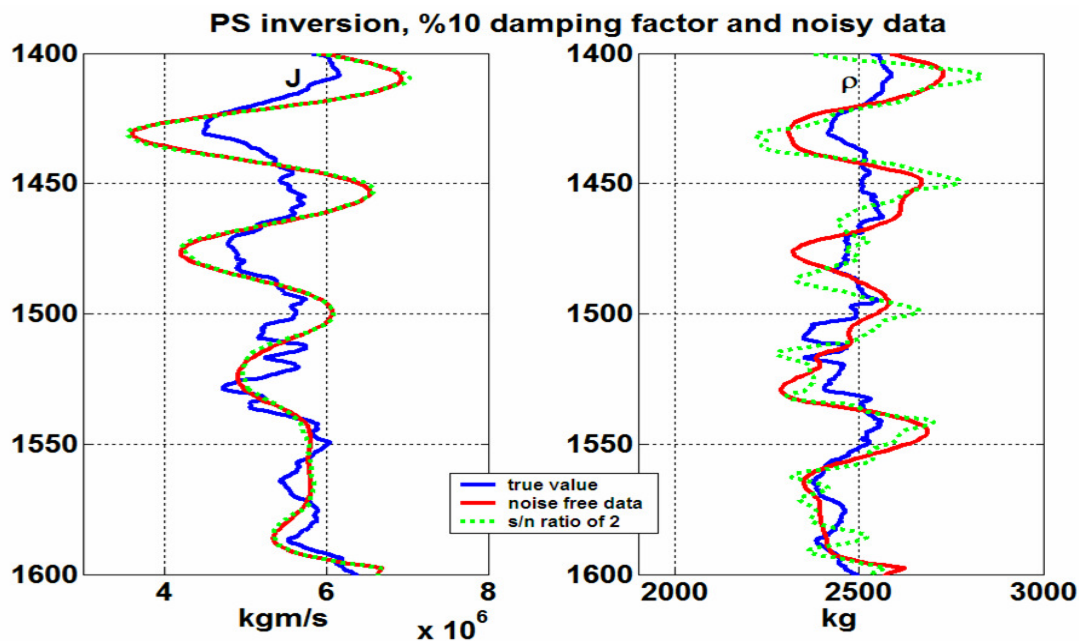
Figure 3.54: S-impedance: *J*, and density: ρ, from the PS inversion of the noisy synthetic 2, with a signal-to-noise ratio of 2.

3.4.6 Sensitivity of 3-Parameter Joint Inversion to Background Velocity

Calculating the coefficients of the Aki-Richards equations, a background velocity is needed in the raytracing to calculate the incident and reflection angles, and to generate the V_S/V_P factor. The determination of the background velocity is a big concern in any inversion. Unfortunately, a detailed background velocity is not provided, and well control or velocity analysis generally gives a rough velocity trend. To examine the effect of using an approximate velocity on the inversion results, the 3-parameter joint inversion has been examined with a few different smoothed velocities from the velocity model. For a non-smoothed, a moderately smoothed, and a highly smoothed P-wave velocity of the synthetic 2 model (Figure 3.55), the 3-parameter joint inversion results are shown in Figure 3.56; the 3-parameter joint inversion performs very stably with different smooth background velocities and the smoothing velocities has almost not effect on *I* and *J* estimates, although the density estimate is slightly affected. Therefore, the 3-parameter joint inversion is less sensitive to the background velocity error, and consequently, is not very sensitive to angle errors, as shown here under the assumption of horizontal layering geology in the raytracing, though the validation of the linear AVO inversion is not restricted to horizontal layering.
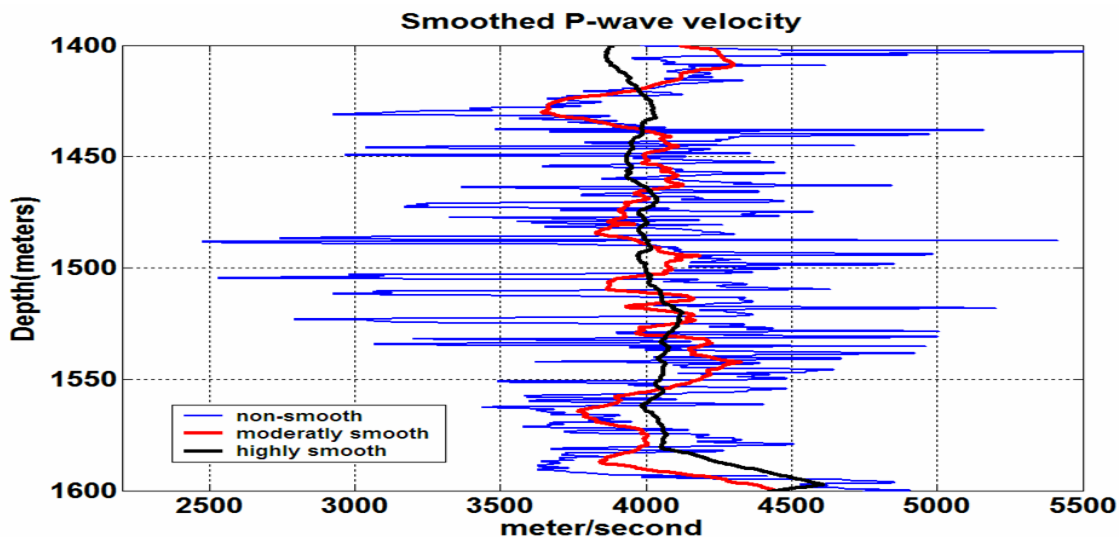
Figure 3.55: Synthetic 2, P-wave velocity, Blackfoot field.
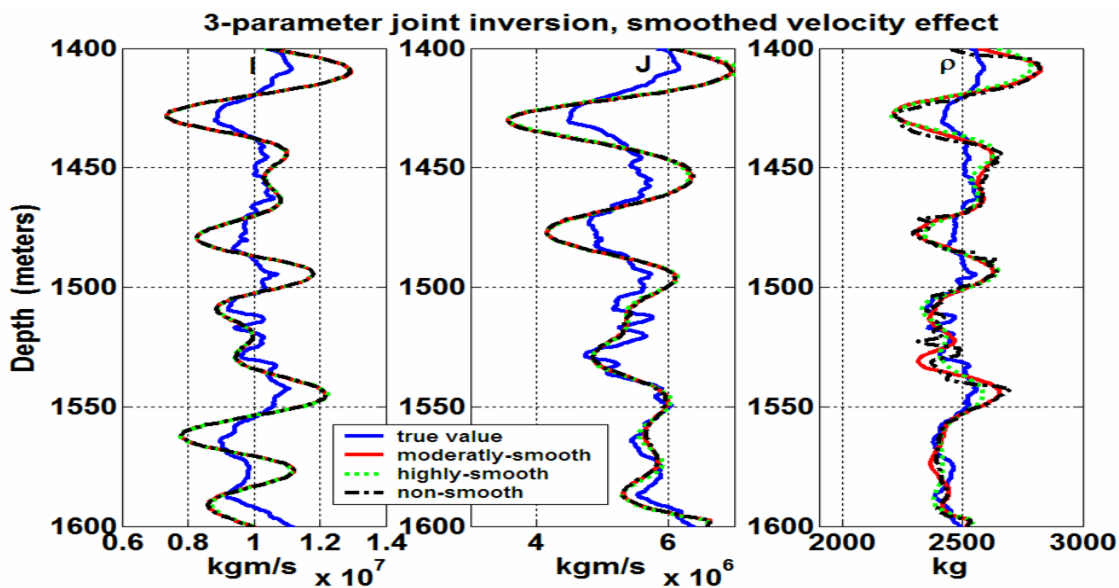
Figure 3.56: P-impedance: *I,* S-impedance: *J,* and density: *ρ*, from the 3-parameter joint inversion of synthetic 2 with a non-, moderately-, and highly smoothed background velocity.

3.4.7 Theoretical Accuracy of the Joint Inversion

The difference between the 3-parameter joint inversion estimates of I, J and ρ, and the true values is mainly due to two reasons: (i) using the linear Aki-Richards approximations instead of the exact Zoeppritz equations, and (ii) using the smoothed velocity model. The impact of smoothing the velocity has been examined for synthetic 2; there is no need to use the exact velocity information. To examine the reliability of the linear 3-parameter joint inversion for the synthetic 2 model, the input PP and PS synthetics were generated with a broad-band (spike) initial wavelet, and the exact velocity is used with no damping factor. The estimates of I, J and ρ (Figure 3.57), show that although the linear 3-parameter joint inversion provide good model parameter estimates, it is not perfect, especially for ρ. Therefore, the difference between the true and estimated values is due to the linear approximation for the reflection coefficients (Aki-Richard's equations). This confirms the necessity of using the non-linear AVO inversion in estimating the three parameters. The condition number plot for this example in shown in Figure 3.58.
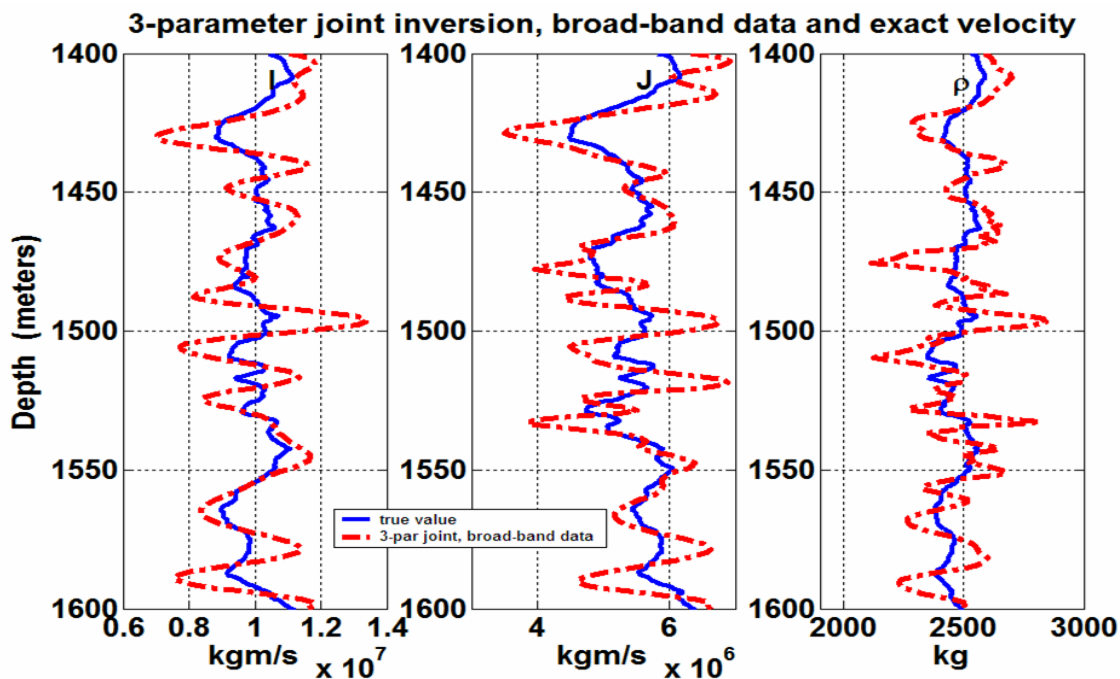
Figure 3.57: P-impedance: *I,* S-impedance: *J,* and density: ρ, from the 3-parameter joint inversion of broad-band data of synthetic 2, with exact background velocity.
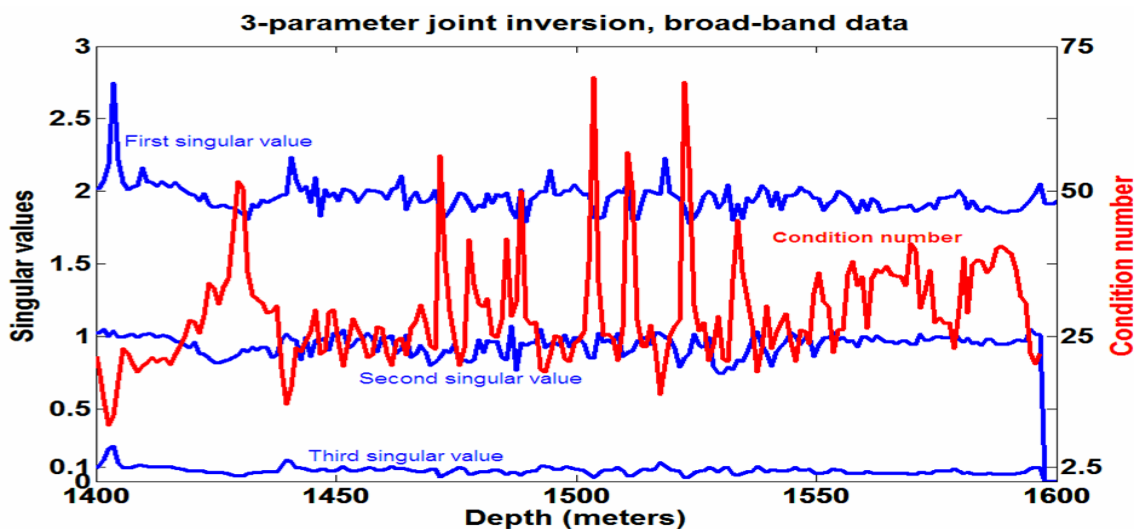
Figure 3.58: P-impedance: *I,* S-impedance: *J,* and density: ρ, estimate from the 3-parameter joint inversion of broad-band data from synthetic 2, with exact background velocity.

3.4.8 Synthetic 3, Red Deer Field

The 3-parameter joint inversion has been applied to the Red Deer synthetic data. The condition number plots of the 3-parameter PP, joint and the PS inversion for J and ρ (Figure 3.59 and Figure 3.60) show that although all inversions are ill-posed for the depth of 280-300 m (low velocity layer, Figure 3.15), they all are well-posed for the rest of the depths. The high condition number values of the 3-parameter PP inversion (Figure 3.60, left) show that the compressional data is incapable of resulting in good estimates; while much smaller condition number values from the PS inversion indicates of capability of the converted shear data in estimating the two parameters J and ρ. The I, J and ρ estimates from the three inversions are shown in Figure 3.61.

The AVO inversion of the Red Deer synthetic data illustrates the difficulty in obtaining good estimates of the I, J and ρ for the low velocity layer, the Ardley coal zone described in Chapter 4. At this low velocity layer the ill-posedness of the AVO inversion depends only on the geometry of the problem and not the data, which might result in an unstable and unrealistic estimate (at least for one of the parameters) no matter how precise the data are.
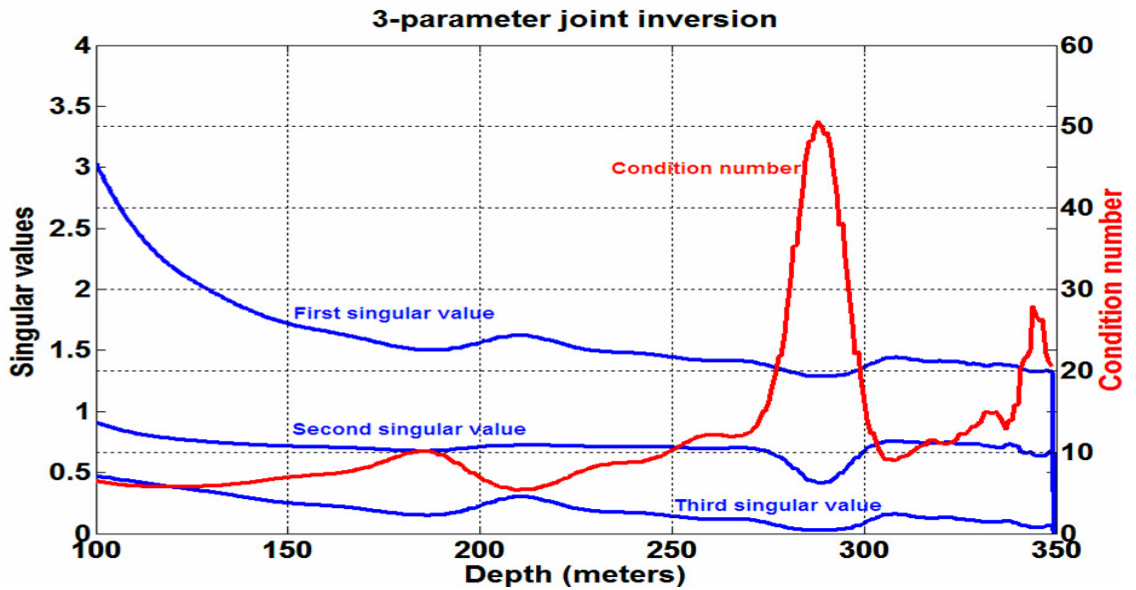
Figure 3.59: Singular values, blue, and condition number, red, versus depth, of the joint inversion of synthetic 3.
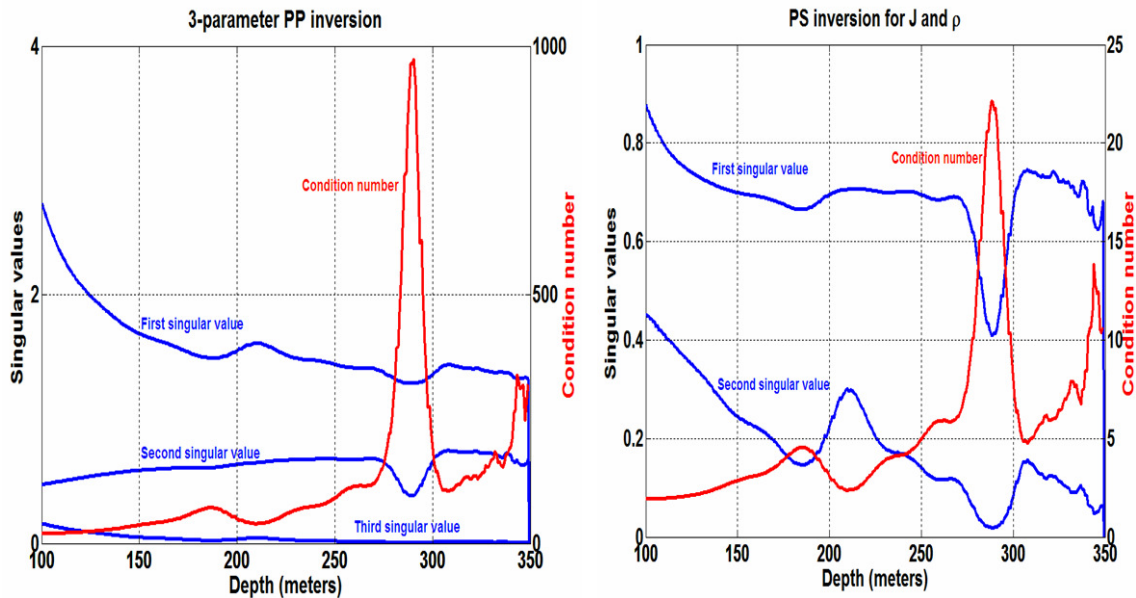
Figure 3.60: Singular values (in blue) and the condition number (red curve) versus depth, from the 3-parameter PP inversion (left); and PS inversion, for the J and ρ, (right) of synthetic 3.
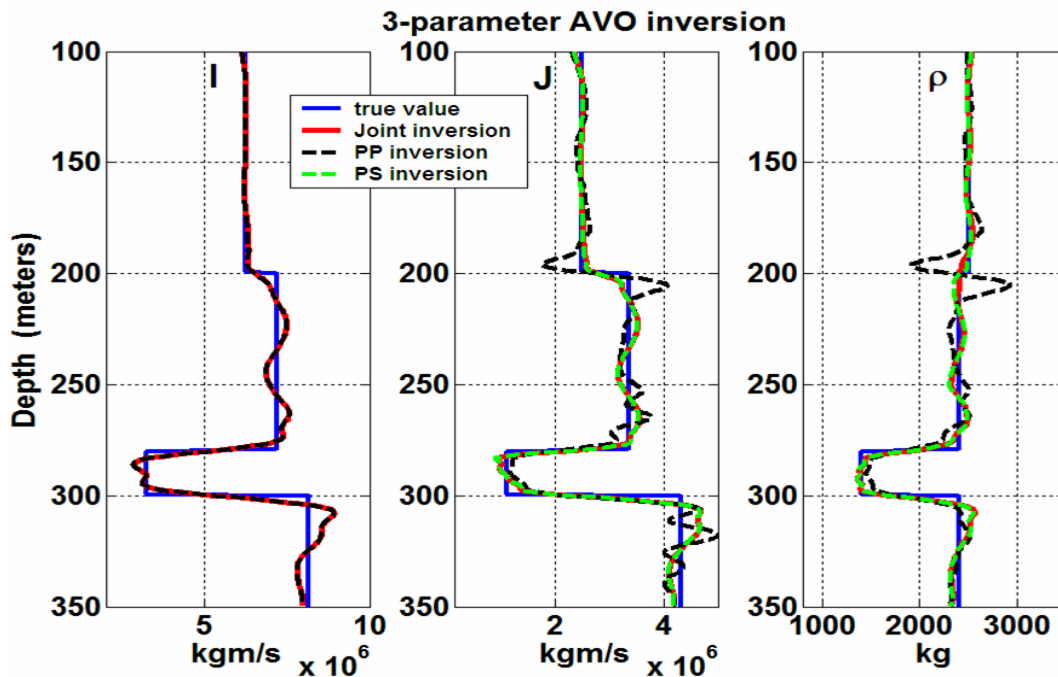
Figure 3.61: P-impedance: *I,* S-impedance: *J,* and density: ρ, estimates from the 3-parameter PP and joint inversions and PS inversion, for *J* and ρ.

3.5 Chapter Summary

The linear joint AVO inversion described by Larsen and Margrave (1999) has been cast as a MATLAB algorithm called 2-parameter joint inversion. This algorithm includes some modifications to Larsen and Margrave's approach: (1) deriving impedance estimates from P- and S-impedance reflectivity traces; and (2) restoring the low-frequency components to the impedance estimates. Additionally, the joint inversion performance in comparison with the PP and PS inversion is documented.

The 2-parameter joint inversion has been extended to the 3-parameter joint inversion to estimate the P-impedance, S-impedance, and density. The 3-parameter joint inversion implementation is presented in detail. At each sample depth, over a range of

source-receiver offsets, the smoothed background velocity is raytraced to calculate the incident and reflected angles, required for constructing the matrix of coefficients of Aki-Richards equations. Assuming that the PP and PS reflection data provide estimates for PP and PS reflection coefficients, the amplitude of pre-stack CMP gather (PP case) and CCP gather (PS case) is the reflection data. The PP and PS reflection data is converted form time to depth, in order to be correlated and scaled to represent the reflectivity. Then the PP and PS data least-squares fitted to the Aki-Richards equations. The inverse of the matrix of coefficient, multiplied by the data, yields the P-impedance, S-impedance and density reflectivities. The inverse of the matrix of coefficients is calculated using the least-squares and SVD methods. As a measure of the singularity of the matrix, the condition number has been studied. Then in inverting the ill-posed matrices, the damped SVD method has been used.

The testing of the 2-parameter and 3-parameter AVO inversion on several synthetic examples has been presented in this chapter. Testing of the AVO inversion led to the following observations:

- In the 2-parameter joint inversion, the PP data dominates in the I estimate, while the PS data dominates in the J estimate. This effect is used as an indicator for choosing the right polarity of the PP and PS data.

- The 2-parameter PP and PS inversions are each able to estimate one parameter successfully, while the 2-parameter joint inversion is capable of providing good estimates for both the I and J. The PP inversion provides a good estimate for I

similar to the joint inversion and the PS inversion provides good estimates for J and ρ similar to the joint inversion.

- Restoring the low frequencies has a significant effect on the AVO inversion estimates.

- In an AVO inversion, adding the fold of data, by incorporating more far offsets data, will lead to better model parameter estimates. The further offset incident angles should be pre-critical and adding the post-critical far offsets data will ruin the model parameter estimates.

- The 2-parameter PP inversion has a smaller condition number than the PS inversion (for I and J), and the joint inversion has the smallest condition number for all the depths; the condition number decreases with increasing the fold of data in the AVO inversion.

- A smaller condition number might produce better I and J estimates from 2-parameter joint inversion than the PP or PS inversions, and the plots of estimates for synthetic examples confirm this fact.

- The SVD method is equivalent to the least-squares method for the well-posed cases; furthermore, the SVD has the best least-squares solution for ill-posed cases.

- The 3-parameter joint inversion (with higher condition number values) is a less stable problem compared to the 2-parameter joint inversion,

- The linear joint inversion is less sensitive to the background velocity errors; therefore, the angle errors (from raytracing) will not strongly bias the joint

inversion results, as shown here under the assumption of horizontal layering geology.

- In presence of random noise in the data, the joint inversion is more accurate for all parameters than PP or PS inversions. The joint inversion has very good estimates for both I and J and reasonable estimate for the ρ even in the presence of noise. Inverting the noisy compressional data by a 2- or 3-parameter PP inversion provides similar results for the I estimate compared to the 2- or 3-parameter joint inversion. Also, inverting the noisy converted shear data with a PS inversion (for I and J or for J and ρ) provides similar results for the J estimate compared to the 2- or 3-parameter joint inversion.

- The PS inversion, for the J and ρ, has comparable results to the 3-parameter joint inversion even for the noisy data sets.

- In the PS inversion, the choice of parameters is not neutral. Although theoretically the same, the PS inversion for I and J has a much higher condition number compared to the PS inversion for the J and ρ.

CHAPTER 4: Cygnet 9-34 VSP Processing for AVO Inversion

4.1 Introduction

VSP data can provide valuable information for the characterization of reservoir lithology, fracture, and fluids (Dewangan, 2003). VSP data have higher resolution than surface seismic images, and provide more accurate details about the earth's properties when performing AVO inversion. A VSP was acquired for the Ardley coal zone strata near Red Deer, Alberta to demonstrate the effectiveness of multi-component seismic application in coalbed methane development (Richardson, 2003); the AVO inversion of Red Deer VSP data has been completed in this thesis. Survey parameters and the geology of the study area are outlined in this chapter. The processing flow for the VSP data, prior to input to the AVO inversion, is presented.

4.2 Vertical Seismic Profile

A vertical seismic profile (VSP) records energy traveling from a surface source to receivers in a borehole. VSP data have higher lateral resolution than surface seismic data for the same depth, due to a smaller Fresnel zone (Hardage, 1985); frequencies are higher in VSP data because of their shorter one-way travel paths through the severely

attenuating near surface and the underlying strata. This yields a wider bandwidth and an improved lateral resolution. Most VSPs use a surface seismic source such as a vibrator truck on land, or an air gun in offshore environments. VSPs include the zero-offset VSP and the walkaway VSP. For a zero-offset VSP, the source is positioned directly above the receivers very close to the borehole. Walkaway VSPs use a number of source locations that increase in lateral distance from the borehole. In this thesis, the AVO inversion of both zero-offset and walkaway VSPs have been studied.
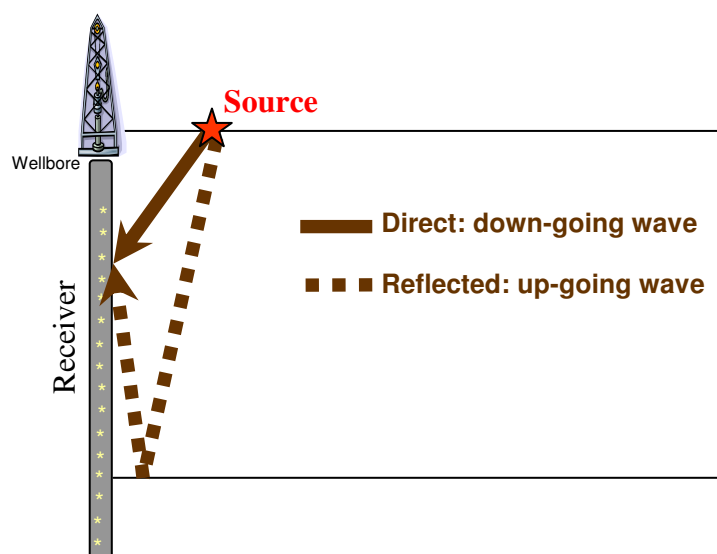
Figure 4.1: The direct, down-going wave, and the reflected, up-going wave in a VSP.

A VSP records both the direct downgoing wavefield and the reflected upgoing wavefield at each receiver position (Figure 4.1). The total recorded wavefield in a VSP consists of downgoing and upgoing wavefields. The upgoing wavefield, which includes the primary reflections, is separated from the downgoing wavefield, and deconvolved to remove the effect of the source signature from the upgoing energy. The upgoing

wavefield is flattened to represent the reflection data in two-way time, so it can be compared to surface reflection seismic data. It is the deconvolved upgoing wavefield that is the input data to the AVO inversion.

4.3 Study Area

The VSP data were acquired at the Cygnet 9-34-38-28W4 lease located northwest of Red Deer, Alberta. At this location, Suncor Energy Inc., with industry partners, and the Alberta Research Council, were evaluating the Upper Cretaceous Ardley coal zone for its coal bed methane (CBM) potential, as well as testing enhanced coalbed methane recovery with carbon dioxide injection (Richardson, 2003). Methane production and carbon dioxide injection are both being tested for viability within the Upper Cretaceous Ardley coal zone, as it is one of Alberta's most prospective CBM targets (Richardson, 2003). The Ardley coal seam is located at the top of the Scollard Formation just beneath the interbedded sands and shales of the Tertiary Paskapoo Formation (Figure 4.2).
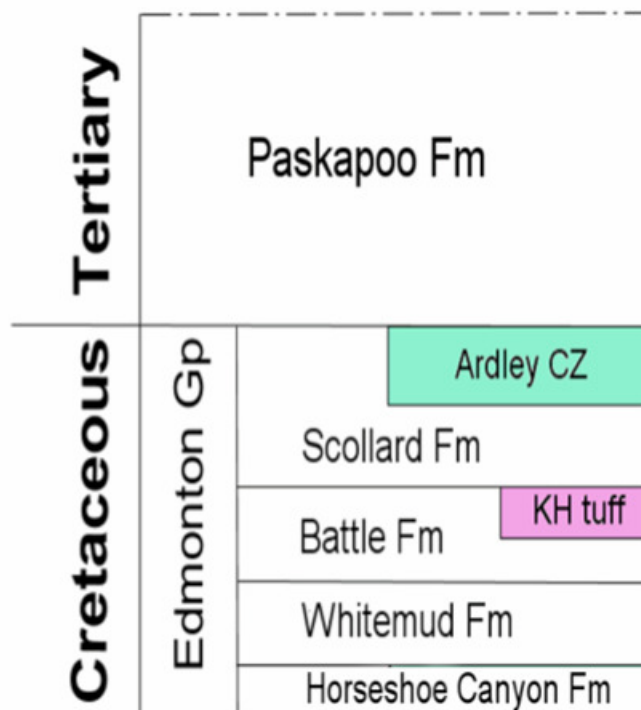
Figure 4.2: Stratigraphic column showing upper Cretaceous/Tertiary strata in the Central Plains of Alberta Cretaceous sediments (courtesy of Richardson, 2003).

4.3.1 Well Logs

The velocity model for this study comes from the well logs obtained by Schlumberger Canada after the Red Deer well was drilled. Compressional sonic, shear sonic and bulk density logs were all run from TD to approximately 40 m below KB. Figure 4.3 shows these logs. The Ardley coal zone is 11.7 m thick, located at a depth of 284 m below surface; TD is at a depth of 300 m (Richardson, 2003). Coal has a low seismic velocity and low density with respect to its boundary strata; thus, although coal seams are extremely thin with respect to seismic wavelength, their exceptionally large acoustic impedance contrast with surrounding rocks results in a distinct reflection

(Gochioco, 1991). The limits of resolution for coal beds are approximately λ/8, and their limit of detection is less than that for other strata - often more than λ/40 (Gochioco, 1992).
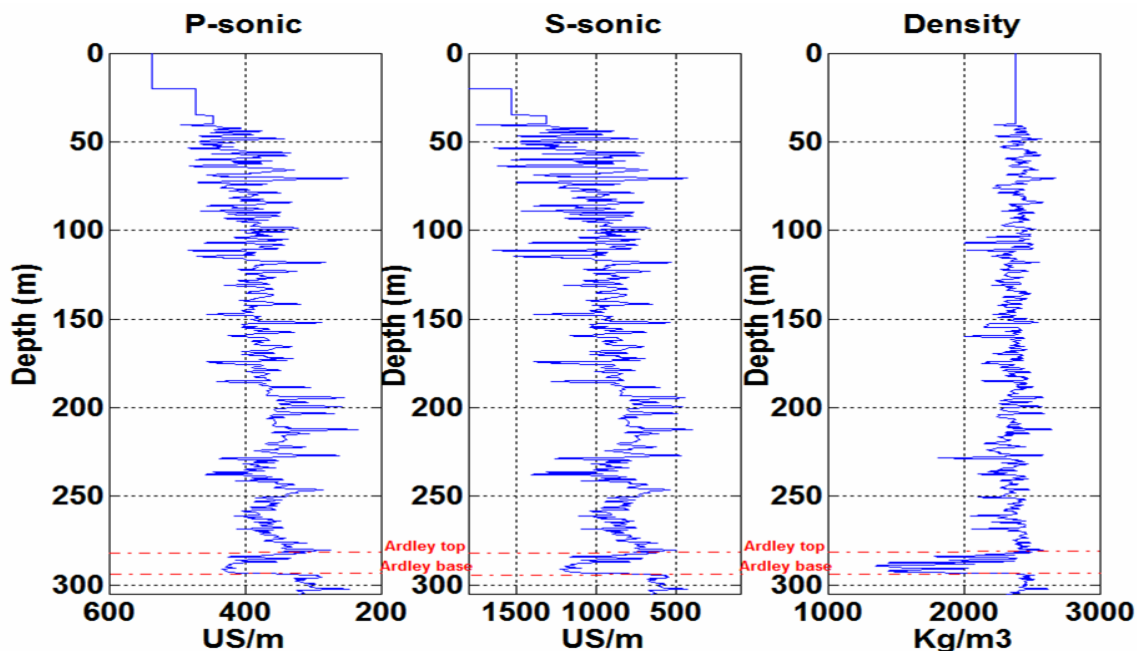
Figure 4.3: Well logs from the Cygnet 9-34 well with coal top and base annotated.

4.4 Survey Geometry

Three zero-offset VSPs were acquired by Schlumberger on the lease site: a Big-P compressional source with a sweep from 8 to 150 Hz, a Mini-P compressional source with a sweep from 8 to 250 Hz, and a Mini-S shear source with a sweep from 8 to 150 Hz (Richardson, 2003). A walkaway VSP with four source locations was also acquired using the Big-P and Mini-P sources. The geometry for all surveys is illustrated in Figure 4.4. The zero-offset VSP sources were located 20 m east of the borehole. The four walkaway

shot points east of the borehole were at the following offsets: 100 m, 150 m, 191 m,
and 244 m from the borehole. Data was acquired between 294.5 m and 19.5 m at 5 m
intervals for the zero-offset surveys and between 294.5 m and 114.5 m at 15 m intervals
for the walkaway VSPs (Richardson, 2003).
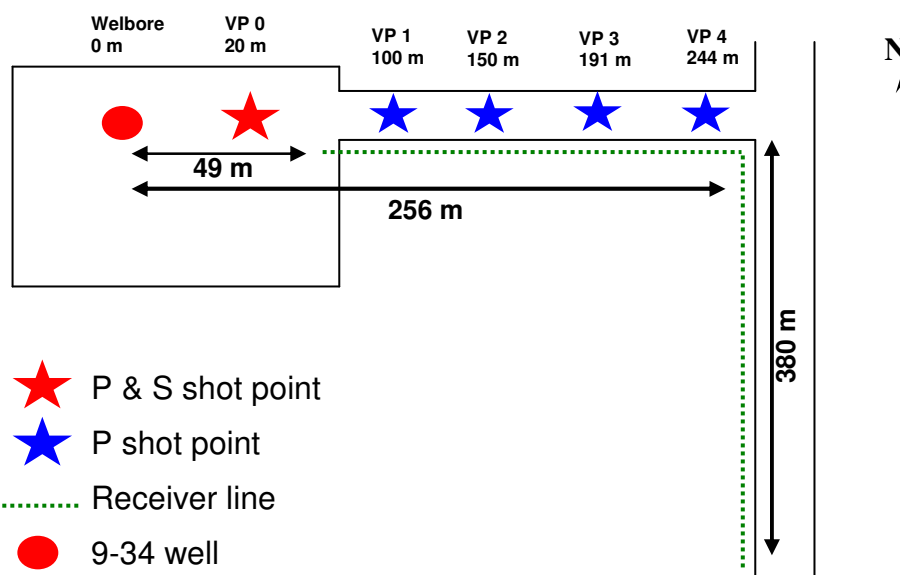
Figure 4.4: Survey geometry for zero-offset and walkaway VSP surveys acquired on the Cygnet
9-34 lease. Zero-offset sources were located at VP0. Walkaway sources were located from VP1
to VP4 (courtesy of Richardson, 2003).

Coal seams are often very thin, resulting in the need for high-bandwidth data to
properly image seams. The Ardley coal zone contacts at the Red Deer site may be
effectively imaged using any of the three sources tested, but lithological changes within
the coal may be detected using the high-frequency Mini-P source (Richardson, 2003).
Therefore, in this study only the zero-offset and walkaway VSP common shot gathers
from Mini-P source have been used.

A CDP gather is required in order to incorporate the reflection data for an AVO study. The VSP geometry is like the geometry of a common-shot gather (Yilmaz, 1987); however a common-shot gather can be considered a CDP gather at the half way point between the source and well provided that the subsurface consists of horizontal layers with no lateral velocity variations. Within Alberta, Ardley coal seams are laterally continuous over tens of kilometres (Beaton, 2003). So, the assumption of horizontal layers with no lateral velocity variation is reasonable for the Red Deer data. Therefore, for the AVO inversion of Red Deer VSP data, a common shot gather is considered as a CDP gather unless otherwise specified. The next section briefly explains the processing flows used for both zero-offset and walkaway VSP.

4.5 VSP Processing

Nearly all current seismic data processing techniques are adaptable to the processing of VSP data (Balch, 1982). This section presents a short review of VSP data processing. The zero-offset and walkaway VPS data were processed prior to the AVO inversion. The zero-offset vertical component and walkaway VSP data were processed by Schlumberger Canada; in addition, the zero-offset data was processed using ProMAX VSP.

4.5.1 Schlumberger Zero-offset Processing

Schlumberger's processing flow for zero-offset VSP is outlined in Figure 4.5. The deconvolved upgoing wavefield that was input to the AVO inversion is shown in Figure 4.6.

```
                    ┌─────────────────────────┐
                    │   Geometry assignment   │
                    └─────────────────────────┘
                                 │
            ┌────────────────────────────────────────┐
            │  Stack multiple shots by median algorithm │
            └────────────────────────────────────────┘
                                 │
                    ┌─────────────────────────┐
                    │    Pick first arrivals  │
                    └─────────────────────────┘
                                 │
                    ┌───────────────────────────┐
                    │ Temporal Amplitude Recovery │
                    └───────────────────────────┘
                                 │
            ┌────────────────────────────────────────┐
            │  Spatial Amplitude Normalization RMS    │
            └────────────────────────────────────────┘
                                 │
                    ┌─────────────────────────┐
                    │   Wavefield separation  │
                    └─────────────────────────┘
```

Geometry assignment

Stack multiple shots by median algorithm

Pick first arrivals

Temporal Amplitude Recovery

Spatial Amplitude Normalization RMS

Wavefield separation

Downgoing wavefield

Upgoing wavefield

Design inverse filter

Median filter data enhancement

Waveshaping bottom level deconvolution

Median filter data enhancement

Deconvolved upgoing wavefield

Figure 4.5: Processing flow used to process zero-offset VSP data, Schlumberger (Courtesy of Richardson, 2003).
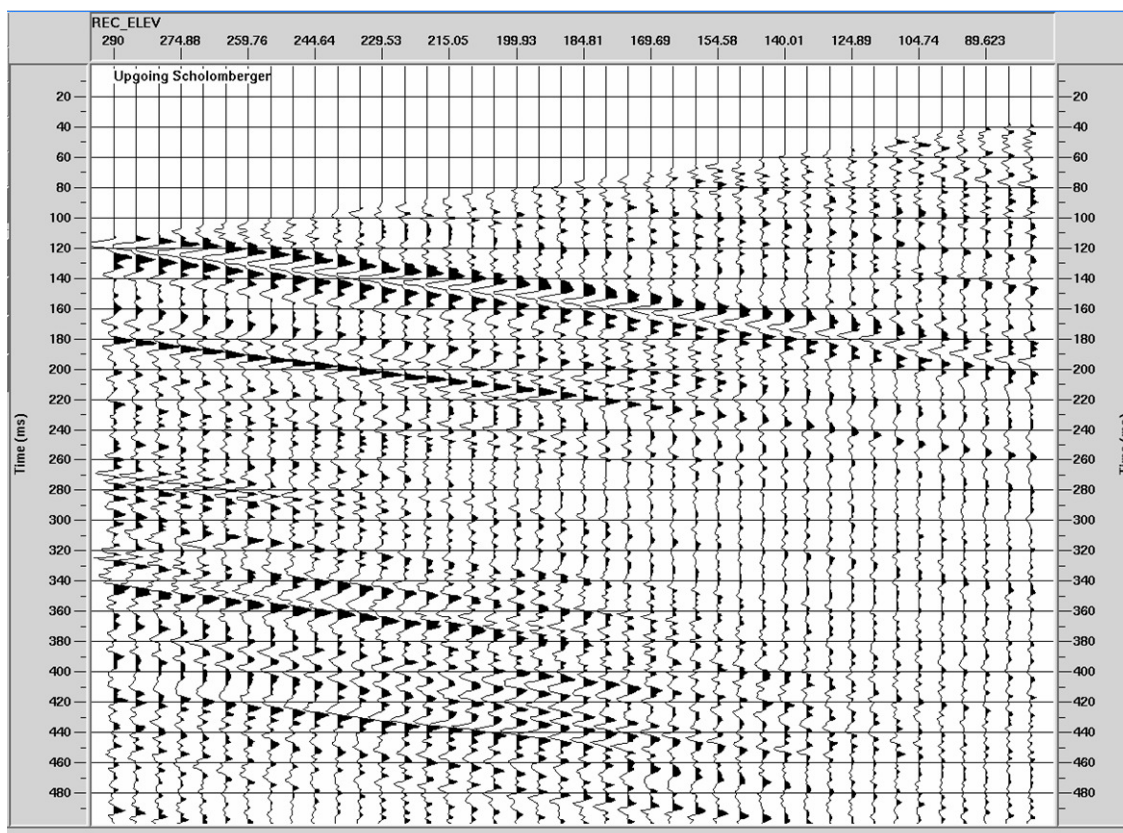
Figure 4.6: PP deconvolved upgoing wavefield (processed by Schlumberger).

4.5.2 ProMAX Zero-Offset Processing

ProMAX processing of zero-offset data used a flow very similar to that used by Schlumberger (Figure 4.8). Survey geometry was assigned to the vertical components (PP data), multiple shots were stacked, and the first-break times were picked on the direct arrival picks (Figure 4.7). The first-break times and the receiver's depth can be used to calculate the average velocity from the source to each receiver depth. Geometrical spreading compensation requires RMS velocities, so the average velocity is converted to RMS velocity. This allows the true amplitude to be recovered. Noisy traces were killed

from the data (Figure 4.7).

Based on the amplitude spectrum, a band pass filter was applied to remove high frequency noise in the data. The wavefields were separated using a 1-D median velocity filter based on the first-break picks. Median filters smooth the data along a particular velocity trend, while suppressing the other trends. To apply the median filter, the downgoing wavefield is flattened by subtracting the first-break times; the upgoing wavefields appear as dipping events. An 11 trace median filter was used to suppress the upgoing wavefield and separate the downgoing wavefield (Figure 4.9). A 10 ms time window around the direct arrivals (Figure 4.9) was used as the initial wavelet in the design of the deconvolution operator. The upgoing wavefield was obtained by subtracting the downgoing wavefield from the total wavefield. The upgoing wavefield is displayed in one-way-time in Figure 4.10; tube waves can be identified in the upgoing wavefield.

Tube waves occur when the surface waves generated by the source come in contact with the fluids in a borehole and become guided waves (Coueslan, 2005). When the tube wave encounters a change in the diameter of the borehole, or reaches the bottom of the well, then it will be reflected back to the surface and recorded by receivers. Tube waves are one of the most damaging types of noise that can exist in VSP because they represent a coherent noise mode and can not be reduced by repeating seismic shots (Hardage, 1985).

To remove the coherent tube waves, a radial filter is used; the radial filter is designed based on a radial transform to eliminate coherent linear noise (Henley, 2003). The radial transform maps the data from offset-time domain into apparent velocity-time

domain; in this domain the linear coherent noise is easily separated. The deconvolved

upgoing wavefield is shown in two way time (Figure 4.11). This wavefield is input to the

AVO inversion.
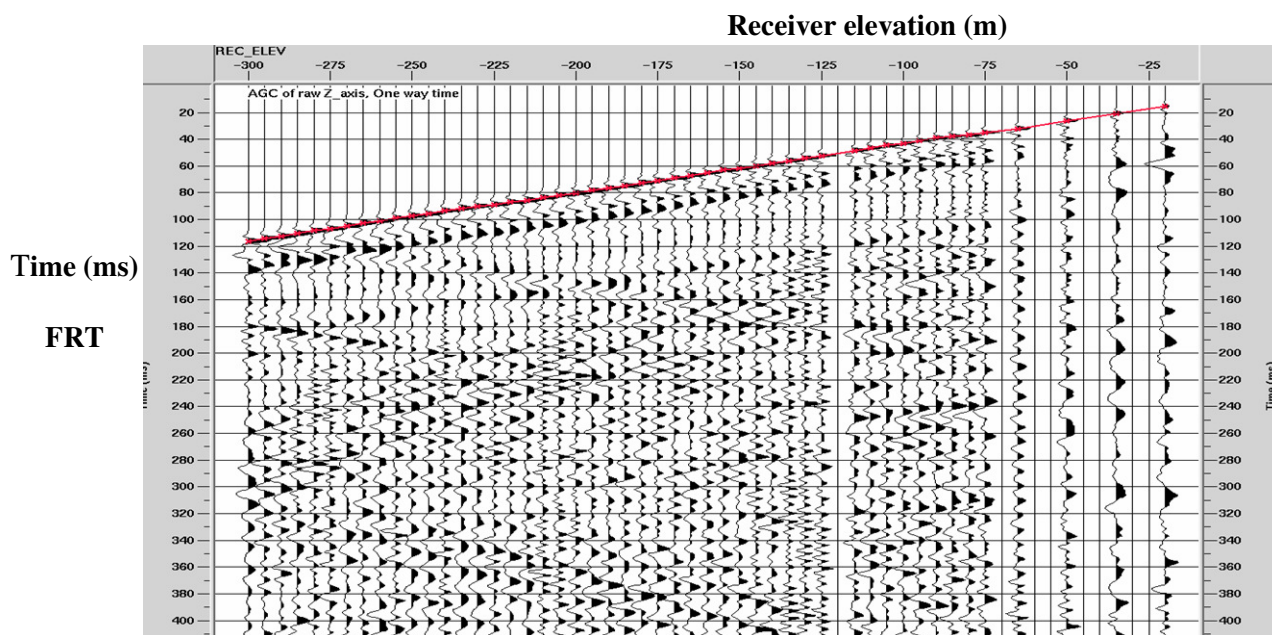
Figure 4.7: The stacked zero-offset data. First-break picks are shown in red. Blank traces

represent the noisy traces killed from the dataset.

```
┌─────────────────────────┐
│   Geometry assignment   │
└─────────────────────────┘
            │
            ▼
┌──────────────────────────────────┐
│ Stack multiple shots by median algorithm │
└──────────────────────────────────┘
            │
            ▼
┌─────────────────────┐
│  Pick first arrivals │
└─────────────────────┘
            │
            ▼
┌──────────────────────────┐
│ Calculate average velocity │
└──────────────────────────┘
            │
            ▼
┌──────────────────────┐
│ Convert to RMS velocity │
└──────────────────────┘
            │
            ▼
┌──────────────────────────┐
│  True Amplitude Recovery  │
└──────────────────────────┘
            │
            ▼
┌─────────────────────┐
│   Band pass filter   │
└─────────────────────┘
            │
            ▼
┌──────────────────────────┐
│    Wavefield separation   │
│     By median filter      │
└──────────────────────────┘
```
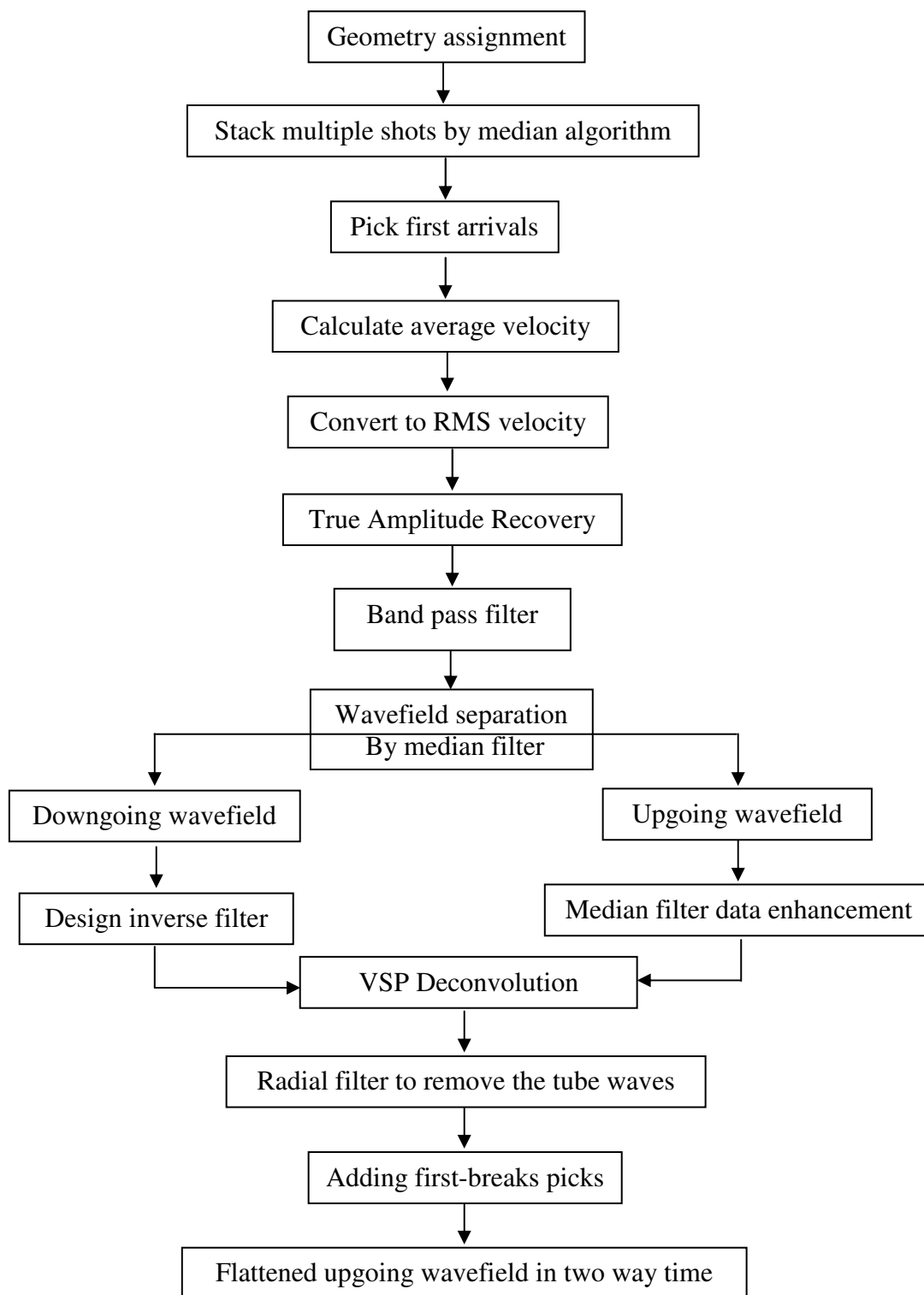
Figure 4.8: Processing flow used to process zero-offset VSP data using ProMAX.

- Downgoing wavefield
- Upgoing wavefield
- Design inverse filter
- Median filter data enhancement
- VSP Deconvolution
- Radial filter to remove the tube waves
- Adding first-breaks picks
- Flattened upgoing wavefield in two way time
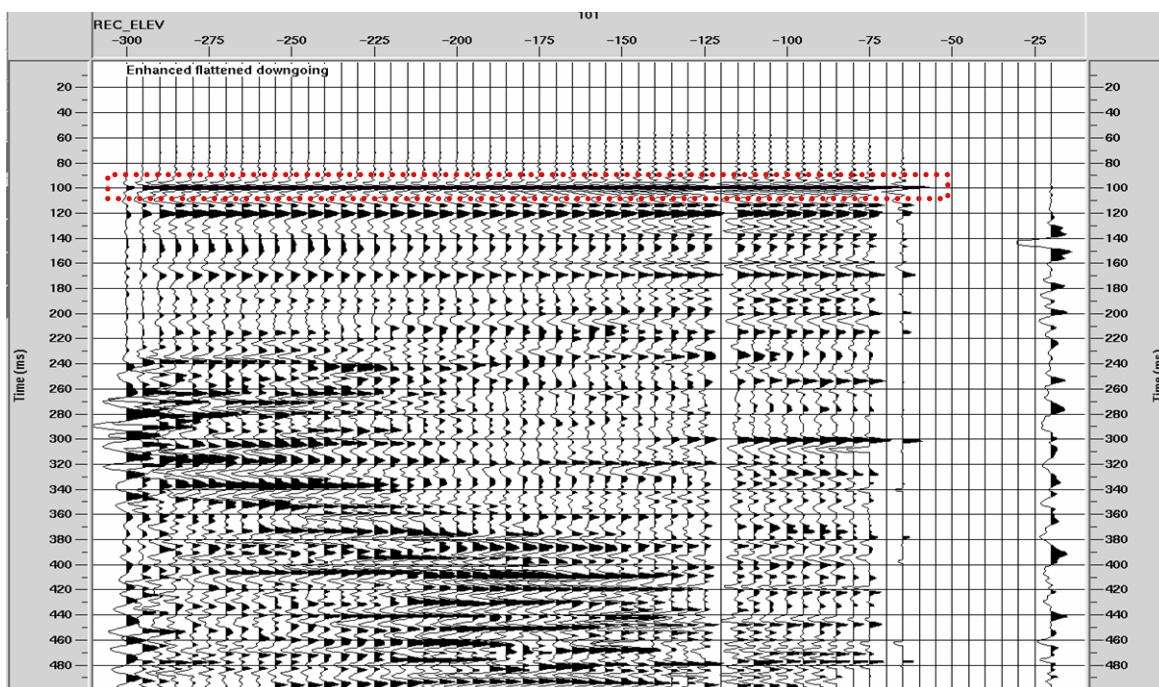
Figure 4.9: The separated downgoing wavefield. The time window used in designing the deconvolution operator is shown in red.
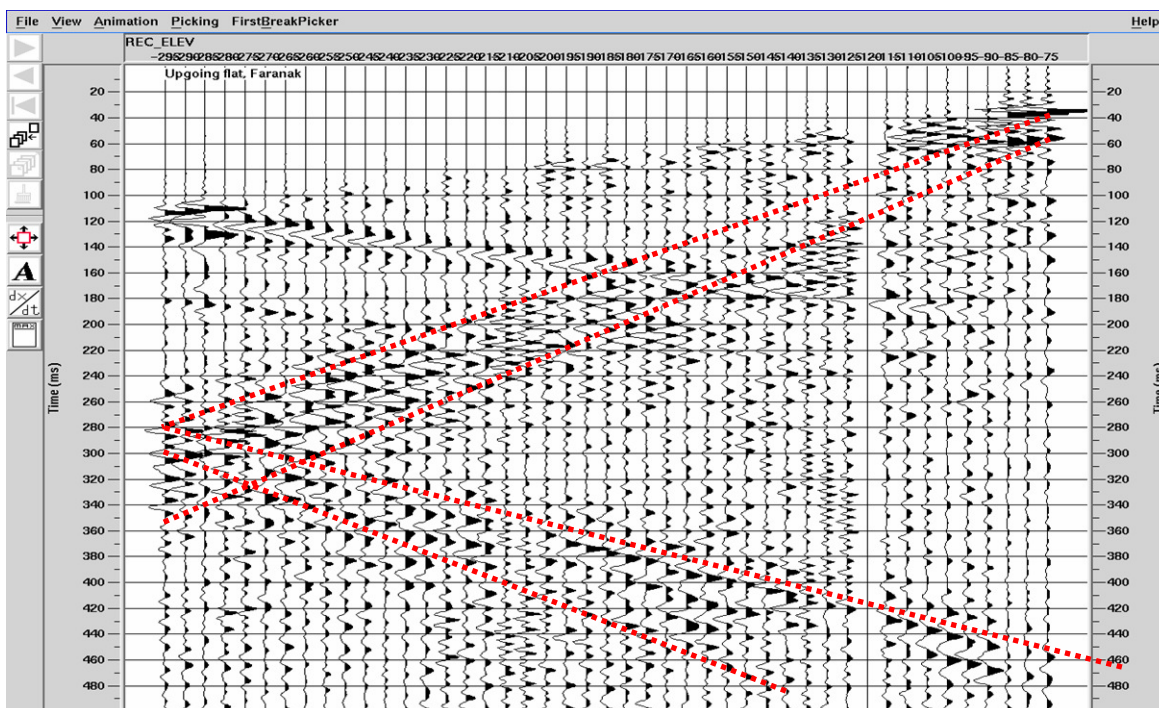
Figure 4.10: The separated upgoing wavefield. Tube wave noise (direct and reflected) is shown in red.

4.5.3 Schlumberger Walkaway Processing

The walkaway data was processed by Schlumberger (

Figure 4.12). The walkaway VSP processing is different from zero-offset, and the following information has been adapted from the Schlumberger processing report. The horizontal components of the data were projected onto a vector in the direction of the source line. The angle of this vector was determined from hodogram analysis of particle motion in a window about the direct P arrival. This analysis is done for each receiver level to produce the in-line maximum horizontal component. The 9-34 well is vertical, so rotations were applied to the vertical plane. The Parametric Wavefield Decomposition method was used to separate the wavefields, and the NMO correction was used to display the upgoing wavefield in two-way time. From this point on, the zero-offset and walkaway deconvolved upgoing data will be used in two way time.
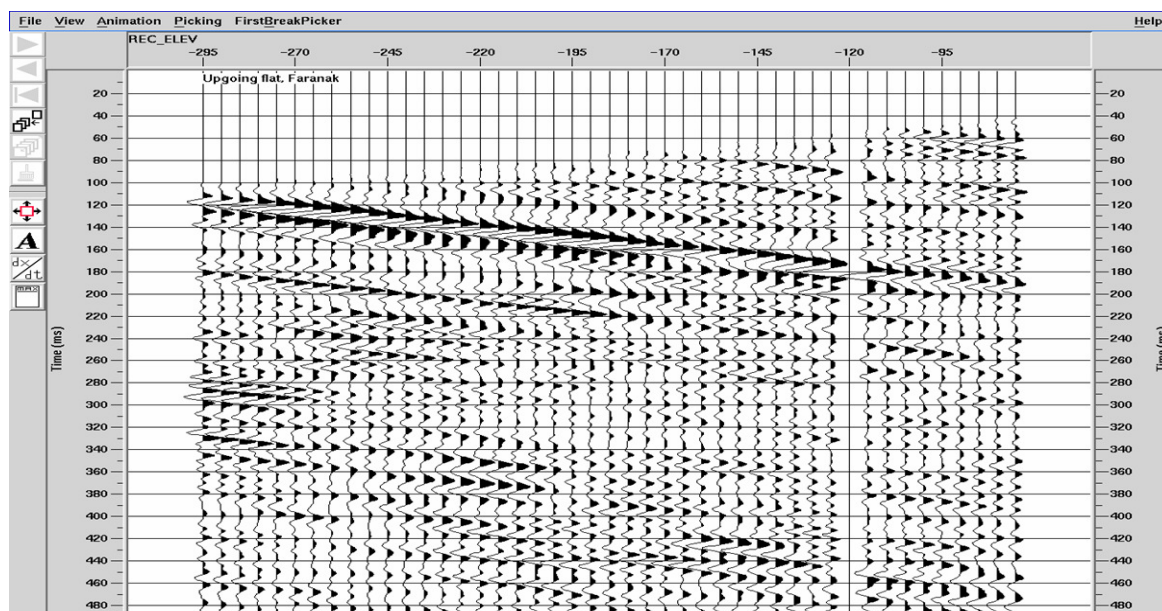
Figure 4.11: The deconvolved upgoing wavefield after application of the radial filter to suppress the tube waves present in the data, processed by ProMAX.

```
┌─────────────────────────────────┐
│       Geometry assignment       │
└─────────────────────────────────┘
                 │
                 ▼
┌─────────────────────────────────────────┐
│  Stack multiple shots by median algorithm │
└─────────────────────────────────────────┘
                 │
                 ▼
┌─────────────────────────────────────────┐
│     Rotation of horizontal components    │
└─────────────────────────────────────────┘
                 │
                 ▼
┌─────────────────────────────────┐
│        Pick first arrivals      │
└─────────────────────────────────┘
                 │
                 ▼
┌─────────────────────────────────────────┐
│      Temporal Amplitude Recovery        │
└─────────────────────────────────────────┘
                 │
                 ▼
┌─────────────────────────────────────────┐
│   Spatial Amplitude Normalization RMS   │
└─────────────────────────────────────────┘
                 │
                 ▼
┌─────────────────────────────────────────┐
│         Wavefield separation            │
└─────────────────────────────────────────┘
```

Downgoing PP
Downgoing PS

Upgoing PP
Upgoing PS

Design inverse filter

Median filter data enhancement

Waveshaping deconvolution

Median filter data enhancement

NMO correction

NMO corrected, deconvolved upgoing PP
NMO corrected, deconvolved upgoing PS

Figure 4.12: Processing flow used by Schlumberger to create NMO corrected deconvolved PP and PS walkaway data used in the AVO inversion (Courtesy of Richardson, 2003).

4.6 The Red Deer Walkaway PP and PS Data

Figure 4.13 and Figure 4.14 show the PP and PS data from the walkaway VSP in depth. The amplitude spectrum of a PP and a PS trace recorded at the deepest receiver for each walkaway offset shown in Figure 4.15. The amplitude spectrum indicates that the usable frequency content of the PP and PS data is similar in bandwidth to that of the Mini-P source (Figure 4.15), only the lowest and highest frequencies have been attenuated.
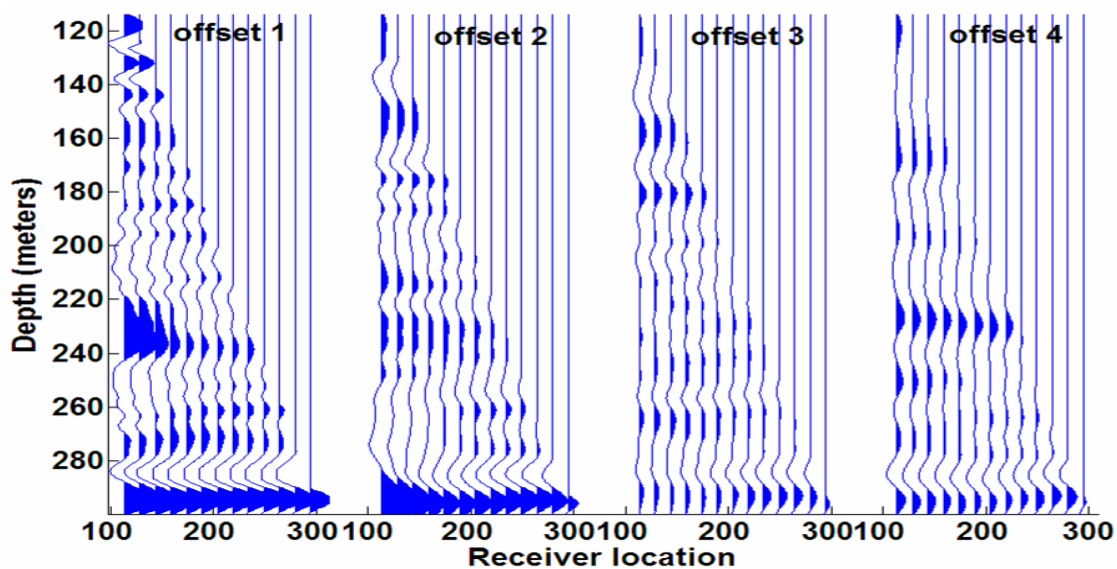
Figure 4.13: Deconvolved upgoing PP wavefield at the four walkaway offsets in depth.
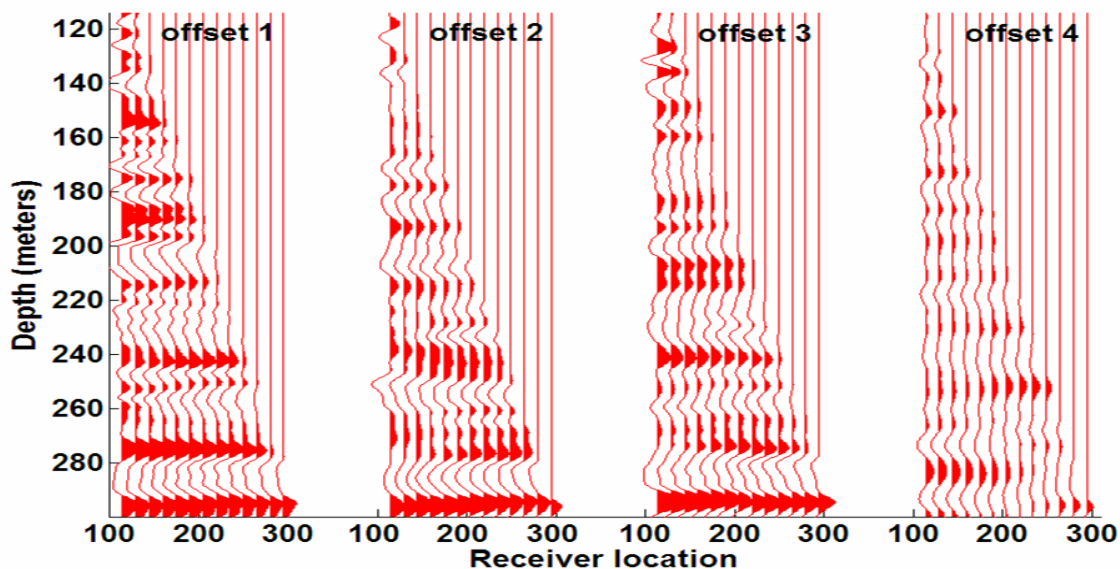
Figure 4.14: Deconvolved upgoing PS wavefield at the four walkaway offsets in depth.
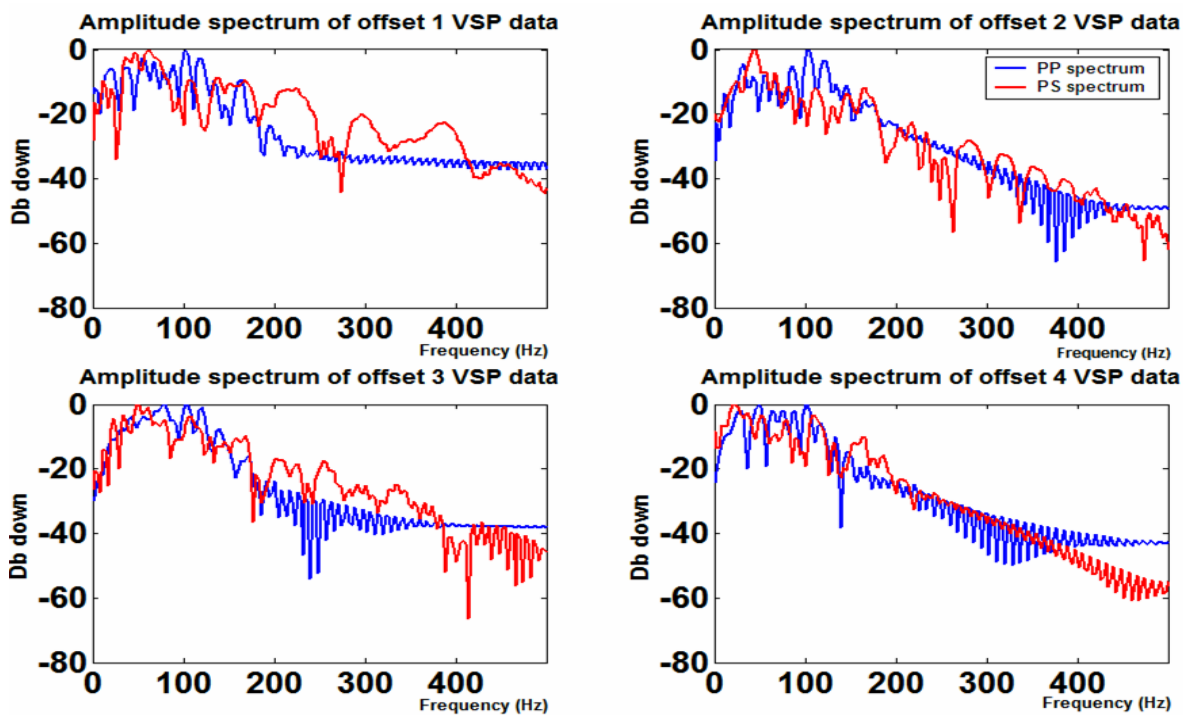
Figure 4.15: Amplitude spectra of the deepest trace of PP and PS data for all offset source locations. PP and PS spectra are shown in blue and red respectively.

4.7 PP and PS Polarity Check

Based on the discussion of Section 3.3.6, the polarity of the input PP and PS datasets prior to the AVO inversion was checked to ensure that it had the correct polarity. The following is an example of the polarity analysis for the walkaway offset 1 datasets. The I estimate from PP inversion correlates well to the I estimate from the well log, (Figure 4.16). However, there is no correlation between the J estimate from the PS inversion and the J estimate from well logs (Figure 4.17). Therefore, for the offset1 data the PS polarity is reversed. The PS inversion of reversed polarity shows a good correlation for the J estimate (Figure 4.18). Examining the PP and PS inversion for each individual walkaway offset data, the polarity of the PS data at offset 1 to offset 3 was reversed while the polarity of PP data from all walkaway offsets was intact. This completes the VSP data preparation for the AVO inversion. The next chapter discuses the AVO inversion of the Red Deer VSP data.
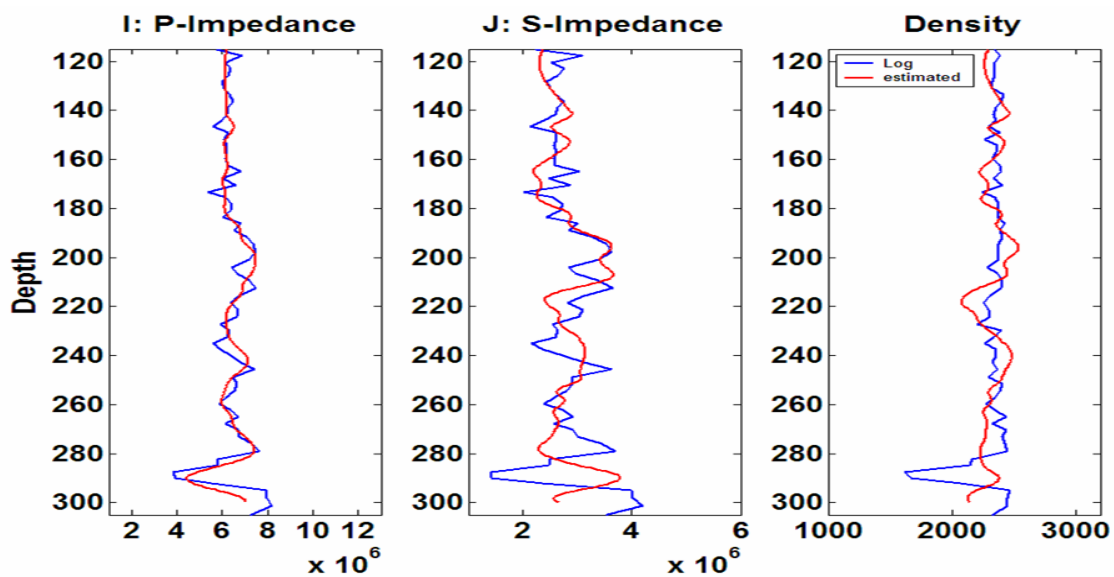
Figure 4.16: PP inversion of PP data from walkaway offset 1. Note that the *I* estimate (red) correlates well to the log estimate (blue).
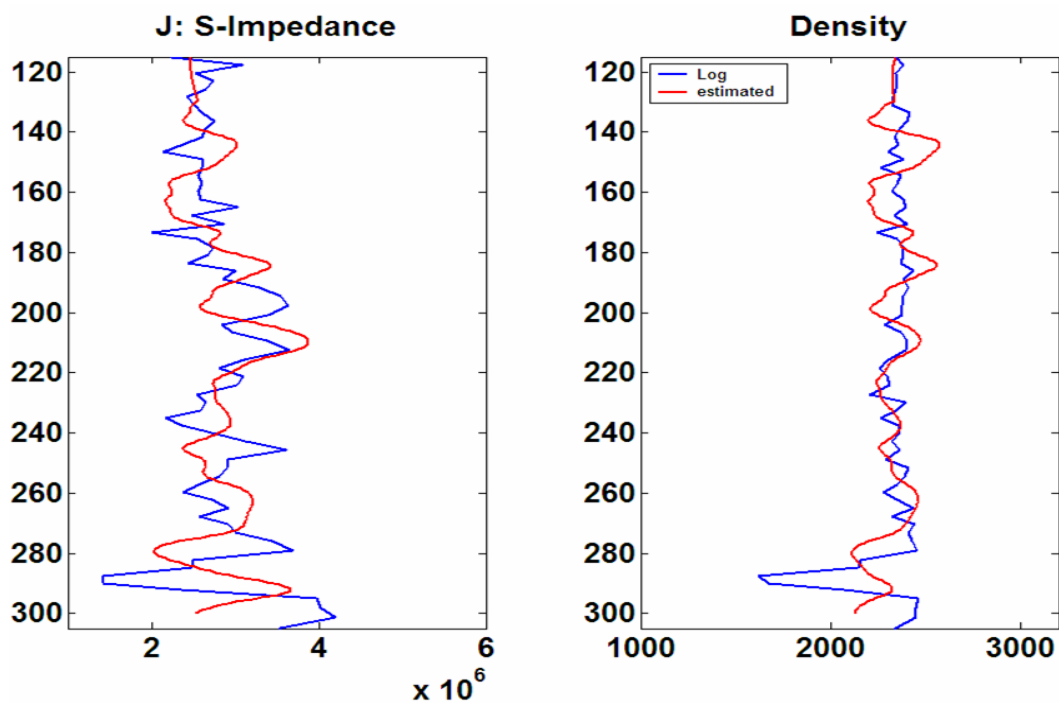
Figure 4.17: PS inversion estimates, for *J* and ρ, from the walkaway offset1 data. Note the *J* estimate (red) doesn't correlate to the log estimations (blue).
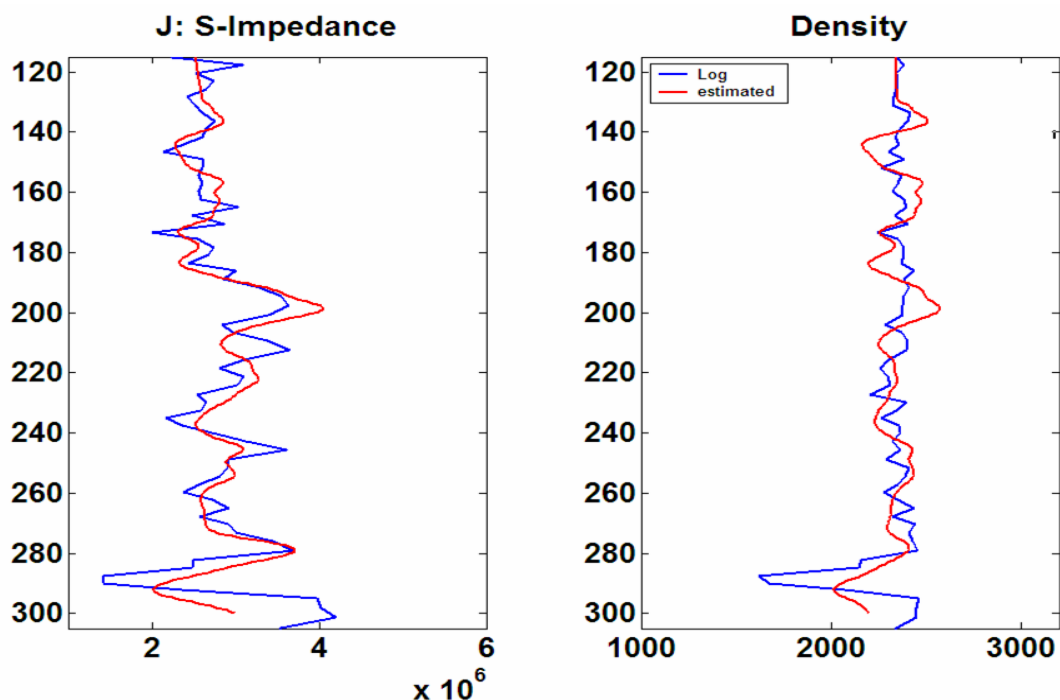
Figure 4.18: PS inversion estimates, for *J* and *ρ*, from reversed PS data of walkaway offset1. Note the *J* estimate (red) correlates well with the log estimations (blue).

4.8 Chapter Summary

The zero-offset vertical seismic profile and walkaway VSP obtained at the Red Deer study site were used in the AVO inversion. The VSPs obtained with the Mini-P source were re-processed prior to input to the AVO inversion; the processing flows for zero-offset and walkaway VSP by Schlumberger, and the VSP data reprocessed in ProMAX, were presented. The deconvolved upgoing wavefields in two way time from zero-offset to walkaway VSP were input to the AVO inversion. The polarity of the data was checked, and the amplitude spectra were examined before the AVO inversion. Some of the walkaway PS data had flipped polarities, thus the polarity had to be reversed.

CHAPTER 5: A Case Study of AVO Inversion using VSP Data,

5.1 Introduction

Chapters 2 and 3 outlined the joint AVO inversion (theory and testing) in which pre-stack PP and PS surface seismic data can be inverted to provide broadband estimates of compressional impedance, shear impedance and density. Chapter 4 presented the Red Deer study area and the processing flows for the VSP data prior to input to the joint AVO inversion. In this chapter, the 3-parameter joint AVO inversion is applied to the Red Deer VSP data. This procedure consists of several steps. The first is to modify the joint AVO inversion program for the VSP data. The second is the SVD analysis of the joint AVO inversion of the VSP data; the SVD analysis has shown that the joint AVO inversion of walkaway VSP data is ill-posed for most of the depths. The third is the application of the damping SVD method in stabilizing the ill-posed inversion.

Choosing a damping factor is a trial-and-error process. The best damping factor should optimize the resolution matrix and the error of the model parameter estimates. Application of SVD damping provides a reasonable estimate for the density, dependent on the two other parameters (the compressional and shear impedance). The investigation on the resolution matrix implies a Gardner's rule between the density and the S-wave

velocity for the study area. Also, the shear impedance and density estimates from inverting the converted shear wave data alone compared to the estimates from the joint inversion, shows comparable estimates.

5.2 Implementation of the AVO Inversion of VSP Data

Further development of the AVO inversion algorithm is required for the AVO inversion of the VSP data. The modifications affect the time-to-depth conversion and raytracing. The first-break times and the receiver depths were used to calculate the average velocity required for the time-depth conversion in the VSP data. The ray paths from the sources to the receivers at the borehole require a different raytracing than the surface seismic. The PP and PS raytracing for the VSP data used the Red Deer velocity log; this utilized the MATLAB routines TRACERAY-PP and TRACERAY-PS. At a particular depth, raytracing gives the incident and reflection angles for the receivers above a particular depth. For example, the PP and PS ray paths for the three selected reflector depths for the geometry of the walkaway offset 4, are illustrated in Figure 5.1. The PP and PS incident angle ranges from the raytracing of the Red Deer walkaway VSP, are given in Table 5.1.
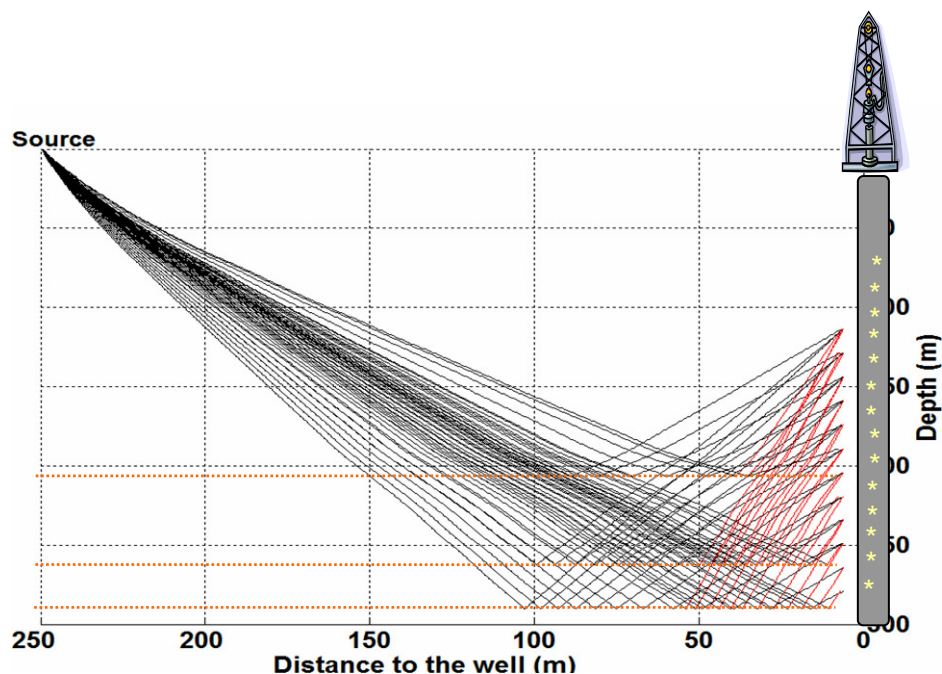
Figure 5.1: Ray paths assumed by the PP and PS raytracing of the Red Deer velocity model for the three selected depths. The black and red paths are the PP and PS ray paths respectively.

Table 5.1: The PP and PS incident angle ranges for the three selected depths from the walkaway VSP.

depth (m)	Walkaway offset 1		Walkaway offset 2		Walkaway offset 3		Walkaway offset 4	
	PP incident angle°	PS incident angle°	PP incident angle°	PS incident angle°	PP incident angle°	PS incident angle°	PP incident angle°	PS incident angle°
206	19°-30°	25°-30°	27°-43°	35°-43°	35°-52°	45°-52°	45°-55°	55°-56°
262	12°-20°	16°-21°	18°-29°	24°-30°	23°-35°	30°-36°	30°-42°	38°-43°
290	10°-17°	14°-18°	15°-25°	20°-25°	19°-30°	25°-31°	25°-36°	32°-37°

The amplitude scaling (Chapter 3) and restoration of the low frequency trend (Chapter 2) in the VSP AVO inversion are identical to the methodology used for the surface seismic AVO inversion. The impedance and density estimates, calculated from the Red Deer well logs, are used to restore the missing low frequency trend. The cutoff low frequency for the *I* estimate is shown in Figure 5.2. It indicates that only a small portion of the frequency band-width is from the well logs. This completes the details of the VSP AVO inversion implementation. The next section will provide an analysis of the singularity of the AVO inversion of the walkaway VSP.
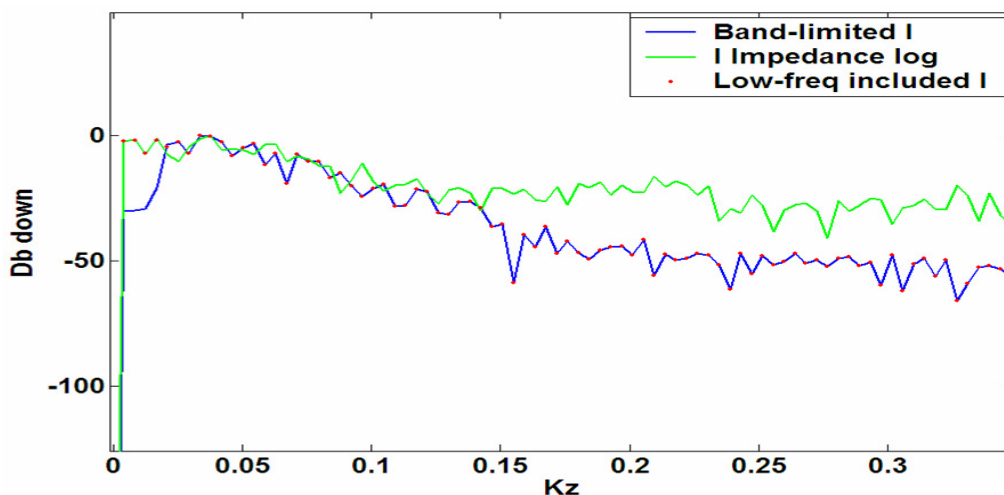
Figure 5.2: Amplitude spectra of the *I* (band-limited) estimate. The blue curve is the band-limited *I*, the green curve is the impedance from the well logs, and the red dots are the *I* estimate after restoring the low frequency trend.

5.3 SVD Analysis

The condition number plots of the 3-parameter PP, joint inversion, and the PS inversion (for *J* and ρ) of the Red Deer walkaway data are shown in Figure 5.3 - Figure 5.5. In these Figures, the condition number plot for the depths smaller than 210 m, is not

displayed, because for the further offsets data (especially for walkaway offset 4) the incident angle passes the critical angle and causes a very unstable inversion; in addition, the zone of interest, the Ardley coal zone, is below this range.

Examination of Figure 5.3-Figure 5.5, leads to the following observations:

1. The high condition number (being far from one, see section 2.4) indicates that the AVO inversions are ill-posed for most of the depths, especially for the Ardley coal zone (at a depth of 284-300 m). Therefore, none of the three inversions could result in favourable model parameter estimates, at least for the third parameter.

2. The very large condition numbers from the 3-parameter PP inversion (Figure 5.5) suggest that inverting the PP data alone may not result in the good estimates for all three parameters.

3. The 3-parameter joint inversion (Figure 5.3) have smaller condition numbers compared to the PP inversion (Figure 5.5), might further underlining the advantage of the application of the joint inversion over the inversion of compressional data alone.

4. There is a decreasing trend in the condition number values, from the AVO inversions (Figure 5.3-Figure 5.5) of the walkaway offset 1 to the walkaway offset 4. This suggests that better estimates might be achieved from the inversion of the larger offset data.

5. The PS inversion (for J and ρ) has smaller condition numbers (Figure 5.4) than the 3-parameter joint inversion (Figure 5.3), which might result in better or comparable parameter estimates, similar to what was observed with the synthetic

data in Chapter 3.
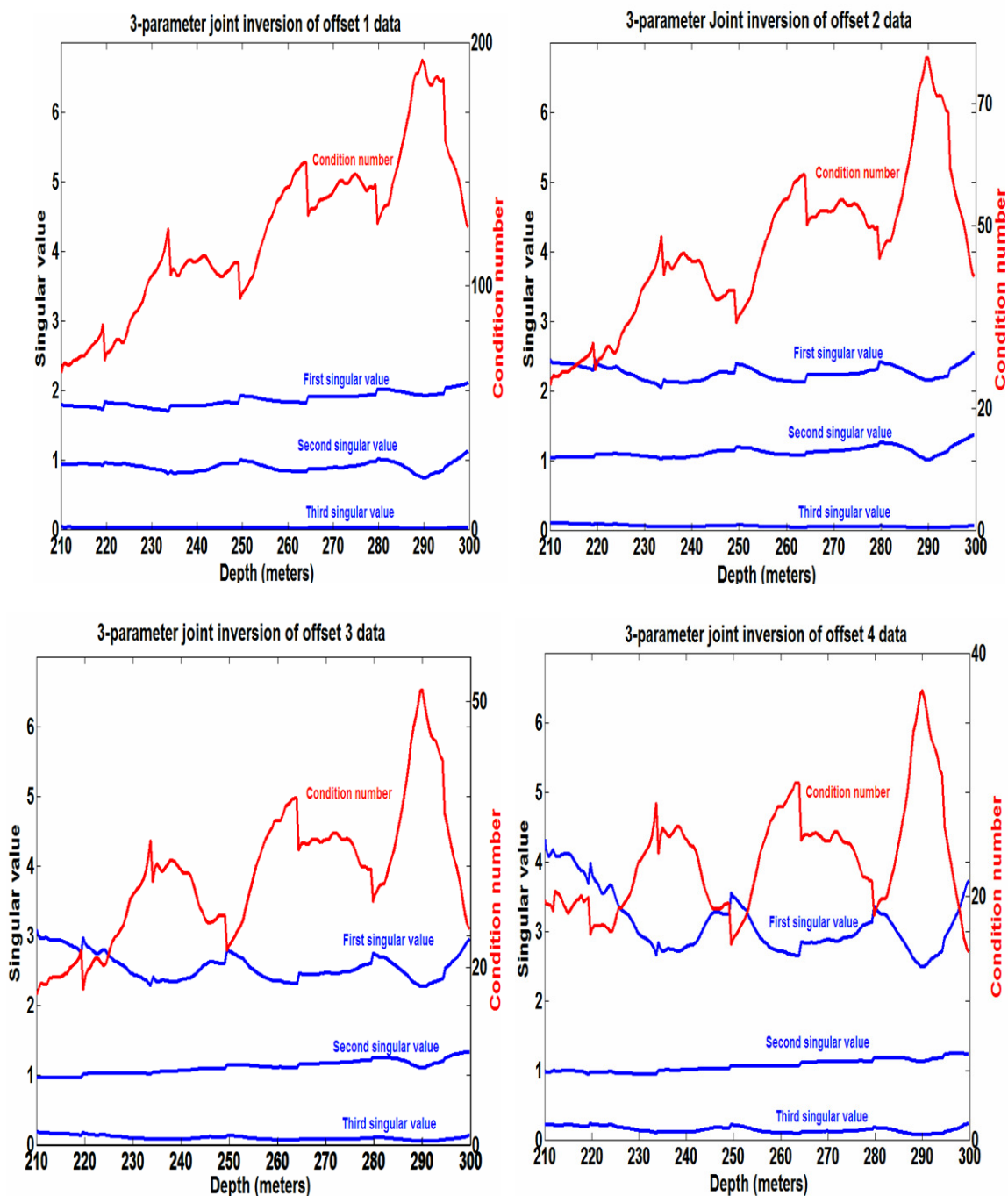
Figure 5.3: The singular value (in blue) and the condition number (in red) versus depth from the 3-parameter joint inversion of walkaway offset 1(upper left), offset 2 (upper right), offset 3 (bottom left), and offset 4 (bottom right).
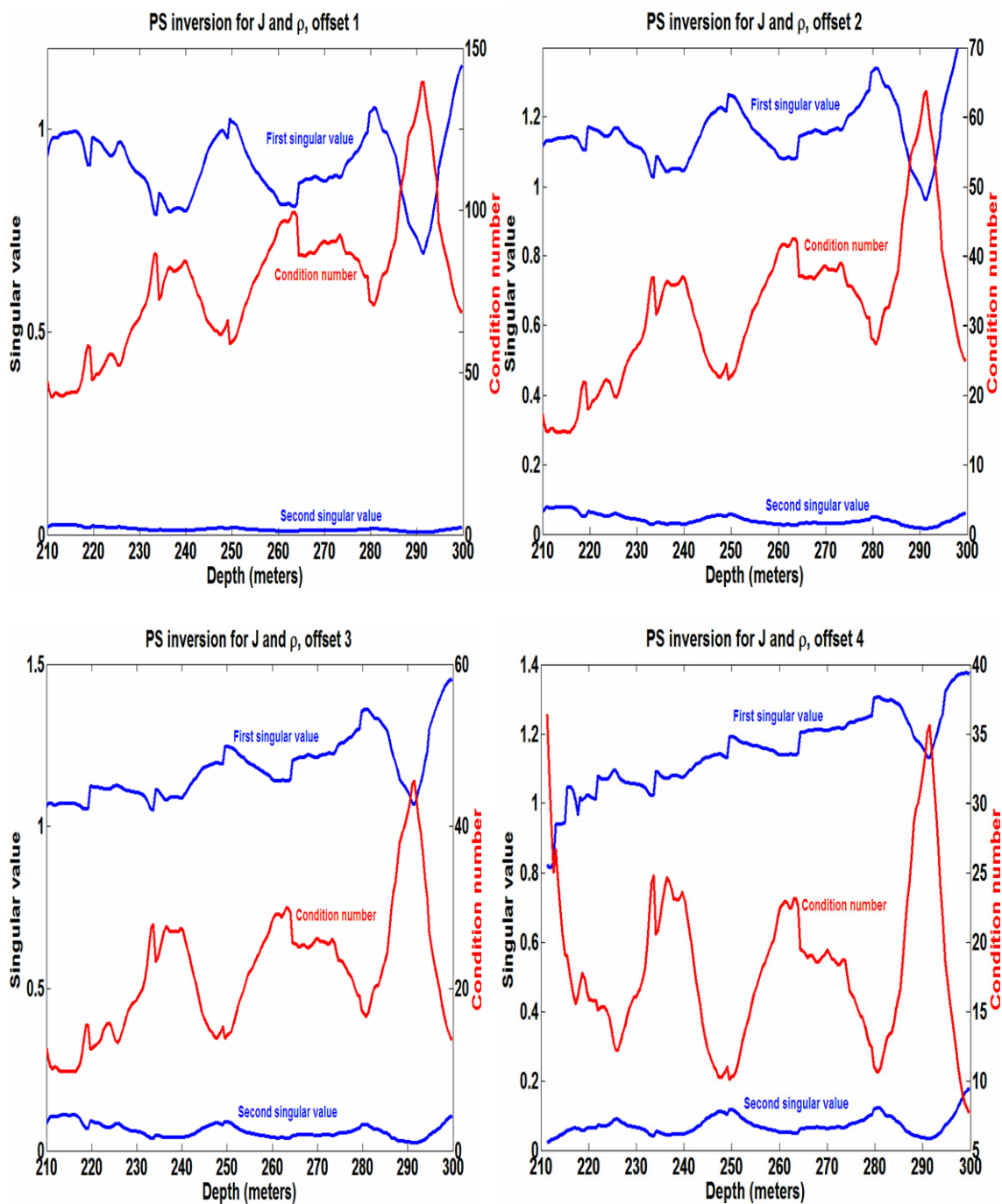
Figure 5.4: The singular values (in blue) and the condition number (in red) versus depth from the PS joint inversion of walkaway offset 1(upper left), offset 2 (upper right), offset 3(bottom left), and offset 4 (bottom right).
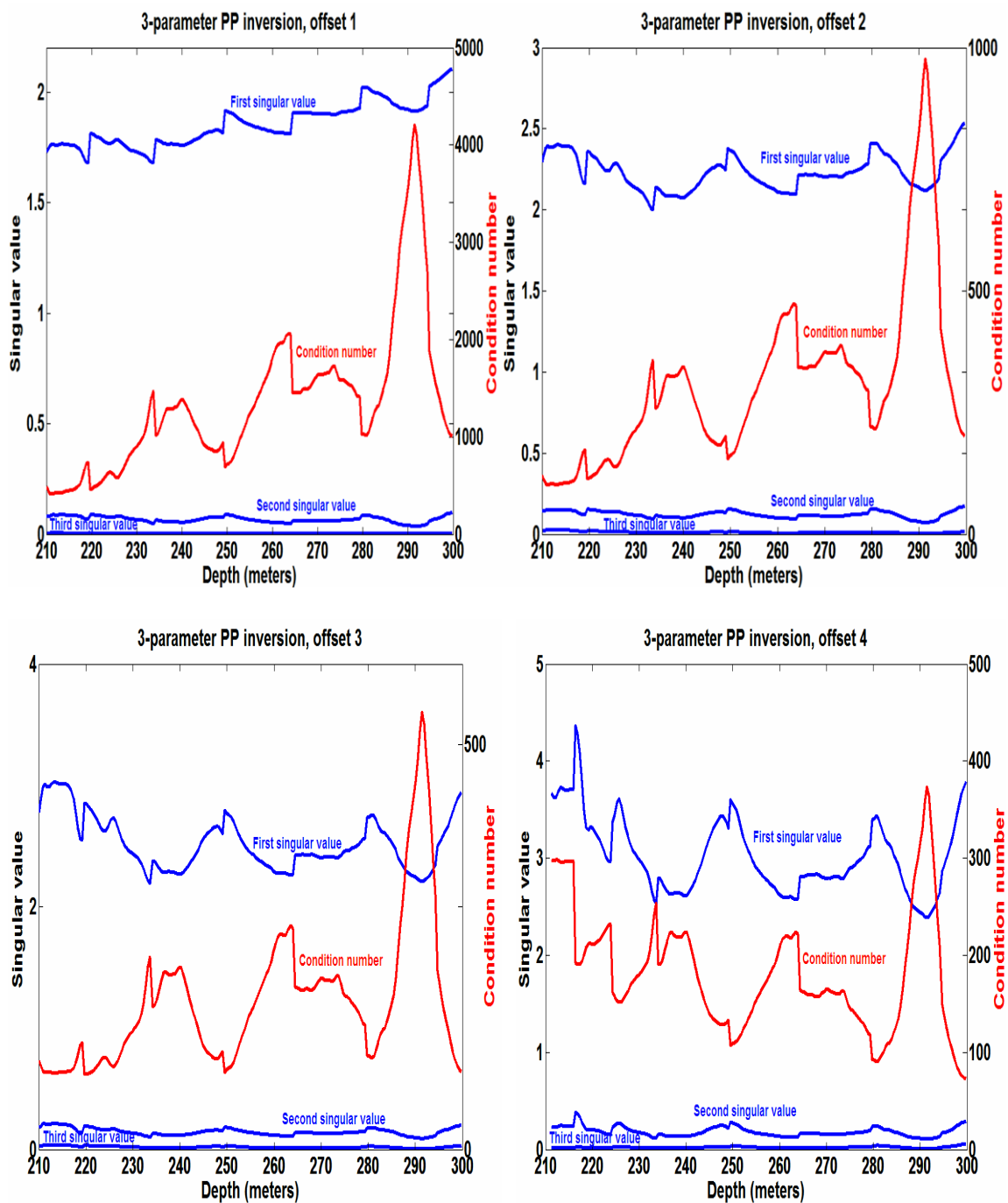
Figure 5.5: The singular values (in blue) and the condition number (in red) versus depth from the 3-parameter PP inversion of walkaway offset 1(upper left), offset 2 (upper right), offset 3(bottom left), and offset 4 (bottom right).

To examine the accuracy of the above observations, the plots of the *I*, *J* and ρ estimates from the AVO inversions of walkaway offset 1 and offset 4 data are shown in Figure 5.6 and Figure 5.7. These Figures confirm the mentioned observations as follow:

- None of the three PP, PS and joint inversions can provide a good estimate for the density especially at the Ardley coal zone, confirming that the ill-posed inversions will not result in a good estimate, at least for the density (statement 1).

- The PP inversion estimates are not desirable (statement 2).

- The PP inversion does not provide as good estimates as the joint inversion (statement 3).

- Better estimates are produced by the inversions of the offset 4 data, compared to the estimates from the inversions of offset 1 data (statement 4).

- The PS inversion provides similar estimates for the *J* and ρ, compared to the joint inversion (statement 5).

Figure 5.6 - Figure 5.7 shows that even for the best survey geometry (walkaway offset 4) none of the three inversions provides a good estimate for the density. Aiming for a good density estimate, the damped SVD will be used as a last resort.
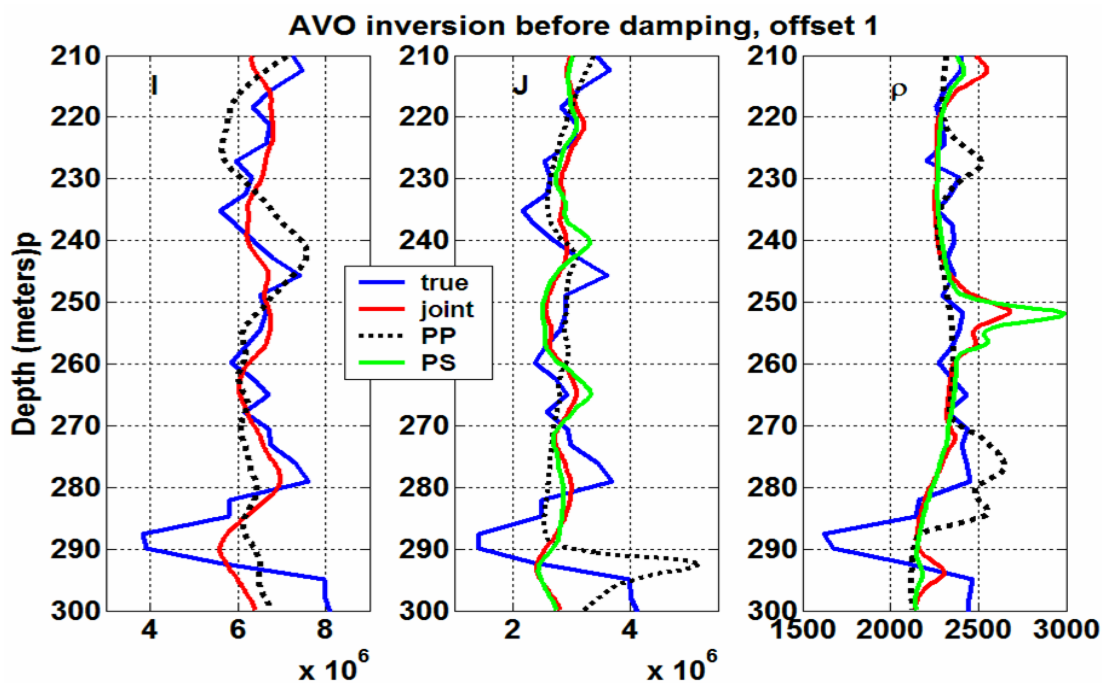
Figure 5.6: The P-impedance: *I*, S-impedance: *J*, and density: ρ from the 3-parameter PP and joint inversion and the PS inversion (for *J* and ρ) of walkaway offset 1.
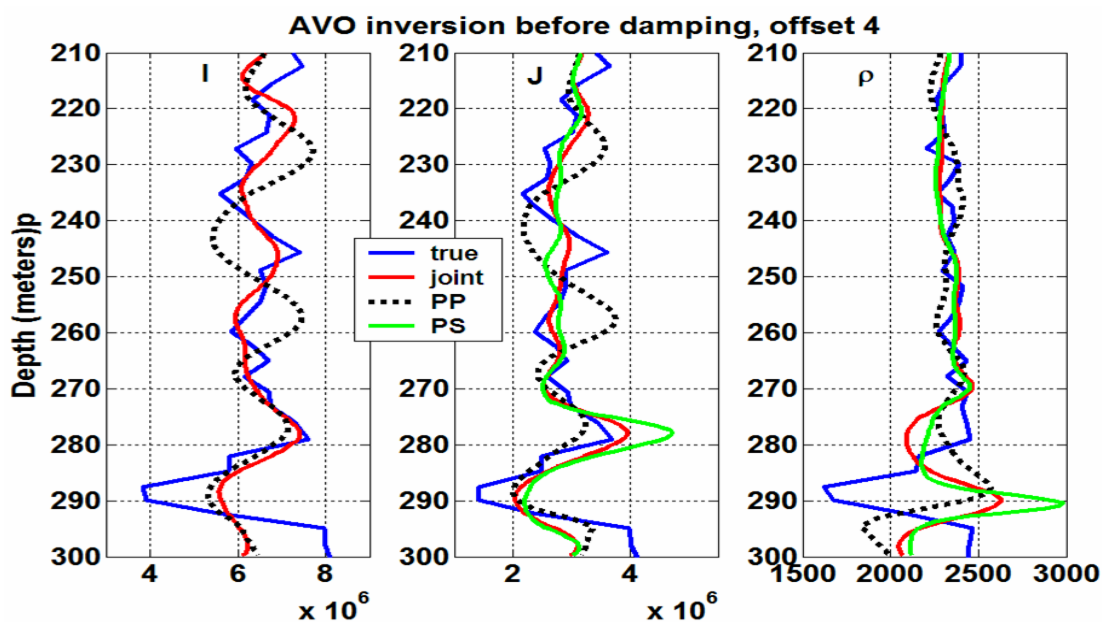
Figure 5.7: The P-impedance: *I*, S-impedance: *J*, and density: ρ from the 3-parameter PP and joint inversion and the PS inversion (for *J* and ρ) of walkaway offset 4.

5.3.1 Damped SVD

The damped SVD method consists of adding a small percentage, ε percent, of the largest singular value to the smaller singular values (as in Equation (2.37)). The damping factor contributes to the stability of the inversion by suppressing the effect of small singular values. To examine the damping factor effect on the AVO inversion estimates, a damping factor, ε, varying from 0 to 9 percent is applied to the 3-parameter joint inversion of the walkaway offset 3 data; the ε equal to zero case yields the undamped estimates (Figure 5.8 -Figure 5.10). The damping factor is not kept constant throughout the inversion procedure versus depth.
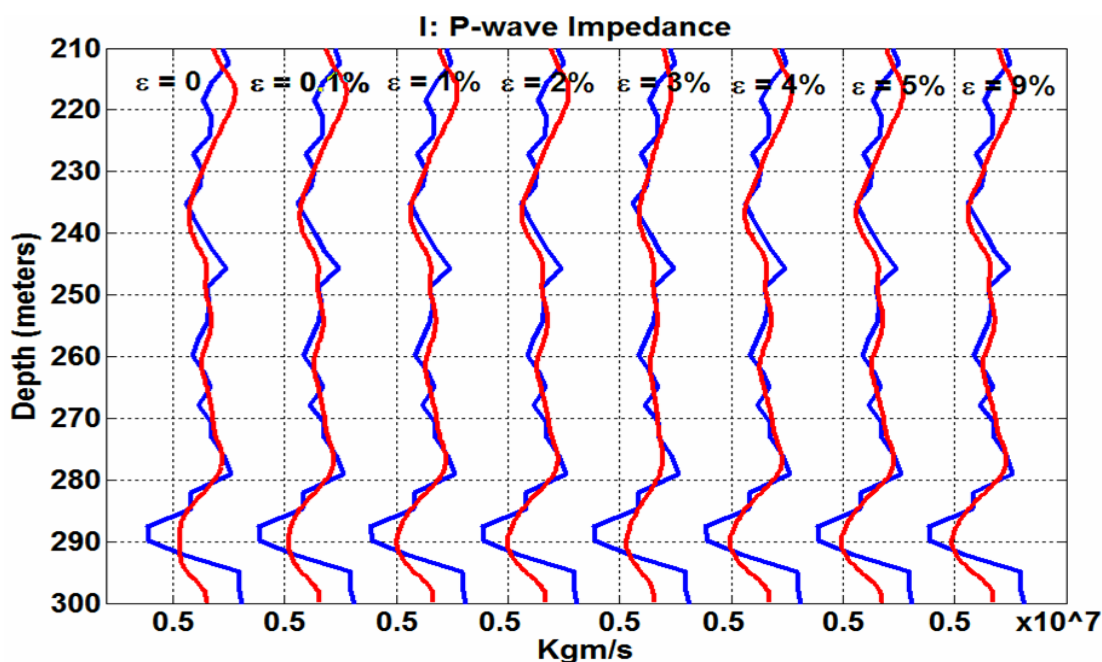
Figure 5.8: The P-impedance estimate from the 3-parameter joint inversion of walkaway offset 3, with various SVD damping factors. The blue curves are values from the well logs, and the red curves the estimates from the joint inversion. ε varies from 0 to 9 percent from left to right.

J: S-wave Impedance
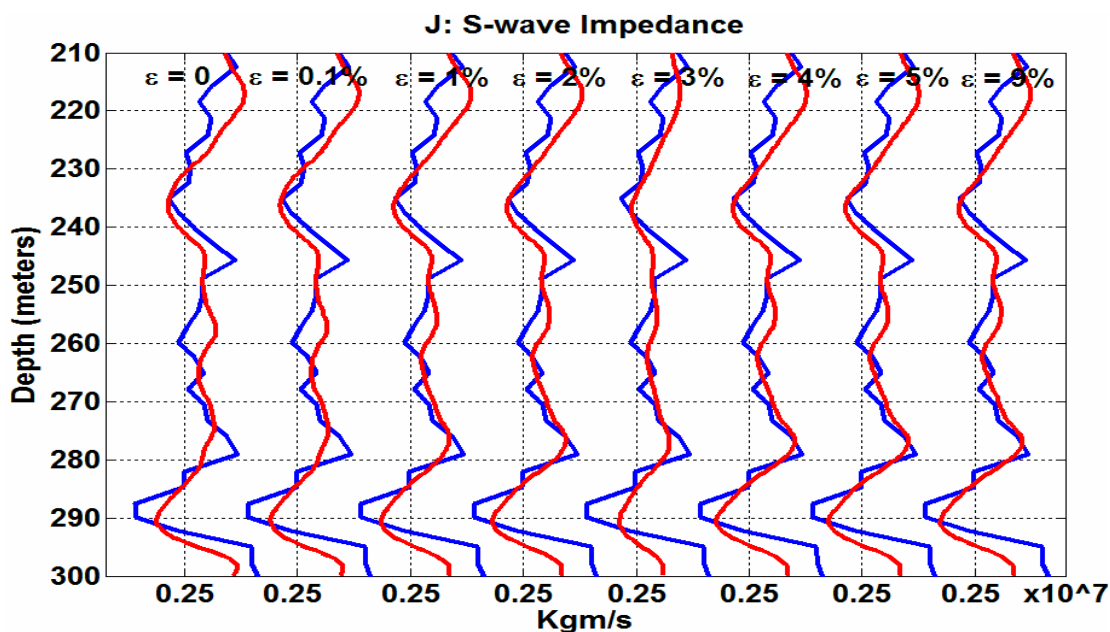
Figure 5.9: The S-impedance estimate from the 3-parameter joint inversion of walkaway offset 3, with various SVD damping factors. The blue curves are value from the well logs, and the red curves are estimates from the joint inversion. ε varies from 0 to 9 percent from left to right.
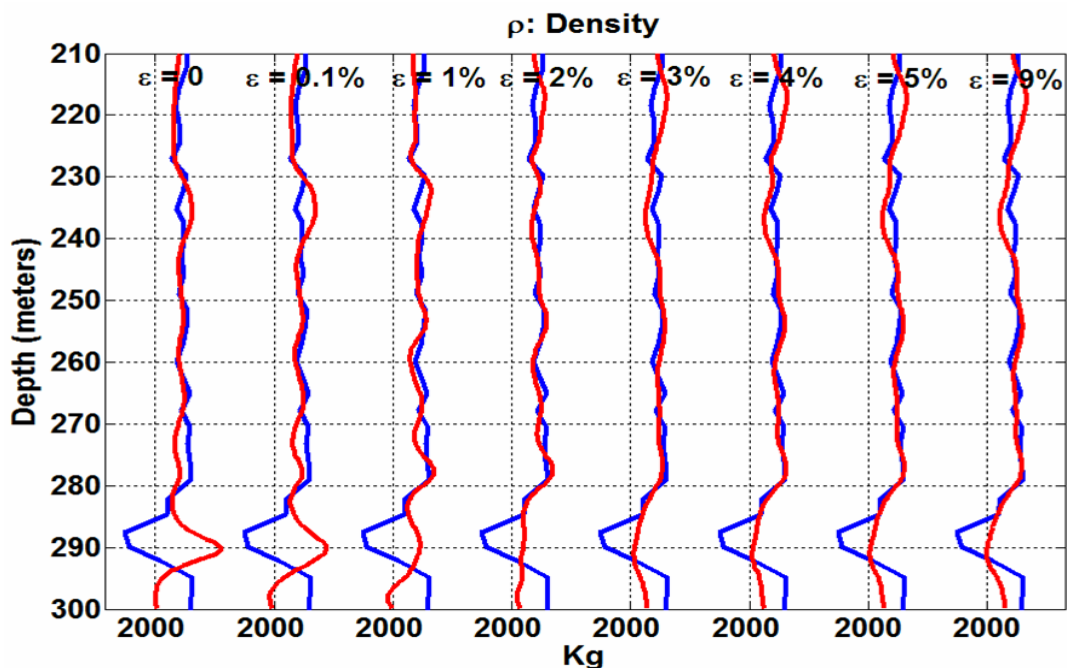
ρ: Density

Figure 5.10: The density estimate from the 3-parameter joint inversion of walkaway offset 3, with various SVD damping factors. The blue curves are values from the well logs, and the red curves are estimates from the joint inversion. ε varies from 0 to 9 percent from left to right.

The relative errors of the model parameters estimates, for various ε, are shown in Figure 5.11-Figure 5.13. The relative error is calculated by comparing the estimates to the true values calculated from the Red Deer well logs. Figure 5.10 and Figure 5.13 show that the error of the ρ estimate has been lowered by the SVD damping, especially at the Ardley coal zone.
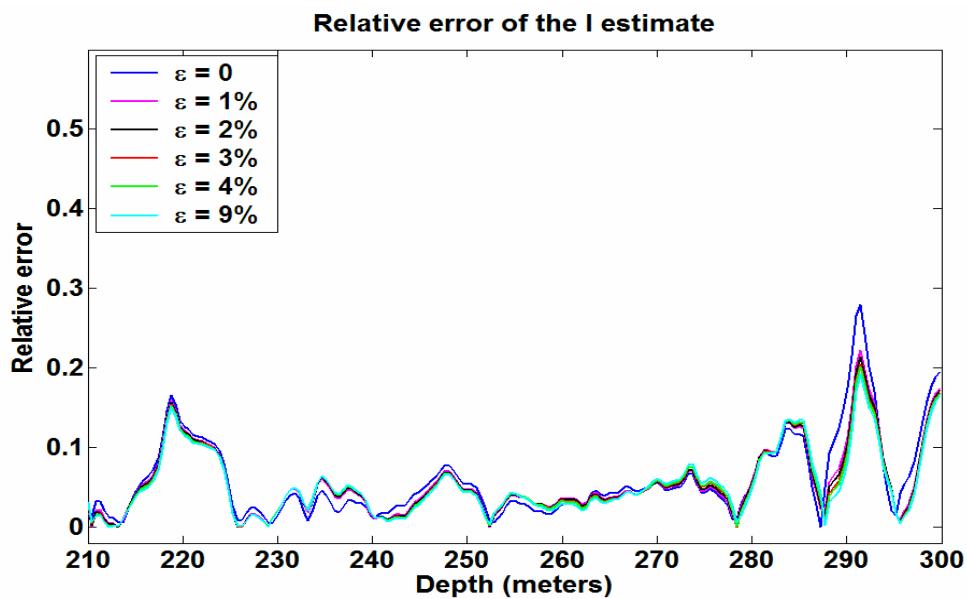
Figure 5.11: the relative error of the *I*: P-impedance estimate versus depth, for the various damping factors ε, from the 3-parameter joint inversion of walkaway offset3 data.
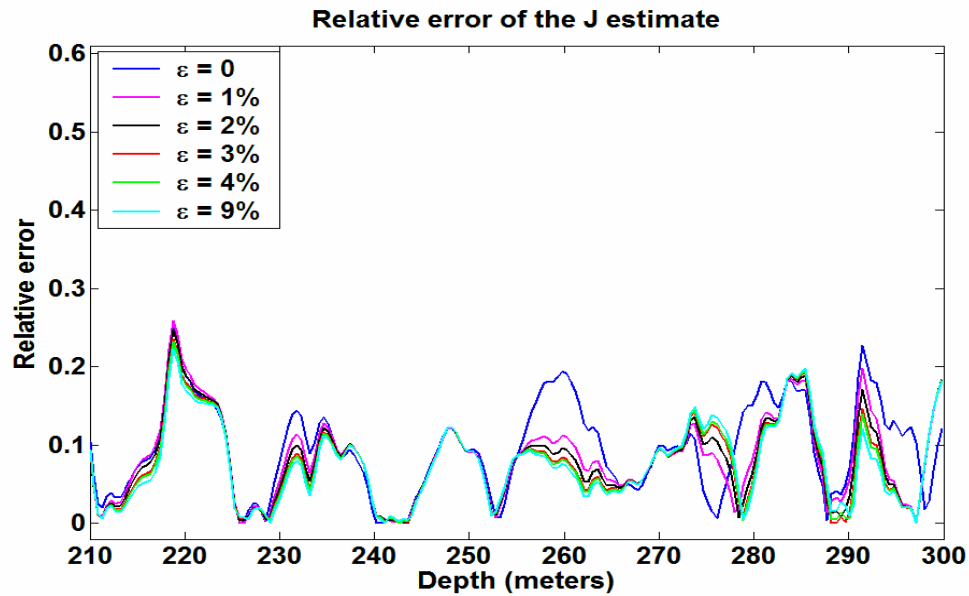
Figure 5.12: The relative error of the *J*: S-impedance estimate versus depth, for the various damping factors ε, from the 3-parameter joint inversion of walkaway offset3 data.
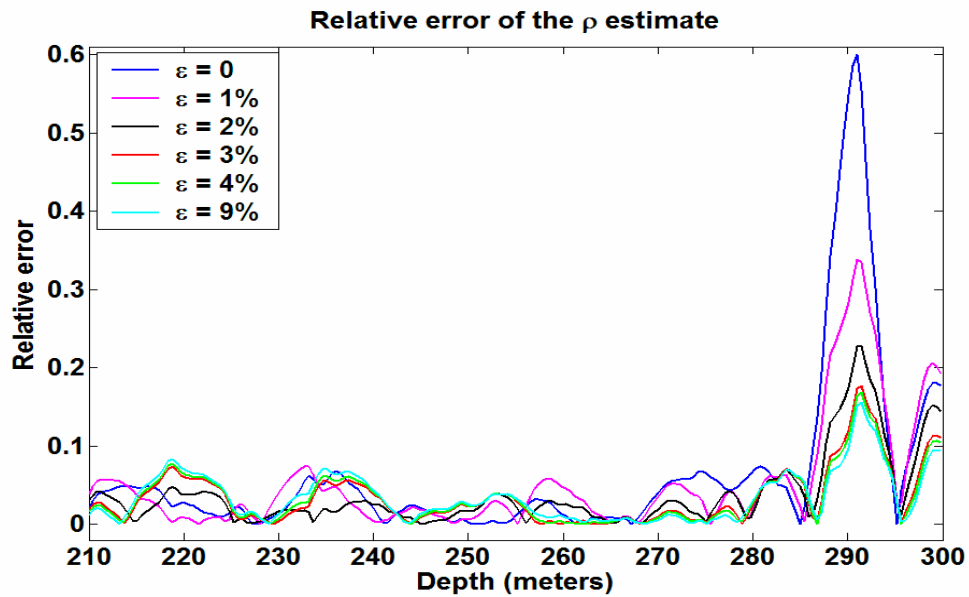
Figure 5.13: The relative error of the *ρ*: density estimate versus depth, for the various damping factors ε, from the 3-parameter joint inversion of walkaway offset3 data.

The precise value of the damping factor must be chosen by a trial-and-error process which weighs the relative merits of having a solution with small errors against those that are well resolved. There is a corresponding decrease in resolution with a decrease in error of the estimates. Ultimately, the model resolution matrix needs to be examined.

The resolution matrix defines how well the estimated solutions resolve the true solutions (Section 2.4). As in Equation 2.34, the model resolution matrix $G^{-1}G$ is derived from:

$$m^{est} = G_g^{-1}d \cong (G_g^{-1}G)m. \tag{5.1}$$

For our AVO inversion problem the resolution matrix is a 3×3 matrix of r_{ij}, then the estimates can be calculated as:

$$
\begin{bmatrix}
\dfrac{\Delta I}{I}^{est} \\[2mm]
\dfrac{\Delta J}{J}^{est} \\[2mm]
\dfrac{\Delta\rho}{\rho}^{est}
\end{bmatrix}
=
\begin{bmatrix}
r_{11} & r_{12} & r_{13} \\
r_{21} & r_{22} & r_{23} \\
r_{31} & r_{32} & r_{33}
\end{bmatrix}
\begin{bmatrix}
\dfrac{\Delta I}{I}^{true} \\[2mm]
\dfrac{\Delta J}{J}^{true} \\[2mm]
\dfrac{\Delta\rho}{\rho}^{true}
\end{bmatrix}
\tag{5.2}
$$

$$
\begin{cases}
\dfrac{\Delta I}{I}^{est} = r_{11}\dfrac{\Delta I}{I}^{true} + r_{21}\dfrac{\Delta J}{J}^{ture} + r_{13}\dfrac{\Delta\rho}{\rho}^{true} \\[4mm]
\dfrac{\Delta J}{J}^{est} = r_{21}\dfrac{\Delta I}{I}^{true} + r_{22}\dfrac{\Delta J}{J}^{ture} + r_{23}\dfrac{\Delta\rho}{\rho}^{ture} \\[4mm]
\dfrac{\Delta\rho}{\rho}^{est} = r_{31}\dfrac{\Delta I}{I}^{true} + r_{32}\dfrac{\Delta J}{J}^{ture} + r_{33}\dfrac{\Delta\rho}{\rho}^{ture}
\end{cases}
\tag{5.3}
$$

Figure 5.14 shows the rows of the resolution matrix from the joint inversion of walkaway offset 3 data at the Ardley coal top at 284 m, with different damping factors. The rows of the resolution matrix relate to the coefficients of the I, J and ρ estimates, as in Equation (5.3), respectively. For a perfect resolution, the resolution matrix should be an identity matrix, which means each parameter is estimated independently from the others; for the case of $\varepsilon = 0$ the resolution matrix is identity (Figure 5.14). By increasing the damping factor the resolution matrix will deviate more from the identity matrix and the less resolution is achieved (Figure 5.14). Table 5.2 shows the numerical values of the resolution matrix from the joint inversion of the walkaway offset 3 data at the Ardley coal top; using the SVD damping method the ρ estimate is determined dependent on the I and J estimates.

Table 5.2: The resolution matrix from the joint inversion of walkaway offset 3 data, with various damping factors, at the Ardley top, depth equal to 284 m.

$\varepsilon = 0$				$\varepsilon = \%0.1$				$\varepsilon = \%1$				$\varepsilon = \%2$		
1	0	0		0.0994	-0.0013	0.0022		0.9939	-0.007	0.0052		0.9879	-0.0018	0.0044
0	1	0		-0.0013	0.9691	0.0852		-0.007	0.9024	0.2404		-0.0118	0.8801	0.2642
0	0	1		0.0022	0.0852	0.7521		0.0052	0.2404	0.2898		0.0044	0.2642	0.2066
$\varepsilon = \%3$				$\varepsilon = \%4$				$\varepsilon = \%5$				$\varepsilon = \%9$		
0.9821	0.0162	0.0031		0.9764	-0.0204	0.0018		0.9708	-0.0244	0.0005		0.9493	0.0388	0.0095
0.0162	0.8642	0.2709		-0.0204	0.8504	0.2725		-0.0244	0.8377	0.2721		0.0388	0.793	0.2639
0.0031	0.2709	0.1735		0.0018	0.2725	0.1553		0.0005	0.2721	0.1436		0.0095	0.2639	0.1193

The resolution matrices (Table 5.2) show that the ρ estimate is more dependent on the J estimate than the I estimate. However, by increasing the damping factor the density error is reduced (Figure 5.10 and Figure 5.13). There is always a tradeoff between resolution and errors in the kth model parameter estimate. The selected damping factor should optimize the resolution matrix and the error estimates.

To decide about the damping factor, the maximum correlation between the estimates and the true model parameters is examined. The maximum correlation plots (Figure 5.15) shows the dramatic change in the ρ estimate when using a damping factor. The large maximum correlation value (Figure 5.15) and the small relative error of the ρ estimate (Figure 5.13) are due predominantly to the low magnitude of the undamped ($\varepsilon = 0$) ρ estimate error (Figure 5.16).
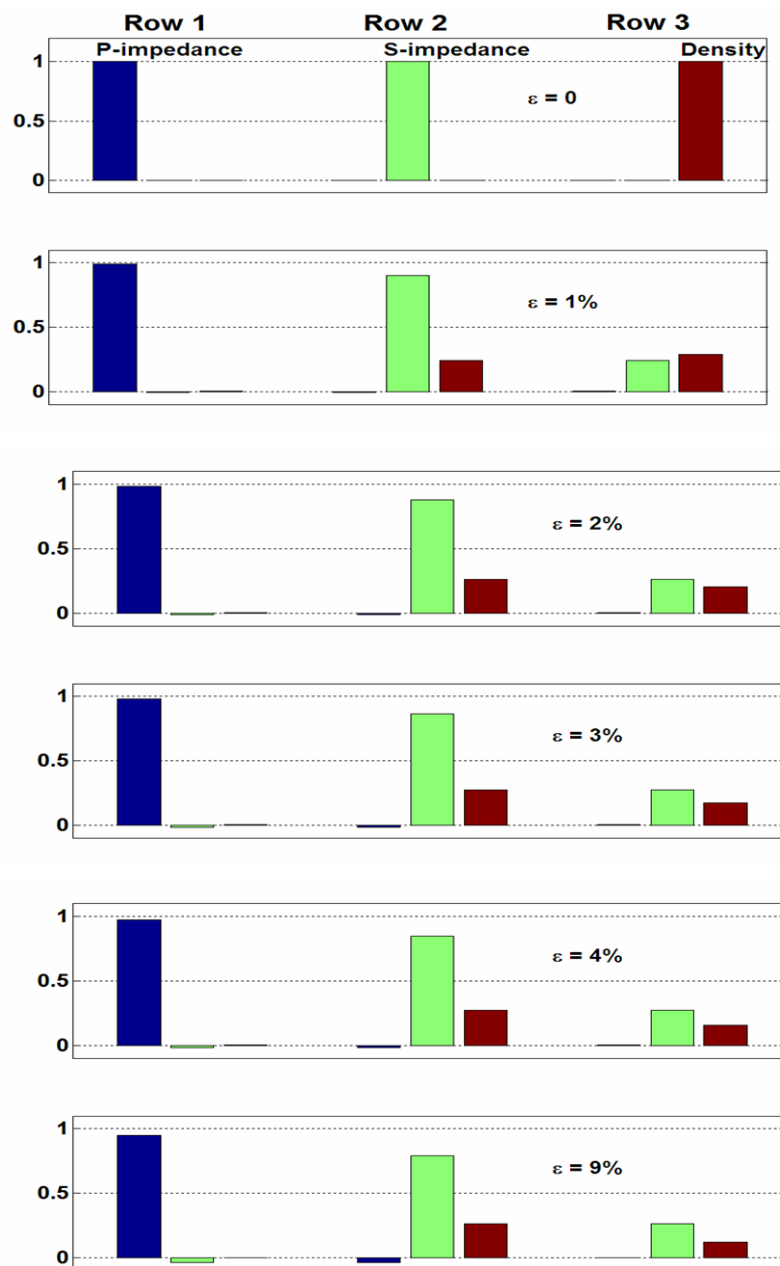
Figure 5.14: The rows of the resolution matrix from the joint inversion of walkaway offset3 data, at the Ardley top at 284 m. Each plot shows the resolution matrix with a different damping factor ε.
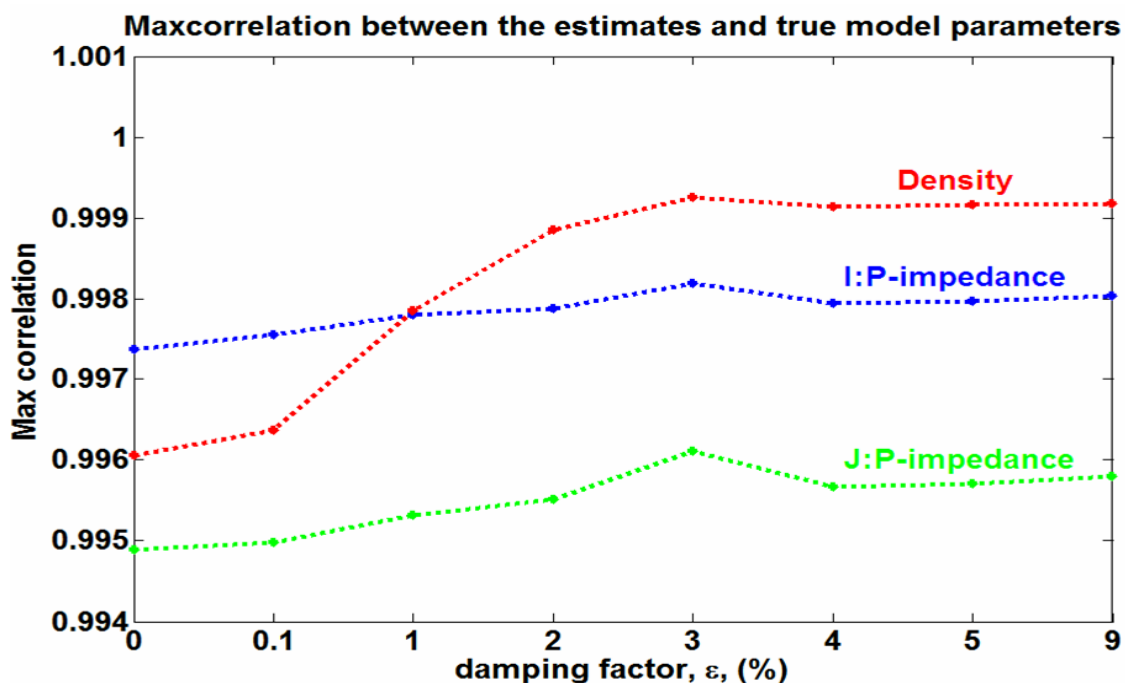
Figure 5.15: The maximum correlation of the joint inversion estimates of walkaway offset 3 data for various ε.

The maximum correlation investigation suggests that a damping factor equal to 3% has the best correlation between the model parameter estimates and the true values (Figure 5.15), although, the higher damping factor results have smaller relative errors (Figure 5.13). At this value $(\varepsilon = 3\%)$, the accuracy gain, compared to the larger damping factor estimates, becomes minimal (Figure 5.13) and the resolvability of the model parameters, although still decreasing, is similar to the resolution provided by the larger damping factor (Figure 5.14). Therefore, the damping factor of 3% is chosen for stabilizing the AVO inversions of Red Deer VSP data.
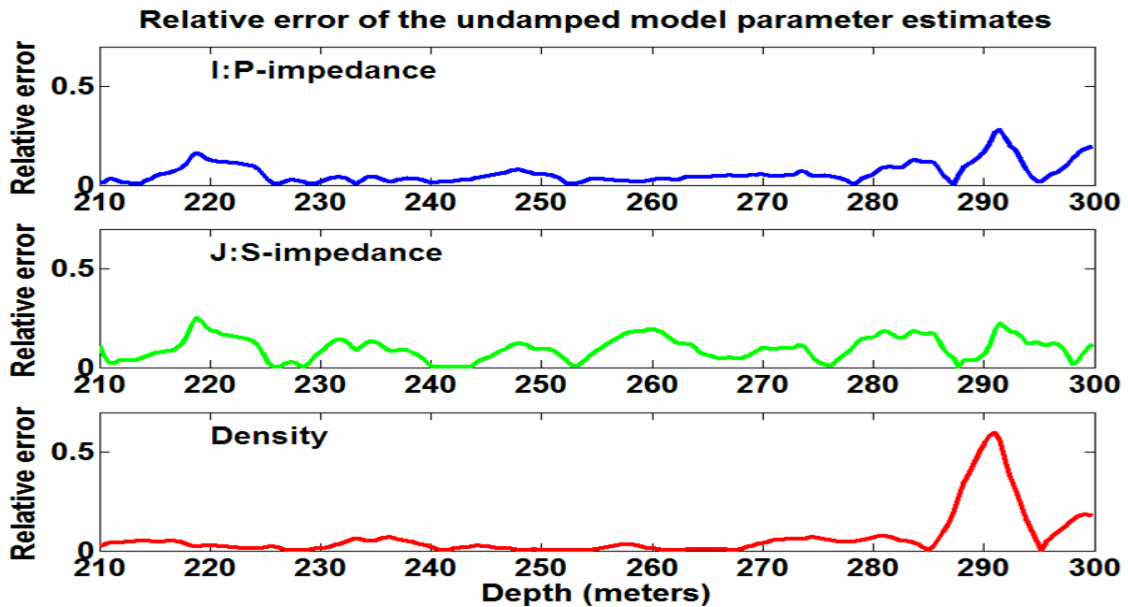
Figure 5.16: The relative error of the unstable joint inversion estimates versus depth ($\varepsilon = 0$), for walkaway offset3 data.

The relative error plots (Figure 5.11-Figure 5.12-Figure 5.13) show that the two estimates (I and J) are not much affected by the SVD damping, while the error of the density estimate has been lowered by the SVD damping. Also, the maximum correlation plots (Figure 5.15) show that there are not dramatic changes in the I and J estimates for different ε; while there is a dramatic change in the ρ estimate when using a damping factor (Figure 5.13 -Figure 5.15). By increasing the damping factor, less resolution for the J and ρ estimates is achieved, however, the resolution of the I estimate is not affected by the use of a damping factor (Figure 5.14). Therefore, the AVO inversion of Red Deer VSP data is a strongly stable problem for the I estimate, a less stable problem for the J estimate, and it is an unstable inversion for the ρ estimate.

Table 5.3: The resolution matrix from the joint inversion of walkaway offset 3 data with damping factor of 3%, at different depths.

depth = 208 m				depth = 257 m		
0.806	-0.1794	0.0665		0.8523	-0.0776	-0.0442
-0.1794	0.3265	0.278		-0.0776	0.5792	0.225
-0.0665	0.278	0.3154		-0.0442	0.225	0.0951
depth = 215 m				depth = 264 m		
0.8034	-0.1837	-0.0445		0.858	-0.0723	-0.0458
-0.1837	0.3661	0.2815		-0.0723	0.5902	0.2213
-0.0445	0.2815	0.2749		-0.0458	0.2213	0.0915
depth = 222 m				depth = 271 m		
0.8266	-0.1351	-0.0514		0.8568	-0.0758	-0.0375
-0.1351	0.449	0.2796		-0.0758	0.6024	0.2178
-0.0514	0.2796	0.2047		-0.0375	0.2178	0.0869
depth = 229 m				depth = 278 m		
0.8346	-0.1075	-0.0492		0.8503	-0.095	-0.0185
-0.1075	0.5081	0.2578		-0.095	0.6111	0.2271
-0.0492	0.2578	0.1437		-0.0185	0.2271	0.0949
depth = 236 m				depth = 285 m		
0.848	-0.0772	-0.0615		0.8606	-0.0735	-0.0306
-0.0772	0.5343	0.2423		-0.0735	0.6283	0.2005
-0.0615	0.2423	0.1202		-0.0306	0.2005	0.0703
depth = 243 m				depth = 292 m		
0.842	-0.1007	-0.0431		0.8642	-0.0591	-0.0367
-0.1007	0.533	0.258		-0.0591	0.6174	0.1968
-0.0431	0.258	0.1392		-0.0367	0.1968	0.0673
depth = 250 m				depth = 299 m		
0.8418	-0.1132	0.0333		0.8493	-0.1118	0.0038
-0.1132	0.5476	0.2562		-0.1118	0.6313	0.2326
-0.0333	0.2562	0.1407		0.0036	0.2326	0.107

5.3.2 Density more dependent on the S-impedance

Table 5.3 shows the numerical values of the resolution matrix from the joint

inversion of the walkaway offset 3 data at a depth of 220-300 m, for the selected

damping factor $(\varepsilon = 3\%)$. The third row of the resolution matrix (Table 5.3) suggests that

for the study area, the relationship:

$$\frac{\Delta \rho}{\rho} \approx 0.25 \frac{\Delta J}{J}, \qquad (5.4)$$

may be used to remove the density term, thus improving the stability of the problem.

The SVD method for the three unknowns finds the "best" solution in the least-squares and minimum-length sense. However, if the solution is poor, it may be better to use only two unknowns (*I* and *J*). This suggests that the problem can be re-formulated so that only two parameters remain, rather than three parameters, with the given density from Equation (5.4). At this point, Equation (5.4) appears to be a good estimate for the density term using a normal least-squares inversion, and helps avoid the complex process of SVD damping in a 3-parameter AVO inversion of the Red Deer data.

Integrating the Equation (5.4) will provide a relationship between density and S-wave velocity as

$$\rho \cong A V_S^{1/3}, \qquad (5.5)$$

where A is constant; the derivation of Equation (5.5) is given in Appendix G. This relationship is similar to Gardner's rule but for the relationship between the density and the S-wave velocity. Equation (5.5) claims that it is reasonable to consider that S-wave velocity contributes to improving the density estimate more than the P-wave velocity for

the study area.

5.4 Red Deer Rock Property Estimates from AVO Inversion

Figure 5.17 shows the I, J and ρ estimates obtained from the 3-parameter PP inversion of the of zero-offset VSP data; there is a relatively accurate estimate of I, while good J and ρ estimates are not obtained. The zero-offset VSP data include incident rays very near to normal incident; therefore, a good estimate of the J or ρ cannot be expected from the zero-offset VSP data.
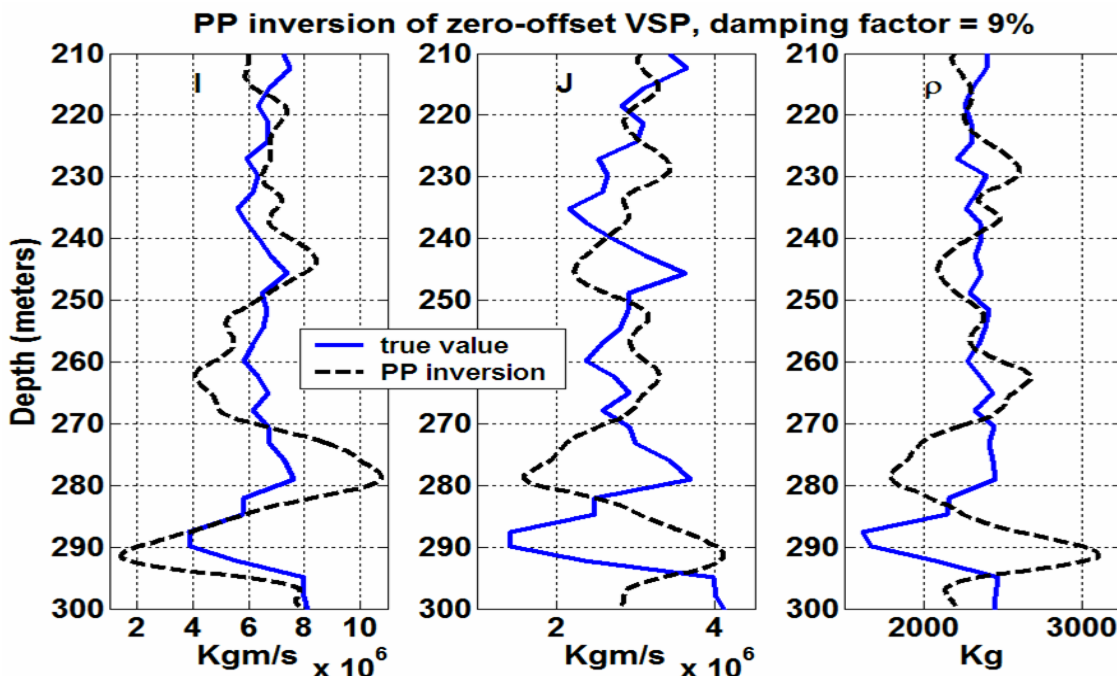
Figure 5.17: The P-impedance: I, S-impedance: J, and density: ρ, from the 3-parameter PP and joint inversion, and the PS inversion (for J and ρ) of zero-offset VSP data.

Figure 5.18-Figure 5.20 show the I, J and ρ estimates obtained from the 3-parameter

PP and joint inversion, and the PS inversion (for J and ρ) of the walkaway VSP data.

In each plot the blue curves are the real values calculated from the Red Deer velocity model, while the red, black and the green curves are estimates by the joint, PP and PS inversions respectively. For the walkaway offset data, the estimates are assigned to the half way point from source to the well. The AVO inversions have been stabilized using a damping factor of 3%.
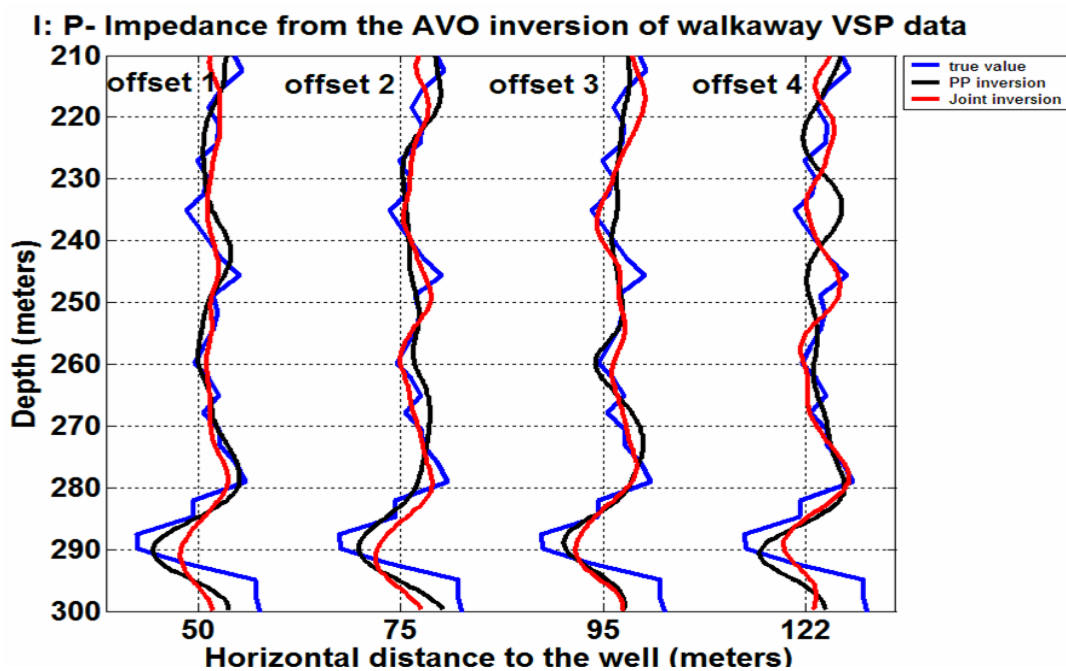
Figure 5.18: The I: P-impedance estimate from the 3-parameter PP and joint inversions of walkaway VSP data.

Figure 5.18 - Figure 5.20 support some of the previously stated results in Section 5.3 and Chapter 3 as follows:

- Joint inversion provides I estimates very similar to those of the PP inversion (Figure 5.18).

- The joint inversion produces the J and ρ estimates almost identical to those obtained from the PS inversion (Figure 5.19-Figure 5.20).

In Chapter 3, for the noisy synthetics data we showed that the joint inversion performs reasonably better than the PP and PS inversions, but only for the large amount of added random noise in Chapter 3 did joint inversions yield better estimates, otherwise, for noise free or less noisy data, it produces results very similar to the PP inversion (for the I estimate) and PS inversion (for the J and ρ estimate). Therefore, it seems safe to drop the complex process of joint inversion in terms of correlation of the PP and PS datasets, and apply the PP inversion to estimate the I, and PS inversion to estimate the J and ρ.
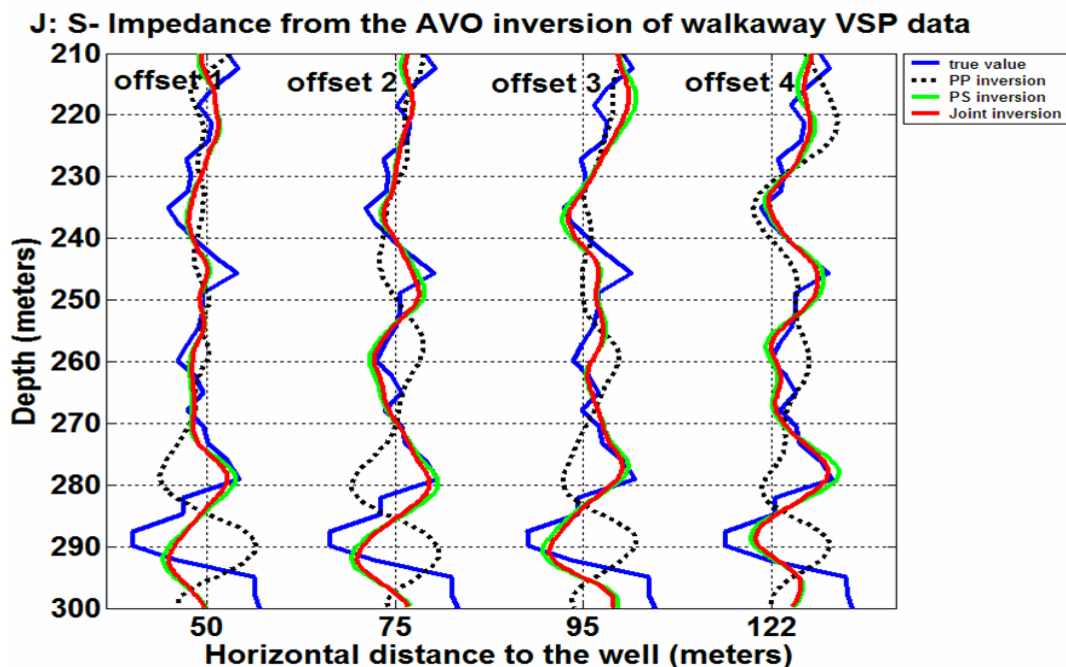
Figure 5.19: The J: S-impedance estimate from the 3-parameter PP and joint inversions, and the PS inversion (for J and ρ), of walkaway VSP data.
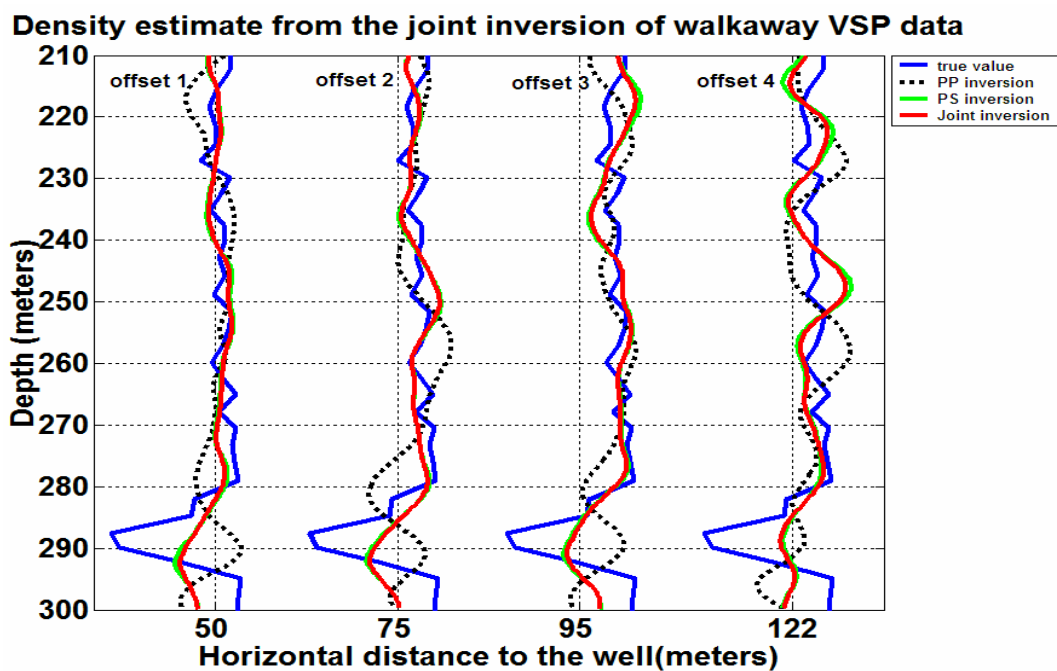
Figure 5.20: The ρ: density estimate from the 3-parameter PP and joint inversions and the PS inversion (for J and ρ), of walkaway VSP data.

5.4.1 Discrepancy in the Density Estimate

The density estimates from walkaway offsets 1-3 data are consistent with those predicted from the well logs (Figure 5.20); however, the density estimate from the walkaway offset 4 data does not resolve the Ardley coal zone. The undesired density estimate from the AVO inversion of the walkaway offset 4, with a smaller condition number, might be due to the following:

1. Incident angles in walkaway offset 4 survey possibly exceed the critical angle or become very large so that the assumptions of Aki-Richards equations are not valid.

2. Possible errors in the walkaway offset 4 data.

3. Possible lateral variation in coal properties which implies inappropriate assumptions such as having no-lateral velocity and horizontal layering.

The first two statements are unlikely to be the possible reason for the bad density estimates. Firstly, although the walkaway offset 4 survey has larger incident angles than other walkaway offset survey (for example incident angle of 25˚-36˚ PP case and 32˚-37˚ PS case at a depth of 290 m, see Table 5.1), the incident angles are still within an acceptable range; the PP and PS reflectivity calculated by exact Zoeppritz equations shown in Figure 5.21, support this statement. The low velocity Ardley coal layer has no critical angle.

.
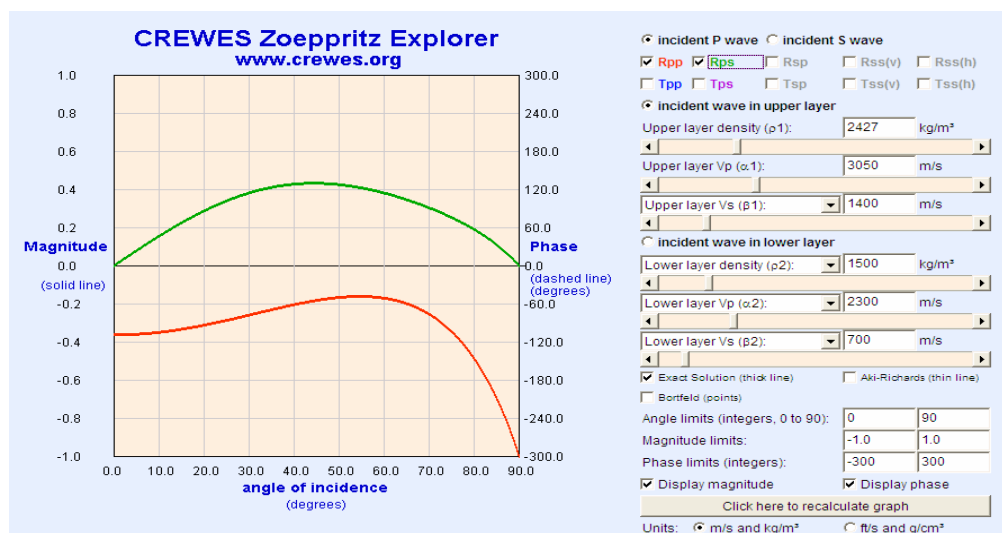
Figure 5.21: Calculated Zoeppritz PP and PS reflectivity for upper 8coal contact using parameters from the well logs (www.crewes.org). Low velocity coal layer has no critical angle.

Secondly, the offset 4 PP and PS datasets do not seem noisier than the other walkaway offset datasets (Figure 4.13 and Figure 4.14). Therefore, the undesired density

estimate from the AVO inversions of walkaway offset 4 data is probably due to the possible discontinuity in coal properties at the lateral distance between 95-125 m (half of the offset 3-to-half of the offset 4 source location) from the borehole.

5.5 Future VSP Surveys

To aid in designing future VSP surveys to provide the best possible chance for a successful AVO inversion, the SVD analysis was tested on a hypothetical source at 200 m from the well, very near to the walkaway offset 3 source location. This hypothetical source location is decided based on the earlier discussion of the probable discontinuity in the coal beds.
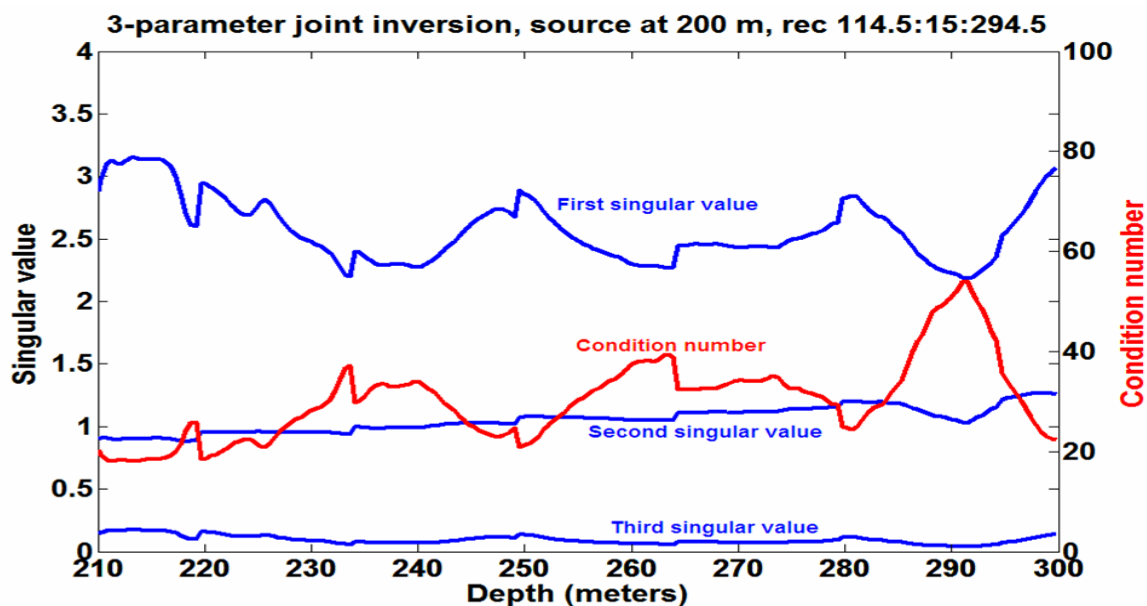
Figure 5.22: The singular value (in blue) and the condition number (red curve) versus depth from the 3-parameter joint inversion of the future survey with the source at 200 m from the well and the receiver location between 114.5 m to 294.5 m at 15 m intervals.

The condition number plots are illustrated for the inversion of data from this hypothetical source and the three sets of receiver locations as follows:

1. Receiver locations between 294.5 m and 114.5 m at 15 m intervals, identical to the Red Deer walkaway VSP (Figure 5.22).

2. Receiver locations between 294.5 m and 144.5 at 15 m intervals, to investigate on a possible decrease in the number of VSP tool movements (Figure 5.23).

3. Receiver locations between 294.5 m and 144.5 at 5 m intervals, to increase the fold compared to the case 2 above (Figure 5.23).
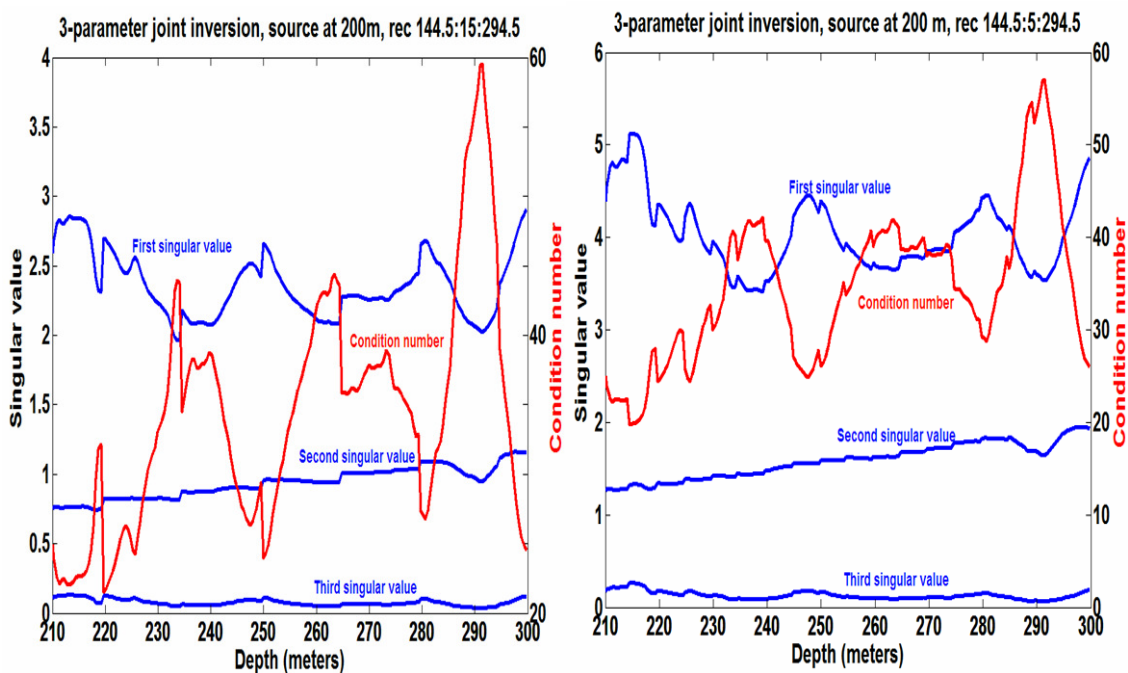
Figure 5.23: The singular value (in blue) and the condition number (red curve) versus depth from the 3-parameter joint inversion of the future survey with the source at 200 m from the well, (left plot) the receiver location between 144.5 m to 294.5 m with the receiver interval of 15 m, and (right plot) receiver location between 144.5 m to 294.5 m at 5 m intervals.

Comparing Figure 5.23 and Figure 5.22 shows that the cutting the number of near-surface receiver does not make a big change on the condition number values. Also comparing the left and right plots in Figure 5.23 shows that an increasing fold of data by decreasing the receiver interval would not affect the condition number plots intensely. Therefore, a future survey with the source at 200 m and the receiver locations between 144.5 m to 244.5 m at 15 m intervals is proposed.
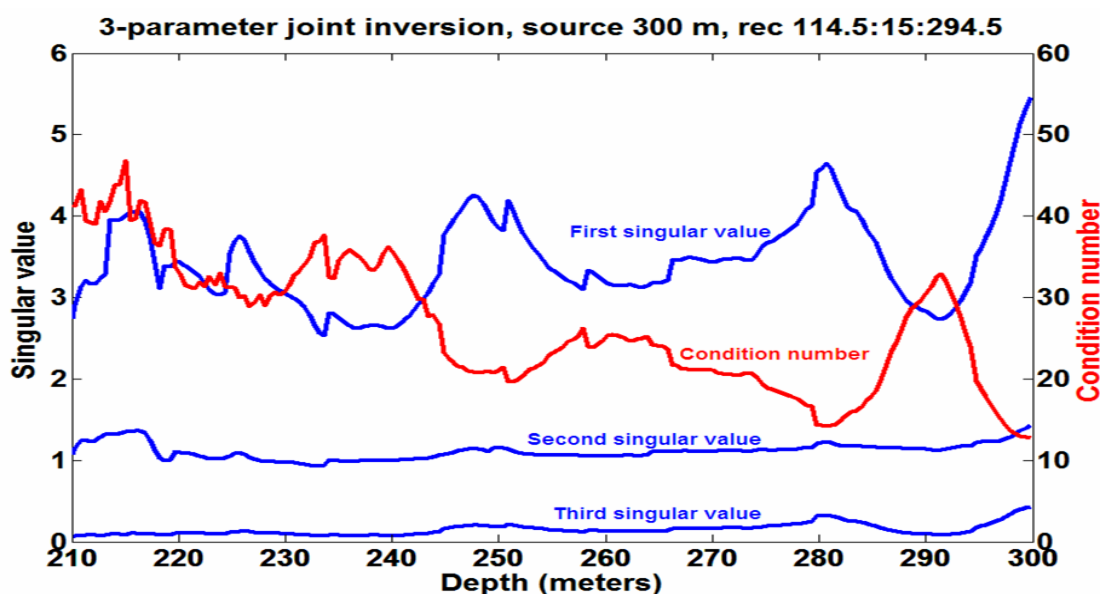
Figure 5.24: The singular value (in blue) and the condition number (red curve) versus depth from the 3-parameter joint inversion of the future survey with the source at 300 m from the well and the receiver location between 114.5 m to 294.5 m at 15 m interval.

It was thought that the above proposed VSP survey may provide useful inversion information with less expense. However, a future VSP survey with a larger source distance to the well would be interesting to acquire and might provide informations

regarding the possible discontinuity in the coal beds. For example, at the hypothetical source at 300 m, the condition number plot (Figure 5.24) has a lower condition number compared to the offset 4 (Figure 5.3). However, knowledge of the depositional setting and the lateral continuity of the coal beds are needed to predict the best survey parameters, because the velocities may begin to vary laterally as offset from the well increases; additionally, the energy source should be high enough to allow the imaging at the borehole.

5.6 Chapter Summary

The 3-parameter joint AVO inversion of surface seismic data has been developed to work with VSP data. This development includes some modifications to the surface seismic AVO inversion: (1) different raytracing; and (2) using the first break times of VSP data in the time-to-depth conversion step. The VSP AVO inversion is applied to Red Deer VSP data. The 3-parameter PP, joint inversion and the PS inversion (for the J and ρ) are ill-posed problems especially for the Ardley coal zone. Therefore, the SVD damping method is utilized.

The damping factor contributes to the stability of the inversion by suppressing the effect of small singular values. By increasing the damping factor, the errors between the estimates and the true values from the well logs is decreased while the resolution matrix is moving away from the ideal case. Comparing the maximum correlation between the estimates of different damping factor and the values, the damping factor equal to 3% is selected for the AVO inversion of the Red Deer data. The examination on the resolution

matrix demonstrates that the S-wave velocity contributes to improving the density estimate more than the P-wave velocity for the study area. The examination of the estimates from the PP, PS and the joint inversion of the Red Deer walkaway VSP data leads to the following conclusions:

- The joint inversion provides the I estimate very similar to those of the PP inversion.

- The joint inversion produces the J and ρ estimates very similar to those obtained from the PS inversion.

- It seems safe to drop the complex process of joint inversion, in terms of correlation of the PP and PS datasets, and apply the PP inversion to estimate the I, and PS inversion to estimate the J and ρ.

- The undesired density estimate from the AVO inversions of walkaway offset 4 data is probably due to the possible discontinuity in coal properties at the lateral distance between 95-125 m.

To aid in designing a future VSP survey to provide the best possible chance for successful AVO inversion, a VSP survey with the source at 200 m (near to the source of offset 3 data) and the receiver locations between 144.5 m to 244.5 m at 15 m intervals is proposed. Also, to examine the possible discontinuity in the coal beds, a VSP survey with source at 300 m and the receiver locations between 144.5 m to 244.5 m at 15 m intervals is proposed.

# CHAPTER 6: Conclusions and Future Work

6.1 Summery and Conclusions

The linear joint AVO inversion described by Larsen and Margrave (1999) has been cast as a MATLAB algorithm called 2-parameter joint inversion. This algorithm includes some modifications to Larsen and Margrave's approach: (1) deriving impedance estimates from P- and S-impedance reflectivity traces; and (2) restoring the low-frequency components to the impedance estimates.

The 2-parameter joint inversion has been extended to the 3-parameter joint inversion to estimate the compressional impedance, shear impedance, and density. Additionally, the 3-parameter joint AVO inversion of surface seismic data has been developed to work with VSP data.

The testing of the AVO inversion on several synthetic example leads to the following observations:

- In the 2-parameter joint inversion, the PP data dominates in the I estimate, while the PS data dominates in the J estimate. This effect is used as an indicator for choosing the right polarity of the PP and PS data.

- The 2-parameter PP and PS inversions are each able to estimate one parameter

successfully, while the 2-parameter joint inversion is capable of providing the good estimates for both the *I* and *J.*

- Restoring the low frequencies has a significant effect on the AVO inversion estimates.

- In an AVO inversion, adding the fold of data, by incorporating more far offsets data, will lead to better model parameter estimates. The further offset incident angles should be pre-critical and adding the post-critical far offsets data will ruin the model parameter estimates.

- The 3-parameter joint inversion (with higher condition number values) is a less stable problem compared to the 2-parameter joint inversion,

- The linear joint inversion is less sensitive to the background velocity errors; therefore, the angle errors (from raytracing) will not strongly bias the joint inversion results, as shown under the assumption of horizontal layering geology.

- In presence of random noise in the data, the joint inversion is more accurate for all parameters than PP or PS inversions. The joint inversion has very good estimates for both *I* and *J* and reasonable estimate for the ρ even in the presence of noise.

In the case study, the VSP AVO inversion is applied to Red Deer VSP data. The 3-parameter PP, joint inversion and the PS inversion (for the *J* and ρ) are ill-posed problems especially for the Ardley coal zone and the SVD damping method is utilized to stabilized the problem. The damping factor contributes to the stability of the inversion by suppressing the effect of small singular values. By increasing the damping factor, the

errors between the estimates and the true values from the well logs is decreased while the resolution matrix is moving away from the ideal case. Comparing the maximum correlation between the estimates of different damping factor and the values, the damping factor equal to 3% is selected for the AVO inversion of the Red Deer data. The examination of the resolution matrix demonstrates that the S-wave velocity contributes to improving the density estimate more than the P-wave velocity for the study area.

The examination of the estimates from the PP, PS and the joint inversion of the Red Deer walkaway VSP data (Chapter 5) and synthetic data (Chapter 3), leads to the following conclusions:

- Inverting the compressional data provides an I estimate very similar to those of the joint inversion.

- Inverting the converted shear data provides the J and ρ estimate very similar to those of the joint inversion.

- It seems safe to drop the complex process of joint inversion, in terms of correlation of the PP and PS datasets, and apply the PP inversion to estimate the I, and PS inversion to estimate the J and ρ.

To aid in designing a future VSP survey to provide the best possible chance for a successful AVO inversion, a VSP survey with the source at 200 m (near to the source of offset 3 data) and the receiver locations between 144.5 m to 244.5 m at 15 m intervals is proposed. Also, to examine the possible discontinuity in the coal beds, a VSP survey with

source at 300 m and the receiver locations between 144.5 m to 244.5 m at 15 m intervals is proposed.

For the Red Deer case study, rather than the usual relation between the density and compressional velocity, a relation between density and shear velocity has been observed, which makes the joint inversion more stable. This relation might apply in other cases also; however, more study is required.

6.2 Future Work

The joint inversion provides similar compressional impedance, compared to the PP inversion, as in this thesis. However, a better or comparable P-impedance by the joint inversion is documented by Larson and Margrave (1999) for the Blackfoot data and Zhang and Margrave (2003) for the Pikes Peaks oil field data. The effect of random noise on the AVO inversion accuracy is examined; the joint inversion provides comparable P-impedance compared to the PP inversion. However, the noise in real data is more than random noise. There are some coherent noises in the real datasets which will not be suppressed by doubling the data and may become worst. Therefore, it is recommended that behaviour of the PP, PS and joint inversion to be examined in the presence of noise, such as generating random noise in frequency domain (instead of time domain) or some linear coherent noise in the time domain.

The condition number of the matrix of Aki-Richards coefficients is a function of the background velocity and the geometry of the problem, and not the data itself. I observed

that adding the random noise did not have noticeable change on the condition number plot, as was predictable due to the fact that the AVO inversion is not sensitive to the background. However, other kind of noise would definitely affect the condition number plot; it should be verified how noise will effect the condition number analysis. This should help demonstrate the advantage of the joint inversion over the PP or PS inversions.

PP and PS event correlation should be done in PP time. Consequently, the application of joint inversion in time should be examined. The joint inversion in time might be more accurate due to the drop of the time or depth migration process.

The reliability of the linear joint inversion showed that the linear approximation to the reflection coefficients is causing the errors in the estimates. Therefore, a non-linear inversion using the exact Zoeppritz should help provide better estimates.

The Red Deer case study AVO inversion, suggested a relationship between the density and shear wave velocity. It is recommended that to the 3-parameter Joint inversion be re-formulated as 2-parameter joint inversion using this relationship, to see if it helps in stabilizing the inversion.

Appendix A

General Least-Squares Solution

This proof has been adapted from Dr. Krebes (2004) course notes. The Least-squares method involves minimizing the sum of squared errors, i.e. minimizing

$$E = \sum_{i=1}^{n} \left(d_i - d_i' \right)^2 \tag{A.1}$$

where d_i' is the model predicted data and d_i is measured data. Then E, the total error produced by linearizing the Zoeppritz equations, becomes

$$E = \sum_{i=1}^{n} \left(d_i - \sum_{j=1}^{m} G_{ij} m_j \right)^2. \tag{A.2}$$

To find the minimum of E,

$$0 = \frac{\partial E}{\partial m_k} = \sum_{i=1}^{n} 2 \left(d_i - \sum_{j=1}^{m} G_{ij} m_j \right) \left(-G_{ik} \right), \tag{A.3}$$

and equivalently

$$\sum_{i=1}^{n} G_{ik} \sum_{j=1}^{m} G_{ij} m_j = \sum_{i=1}^{k} G_{ik} d_i, \tag{A.4}$$

$$\sum_{j=1}^{m} \sum_{i=1}^{n} G_{ki}^{T} G_{ij} m_j = \sum_{i=1}^{k} G_{ik} d_i, \tag{A.5}$$

or in matrix form

$$m = \left(G^{T} G \right)^{-1} G^{T} d. \tag{A.6}$$

The solution *m* is then obtained from

$$m = \left(G^T G\right)^{-1} G^T d. \tag{A.7}$$

Appendix B

Weights in the weighted stacking scheme

The weighted stacking scheme weights are adapted from Larsen and Margrave (1999).

$$W_{IPP} = \frac{\left(A_i \sum_{i=1}^{n}(B_i^2 + D_i^2) - B_i \sum_{i=1}^{n}(A_i B_i + C_i D_i) \right)}{\sum_{i=1}^{n}(A_i^2 + C_i^2)\sum_{i=1}^{n}(B_i^2 + D_i^2) - \left[\sum_{i=1}^{n}(A_i B_i + C_i D_i) \right]^2} \tag{B.1}$$

$$W_{IPS} = \frac{\left(C_i \sum_{i=1}^{n}(B_i^2 + D_i^2) - D_i \sum_{i=1}^{n}(A_i B_i + C_i D_i) \right)}{\sum_{i=1}^{n}(A_i^2 + C_i^2)\sum_{i=1}^{n}(B_i^2 + D_i^2) - \left[\sum_{i=1}^{n}(A_i B_i + C_i D_i) \right]^2} \tag{B.2}$$

$$W_{JPP} = \frac{\left(B_i \sum_{i=1}^{n}(A_i^2 + C_i^2) - A_i \sum_{i=1}^{n}(A_i B_i + C_i D_i) \right)}{\sum_{i=1}^{n}(A_i^2 + C_i^2)\sum_{i=1}^{n}(B_i^2 + D_i^2) - \left[\sum_{i=1}^{n}(A_i B_i + C_i D_i) \right]^2} \tag{B.3}$$

$$W_{JPS} = \frac{\left(D_i \sum_{i=1}^{n}(A_i^2 + C_i^2) - C_i \sum_{i=1}^{n}(A_i B_i + C_i D_i) \right)}{\sum_{i=1}^{n}(A_i^2 + C_i^2)\sum_{i=1}^{n}(B_i^2 + D_i^2) - \left[\sum_{i=1}^{n}(A_i B_i + C_i D_i) \right]^2} \tag{B.4}$$

Appendix C

Derivation of Integration of the Reflectivity Trace to the Impedance Trace

This proof is adapted from Ferguson and Margrave (1996). The estimated reflectivity traces *ΔI/I*, *ΔJ/J* and *Δρ/ρ* from joint inversion are integrated to estimate *I* and *J* and *ρ* in *BLIPM* routine.

Define the jth sample of the reflectivity trace, r_j, as the relative change in α across the jth interface (Aki-Richards, 1980), thus,

$$r_j = \frac{1}{2}\left(\frac{\Delta\alpha}{\alpha}\right)_j = \frac{\alpha_{j+1} - \alpha_j}{\alpha_{j+1} + \alpha_j},$$
(C.1)

where α can be either *I, J* or *ρ*. From calculus we have

$$r_j \approx \frac{1}{2}\Delta\ln(\alpha_j) = \frac{1}{2}\left(\ln(\alpha_{j+1}) - \ln(\alpha_j)\right) = \frac{1}{2}\ln\left(\frac{\alpha_{j+1}}{\alpha_j}\right).$$
(C.2)

Summing both sides and reducing gives

$$2\sum_{k=1}^{j} r_k = \sum_{k=1}^{j}\ln\left(\frac{\alpha_{k+1}}{\alpha_k}\right) = \ln\left(\frac{\alpha_{j+1}}{\alpha_j}\frac{\alpha_j}{\alpha_{j-1}}\cdots\frac{\alpha_2}{\alpha_1}\right).$$
(C.1)

Thus

$$2\sum_{k=1}^{j} r_k = \ln\left(\frac{\alpha_{j+1}}{\alpha_1}\right).$$
(C.2)

Solving Equation (C.2) for $ln(\alpha_{j+1})$, we will have

$$ln(\alpha_{j+1}) = ln(\alpha_1) + 2\sum_{k=1}^{j} r_k.$$
(C.3)

Exponentiation of Equation (C.3) gives

$$\alpha_{j+1} = \alpha_1 \, exp\left(2\sum_{k=1}^{j} r_k\right), \tag{C.4}$$

which gives the value of α at j+1 sample depth.

Appendix D

Time-to-Depth Conversion of PP and PS Surface Seismic Data

A simple MATLAB routine for converting PP or PS datasets to depth is presented.

```
function [seisz,z,dz,z1,z2]=seis2z(seis,t,vp,zv,vs,iv,zmin,zmax),
%SEIS2Z: converts PP or PS surface seismic data from time to depth.
%
% seis: PP or PD data in time.
% t:  time axis of PP or PS data.
% vp: P-wave velocity log.
% zv: depth axis for velocity log.
% vs: S-wave velocity log.
% iv: inversion type, iv=1 for PP data  and iv=2 for PS data
% zmin: minimum desired depth.
% zmax: maximum desired depth.
%%%%%%%%%%%%%%%%%%%%%%%%%%%%%%%%%%%%
%seisz: the output PP or PS data.
%z:      the output depth-axis.
%%%%%%%%%%%%%%%%%%%%%%%%%%%%%%%%%%%%

if  iv==1;               % for PP data
   vs=vp;
end;

v=vs;                        %to get the same sample for both PP and PS data.
dt=t(2)-t(1);               % time interval
[nt,nx]=size(seis);          %nt is the number of time steps.

pson=(10^6./vp);           %P-sonic
sson=(10^6./vs);           %S-sonic
spson=(pson + sson)/2;     %Fake PS-sonic

% sonic2tz: computes an approximate 2-way time-depth curve from a sonic log for
             use with depth conversion.
% tstart=0   %tstart: the starting time corresponded to the z(1) in the log.
[tz,zt]=sonic2tz(spson,zv,-601,tstart);          %to get time-depth curve.
                                      %601: nleg.
%To determine depth range
%zb=interp1(tz,zt,t);
% zb1=min(zb);
% zb2=max(zb);
% zmin=min(zb1,zmin);
```

```
% zmax=max(zb2,zmax);
dz=min(v)*dt/2;                          % sample depth
nz=floor((zmax-zmin)/dz)+1;              % number of depth sample
z=(0:nz-1)*dz + z1;                       %z: depth axis
z=z(:);                                   %to have column vector for depth
t2=interp1(zt,tz,z);
nt2=length(t2)
seisz=zeros(nt2,nx);              %data in depth, nx=number of offsets

for k=1:nx,
   seisz( : ,k)=sinci(seis(: ,k),t',t2);    %to interpolate the amplitude at each depths sample
end;
```

Appendix E

Smoothing Velocity Model

A simple MATLAB routine for smoothing blocky velocity models is presented.

```
function smoothv=smooting(v,zv,n),
% SMOOTHING : makes a smooth log out of the blocky velocity log.
% the smoothed P- velocity is used as the background velocity in the inversion
%v: P-wave velocity vector.
%zv: the depth-axis of velocity vector.
%n: Degree of polynomial that fits the data
%smoothv: the smoothed velocity vector.
%%%%%%%%%%%%%%%%%%%%%%%%%%%%%%%%%%%%%%%%

%polyfit function finds the coefficients of a polynomial P(zvp) of
%degree n that fits the data, P(zvp(k))~=vp(k), in a least-squares.
if n==0,
    smoothv=v;
else
    pop=polyfit(zv,v,n);
    smoothv=polyval(pop,zv);
end;
```

A simple MATLAB routine for smoothing well logs is presented.

```
function smoothv=smootlog(v,n),
% SMOOTHLOG : makes a smooth log out of  a well log
% v: velocity vector.
% n: size of the boxcar which is convolving with log to smooth that
%----------------------------------------
% smoothv: the smoothed velocity vector, having the same sample as input velocity
%%%%%%%%%%%%%%%%%%%%%%%%%%%%%%%%%%%%%%%%%%
if n==0,
    smoothv=v;
else
    bxcar=ones(1,n);
    smoothv=convz(v,1/n*bxcar);
end;
```

Appendix F

A numerical test of the relation $R_{PS} \approx -R_{PP} - R_{SS}$

The Aki-Richards approximations for R_{PP}, R_{PS} and R_{SS} are

$$R_{PP}(\theta) \approx \frac{1}{2\cos^2\theta} \frac{\Delta\alpha}{\alpha} - 4\beta^2 p_P^2 \frac{\Delta\beta}{\beta} + \frac{1}{2}\left[1 - 4\beta^2 p_P^2\right]\frac{\Delta\rho}{\rho}. \tag{F.1}$$

$$R_{PS}(\theta,\phi) \approx -\frac{p\alpha}{2\cos\varphi}\left[\left(1 - 2\beta^2 p_P^2 + 2\beta^2 \frac{\cos\theta}{\alpha}\frac{\cos\varphi}{\beta}\right)\frac{\Delta\rho}{\rho} - \right.$$
$$\left. 4\beta^2\left(p_P^2 - \frac{\cos\theta}{\alpha}\frac{\cos\varphi}{\beta}\right)\frac{\Delta\beta}{\beta}\right]. \tag{F.2}$$

$$R_{SS}(\theta) \approx -\frac{1}{2}(1 - 4\beta^2 p_S^2)\frac{\Delta\rho}{\rho} - \left(\frac{1}{2\cos^2\theta} - 4\beta^2 p_S^2\right)\frac{\Delta\beta}{\beta}. \tag{F.3}$$

where α is P-wave velocity, β is S-wave velocity, p_P is the PP ray parameter, and θ is the

P or S incident angle and φ is the PS reflected angle. For the P incidence angle θ, the PP

and PS have the same ray parameter, $p_P = \dfrac{\sin\theta}{\alpha} = \dfrac{\sin\varphi}{\beta}$, and $p_S = \dfrac{\sin\theta}{\beta}$.

Assuming that the ratio of α/β is constant, then $\dfrac{\Delta\alpha}{\alpha} \cong \dfrac{\Delta\beta}{\beta}$. Then we can write

$$R_{PP} + R_{PS} = A_1\frac{\Delta\rho}{\rho} + B_1\frac{\Delta\beta}{\beta}, \tag{F.4}$$

$$R_{SS} = A_2\frac{\Delta\rho}{\rho} + B_2\frac{\Delta\beta}{\beta}, \tag{F.5}$$

where,

$$A_1 = \frac{1}{2}\left[1 - 4\beta^2 p_P^2\right] - \frac{p_P\alpha}{2\cos\varphi}\left(1 - 2\beta^2 p_P^2 + 2\beta^2 \frac{\cos\theta}{\alpha}\frac{\cos\varphi}{\beta}\right), \tag{F.6}$$

$$B_1 = \frac{1}{2\cos^2\theta} - 4\beta^2 p_P{}^2 + \frac{2p_P\alpha\beta^2}{\cos\varphi}\left(p_P{}^2 - \frac{\cos\theta}{\alpha}\frac{\cos\varphi}{\beta}\right). \tag{F.7}$$

We try to show that: $A_1 \approx -A_2$ and $B_1 \approx -B_2$ numerically. As an example for $\alpha_1 = 4000$, $\alpha_2 = 5000$, $\beta_1 = 2000$ and $\beta_2 = 2500$ for pre-critical angles, the plots of A_1 and A_2 are very close, also the plots B_1 and B_2 are very close (Figure F. 1); similarly for the different incident angle θ, the two relation $R_{PP} + R_{PS}$ and $-R_{SS}$ is comparable for sub-critical angles (Figure F. 2).
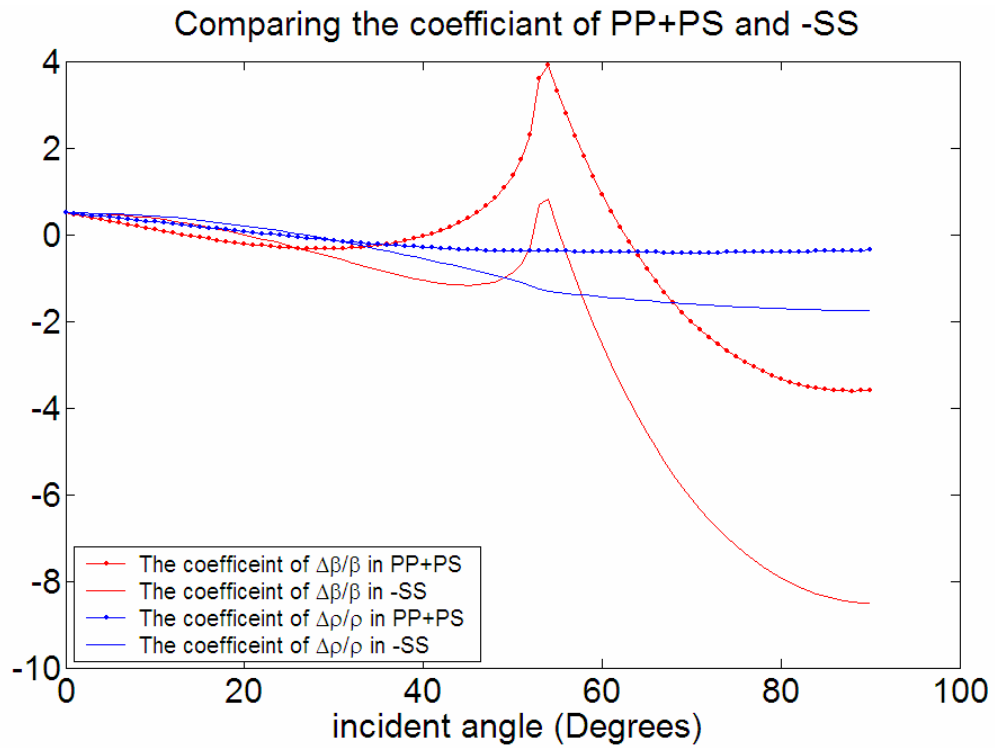

Figure F. 1: The plots of coefficients of $\dfrac{\Delta\beta}{\beta}$ and $\dfrac{\Delta\rho}{\rho}$ from $-R_{SS}$ and $R_{PP} + R_{PS}$.
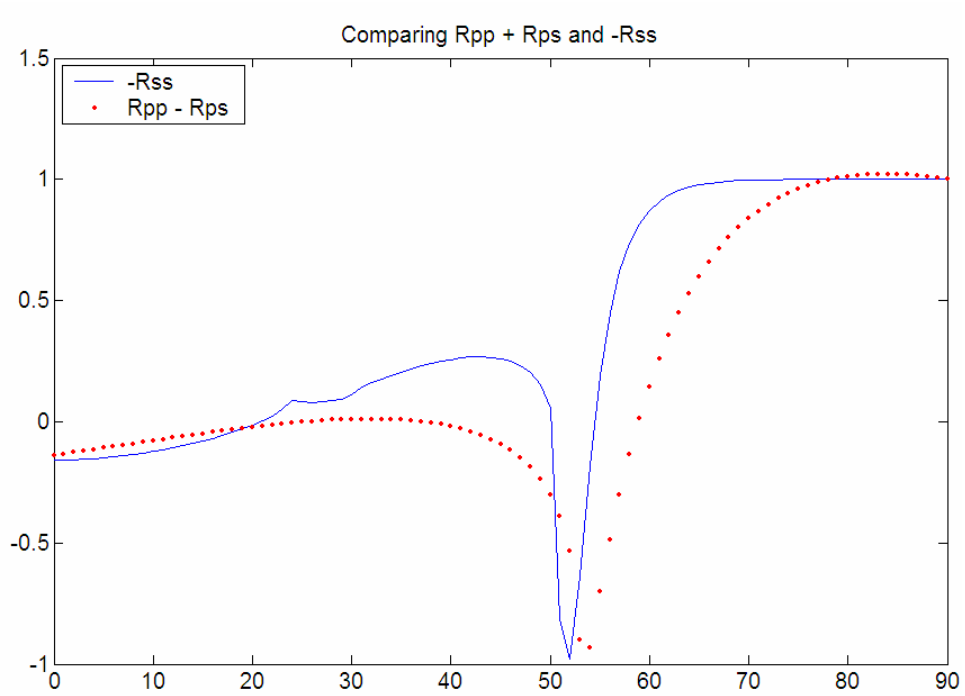
Figure F. 2: Comparing the $-R_{SS}$ and $R_{PP} + R_{PS}$ relations for different incident angle. The horizontal axis is P or S incident angle.

Appendix G

Derivation of relation between density and S-wave velocity

The derivation of the relation between the density ρ, and the S-wave velocity V_S from Equation (5.4) is presented. Substitution of the relation $\Delta J / J \cong \Delta\rho / \rho + \Delta V_S / V_S$, into Equation (5.4) gives

$$\frac{\Delta\rho}{\rho} \cong \frac{1}{4}\left(\frac{\Delta\rho}{\rho} + \frac{\Delta V_S}{V_S}\right). \tag{G.1}$$

Then

$$\frac{\Delta\rho}{\rho} \cong \frac{1}{3}\frac{\Delta V_S}{V_S}. \tag{G.2}$$

Supposing that the relative change Δ well approximated by a derivative, will result in

$$\frac{d\rho}{\rho} \cong \frac{1}{3}\frac{dV_S}{V_S}. \tag{G.3}$$

Taking a couple of simple algebra steps, will result

$$\frac{d\rho}{\rho} \cong \frac{1}{3}\frac{dV_S}{V_S} \times \frac{V_S^{-2/3}}{V_S^{-2/3}}, \tag{G.4}$$

$$\frac{d\rho}{\rho} \cong \frac{d(V_S^{1/3})}{V_S^{1/3}}, \tag{G.5}$$

$$d(\ln\rho) = d\left(\ln(V_S^{1/3})\right), \tag{G.6}$$

$$(\ln\rho) \cong (\ln(V_S^{1/3})) + C, \tag{G.7}$$

where C is constant. Exponentiation of Equation (G.7) gives

$$\rho \cong A V_S^{1/3}, \tag{G.8}$$

where A is constant.

References

Aki, K., and Richards, P. G., 1980, Quantitative Seismology : Theory and Methods, W. H. Freeman and Company. Vol. 1.

Beaton, A., 2003. Production potential of coalbed methane resources in Alberta: Energy & Utilities Board/Alberta Geological Survay, Earth Scinces Report, 2003-03, 68 pp.

Bleistein, N., Cohen, J. K., 1982, The velocity inversion problem ― Present status, new directions, Geophysics, **47**,1497-1511.

Brown, J. R., Stewart, R. R., and Lawton, D. C., 2002, Tutorial ; A proposed polarity standard for multicomponent sesimic data, Geophysics, **67**, 1028-1037.

Castagna, J. P., Batlz, M. L., and Eastwood, R. L. 1985, Relationship between compressinal and shear-wave velocities in elastic silicate rocks :Geophysics, **50**, 551-570.

Castagna, J. P., Batlz, M. L., and Kan, T. K., 1993, Rock physics ― the link between rock properties and AVO response, *in* Castagna, J.P., and Backus. M.M., Eds., offset-dependent reflectivity – Theory and practice of AVO analysis: Soc. Expl. Geophys. 135-171.

Coueslan, M., 2005, Big-P ZVSP Processing and Wavefiled Seperation Results for Cygnet 9-34, Unpublished Course Project.

De Nicolao, A., Drufuca, G., and Rocca, F., 1993, Eigenvalues and eigenvectors on lineaized elastic inversion, Geophysics, **58**, 670-679.

Dębski, W., Tarantola A., 1995, Information on elastic parameters obtained from the amplitudes of reflected waves: Geophysics, **60**, 1426-1436.

Dewangan, P., Grechka, V., 2003, Inversion of multuicomponent, multiazimuth, walkaway VSP data for the stiffness tensor, Geophysics, **68**, 1022-1031.

Downton, J. E., Lines, L., 2001, Constrained three parameter AVO inversion and uncertainty analysis : 71st Ann. Internat. Mtg., Soc. Expl. Geophys., expanded Abstracs, 251-254.

Downton, J.E., 2005, Seismic parameter estimation from AVO inversion, PHD Thesis, University of Calgary.

Engelmark, F., 2000, Using converted shear waves to image reservoirs with low-impedance contrast : The Leading Edge, **19**, 600-603.

Ensley, R. A., 1984, Comparison of P-wave and S-wave seismic data ─ A new method for detecting gas reservoir : Geophysics, **49**, 1420-1431.

Fatti, J. L., Vail, P. J., Smith, G.C., Strauss, P.J., and Levitt, P.R., 1994, Detection of gas in sandstone reservoirs using AVO analysis : A 3-D seismic case study history using the Geostack technique : Geophysics, **59**, 1362-1376.

Ferguson, R. J., Margrave G.F., 1996, A simple algorithm for band-pass impedance inversion, CREWES Research Report, 8, 1-10.

Gardener, G. H. F., Gardener, L.W., and Gregory, A.R., 1974, Formation velocity and density : the diagnostic basis for stratigraphic traps : Geophysics, **39**, 770-780.

Gochioco, L. M., 1991. Tuning effect and interference reflections from thin beds and coal seams: Geophysics, **56**, 1288-1295.

Gochioco, L. M., 1992. Modelling studies of interference reflections in thin-layered

media bounded by coal seams: Geophysics, **57**, 1209-1216.

Hardage, B. A., 1985, Verical Seimic Profiling, Handbook of Geophysical Exploration, Geophysical Press, London-Amesterdam.

Henley, D. C., 2003, Coherent noise attenuation in the radial trace domain, Geophysics, **68**, 1408-1416.

Jackson, D. D., 1972, Interpretation of Inaccurate, Insufficient and Inconsistent Data: Geophys. J. R. astr. Soc. , 28, 97-109.

Jin, S., Beydoun, W., and Madariaga, R., 1993, A stable elastic inversion for marine data: 63rd Ann. Internat. Mtg., Soc. Expl. Geophys., Expanded Abstracts, 665-668.

Jin, S., Cambois, G., and Vuillermoz, C., 2002, Shear-wave velocity and density estimation from PS-wave AVO analysis: Application to an OBS database from the North Sea: Geophysics, **65**, 1446-1454.

Jonnane, M., Beydoun, W., Crase, E., Cao Di, Koren, Z., Landa, E., Mendes, M., Pica, A., Nobel, M., Roth,m G., Singh, S., Snieder, R., Trantola, A., Trezeguet, D., and Xie, M., 1988, Wavelengths of earth structures that can be resolved from seismic reflected data: Geophysics, **54**, 904-910.

Krebes, E. S., 2004, Theoretical seismology, unpublished course notes.

Larsen J. A., 1999, AVO inversion by simultaneous PP and PS inversion: M.Sc. Thesis, University of Calgary.

Larsen, J. A., Margrave G. F., Lu H., and Potter C. C., 1998, Simultaneous P-P and P-S inversion by weighted stacking applied to the Blackfoot 3C-3D survey, CREWES Research Report, 10, 50-1‒50-22.

Lay. D. C., 1996, Linear algebra and its applications, 2nd ed, Addison-Wesley.

Lawton, D. C., and Howell, T. C., 1992, P-P and P-SV synthetic stacks, , 62nd SEG Ann. Interat. Mtg., Soc. Expl. Geophys., Expanded Abstracts, 1344-1347.

Lindseth, Roy O., 1979, Synthetic sonic logs ─ Aprocess for statigraphic interpretation : Geophysics, **44**, no.1, 3-26.

Gildow, P. M., Smith, G. C., and Vail, P. J., 1992, Hydrocarbon detection using fluid factor traces, a case study : How useful is AVO analysis ? Joint SEG/EAEG summer research workshop, Technical Program and Abstracts, 78-89.

Margrave, G. F., and Foltinek D. F., 1995, Synthetic P-P and P-SV cross sections : CREWES Project Annual Research Report, Vol. 7, Ch. 5.

Margrave, G. F., Stewart, R. R. And Larsen, J. A., 2001, Joint PP and PS seismic inversion, The Leading Edge, 1048-1052.

Menke, W., 1989, Geophysical Data Analysis : Discrete inversion Theory : International geophyical series, 45, Academic press.

Richardson, S. E., 2003, Multicomponent seismic application in coalbed methane development, Red Deer, Alberta, M.Sc. Thesis, University of Calgary.

Sheriff, R. E. 1991, Encyclopedic dictionary of applied geophysics, Third edition, Society of Exploration Geophysicists, Geophysical References **1**.

Shuey, R., 1985, A simplification of Zoeppritz equations : Geophusics, **50**, 609-614.

Smith, G. C. and Gidlow, P. M., 1987, Weighted stacking for rock property estimation

and detection of gas: Geophysical Prospecting, 35, 993-1014.

Stewart, R. R., 1990, Joint P and P-SV inversion: CREWES Research Report, 2, 112-115.

Stewart, R. R., Zhang Q., and Guthoff, F., 1995, Relationships among elastic-wave values: Rpp, Rps, Rss, Vp, Vs, κ, σ and ρ: The CREWES Project Research Report, Vol. 7.

Stewart, R. R., Gaiser, J. E., Brown, R. J., and Lawton, D. C., 2002, Tutorial, Converted-wave seismic exploration : Methods : Geophysics, **67**, 1348-1363.

Tarantola, A., 1986, A strategy for nonlinear elastic inversion of seismic reflection data: Geophysics, **51**, 1893-1903.

Tatham, R. H., and McCormick, M. D., 1991, Multi-component seismology in petroleum exploration: Society of Exploration Geophysicists.

Thigpen, B. B., Dalby, A. E., and Landrum R., 1975, Special report of the subcommittee on polarity Standard: Geophysics, **40**, 694-699.

Thomson, L., 1990, Poisson was not a geophysicist: The Leading Edge, December 1990, 27-29.

Treitel, S., and Lines, L. R., 1982, Linear inverse theory and deconvolution, Geophysics **47**, 1153-1159.

Ursin B., Ekren, B. O., and Tjaland, E., 1996, the information content of the elastic reflection Matrix: Geophys, J. Internat., **125**, 214-228.

Vestrum, R. W., and Stewart, R. R., 1993, Joint P and P-SV inversion: application and

testing: CREWES Research Report, 5, 13-1—13-7.

Waters, K. H., 1987, Reflection seismology: John Wiley and sons.

Wright, J., 1984, The effects of anisotropy on reflectivity-offset: 5th Annual Internat. Mtg., Soc. Expl. Geophys., Expanded Abstracts, 84.

Yilmaz, O., 1987, Seismic data processing: Soc. Expl. Geophys.

Zhang, H., Margrave, G. F., 2003, Joint PP-PS inversion at Pikes Peak oilfield, Saskatchewan, CREWES Research Report, 15, 1-12.